A Precise Measurement of the Left-Right Cross Section Asymmetry in Z Boson Production

by

Amitabh Lath

B.Sc., Massachusets Institute of Technology (1988)

Submitted to the Department of Physics
in partial fulfillment of the requirements for the degree of

Doctor of Philosophy

at the

MASSACHUSETTS INSTITUTE OF TECHNOLOGY

November 1994

Author...
Department of Physics
November 10, 1994

Certified by ....
Henry W. Kendall
Professor of Physics
Thesis Supervisor

Accepted by...
George F. Koster
Chairman, Departmental Committee on Theses

Science

A Precise Measurement of the Left-Right Cross Section Asymmetry in Z Boson Production

by

Amitabh Lath

Submitted to the Department of Physics
on November 10, 1994, in partial fulfillment of the
requirements for the degree of
Doctor of Philosophy

Abstract

This thesis presents a measurement of the left-right asymmetry, A_{LR}, in the production cross section of Z Bosons produced by e^+e^- annihilations, using polarized electrons, at a center of mass energy of 91.26 Gev. The data presented was recorded by the SLD detector at the SLAC Linear Collider during the 1993 run. The mean luminosity-weighted polarization of the electron beam was $\mathcal{P}_e^{lum} = (63.0 \pm 1.1)\%$. Using a sample of 49,392 Z events, we measure A_{LR} to be 0.1626±0.0071(stat.)±0.0030(sys.), which determines the effective weak mixing angle to be $\sin^2 \theta_W^{\text{eff}}$ =0.2292±0.0009(stat.)±0.0004(sys.). This result differs from that expected by the Standard Model of Particles and Fields by 2.5 standard deviations.

Thesis Supervisor: Henry W. Kendall
Title: Professor of Physics

Acknowledgments

Some traditions are strange. Tradition dictates I spend nearly two hundred pages expounding on results everyone already knows, and about two pages naming people important to me and to the task. Quite backwards.

First, there is Henry Kendall: Physicist, mountaineer, aviator, concerned scientist. Henry will be remembered as one of the few people who first observed a fundamental layer in the structure of matter. There have been a number of great scientists and Nobel Laureates; but only a handful presided over drastic simplifications in the picture we have of nature. More than any other quality, I admire his intolerance of unnecessarily complicated and vague arguments (whether put forth by know-it-all students or heads of state). Hopefully, some of his genius for clear, simple, elegant explanations and robust design has been handed down.

I remember Wit Busza telling me that the Counter Spark-Chamber group "throws you in the deep end, and if you swim you come out a good physicist". This is true. We gulped, but didn't drown, thanks to Wit, as well as Jerry Friedman, Lou Osborne, Larry Rosenson, Frank Taylor, and Robin Verdier. All functioned as my advisors. Thanks especially to Frank for being on my thesis committee. Thanks go also to John Ryan for patiently enduring all my fiddling with his computer, trying to make pretty figures, and to Sandra Fowler, the group secretary, who mother-henned us quite ably from three thousand miles away.

As the youngest of the four students our group sent to SLAC, I endured a lot of elder-brothering from John, Saúl, and Dave. They did eventually get me to wear a watch and carry a wallet. Suzanne and Andrea made up for all of it with elder-sistering. Phil Burrows occasionally took me to the symphony and ballet to infuse a little culture. His rather interesting social life also provided grist for some juicy gossip. May all your pizzas be fresh and fungus-free.

The high quality of the data we collected is due to members of the Compton Polarimeter group, probably the most under-appreciated detector group in the Universe: Fearless Leader Mike Fero welcomed me into the group and let me squat in his office and and squeezed real work out of me; Morris Swartz knows more about electroweak theory (or any other kind of theory) than the theorists and explained it during lunch; Bruce Schumm and Mike Woods imparted what few analytic skills I do posses. I was indeed lucky to have such talented role models.

Dave Calloway knew the laser and every mirror and window it touched, and made pretty schematics we all greedily included in our theses. He will probably never ride in an electric cart with another Indian ever again. Fellow students Rob Elia and Ross King did a lot of the brainwork presented in this thesis. Both of them are also musically gifted, which I think is just plain unfair of nature. Most of our data would have fallen far short of being written on tape (we, of course, would have labored on blissfully unaware) were it not for Tom Junk, demigod. I was honored to be part of that cadre. It was a somewhat bracing pleasure to work with the new students, Eric Torrence, Kendall Reeves, and XiaoQing Yang and watch them pick up in hours and days what had taken me weeks and months to master. I wish them the similar successes. One day I may wish I was back among the Compton Cowboys, scanning, panicking, watching mirrors burn, enduring Marty. . . that, of course, will be the unambiguous sign I am going senile.

This work is dedicated to my mother, my father

and to Radha.

Ande Brahmandam (Within the minute, the cosmos).   *The Upanishads*

Contents

List of Figures

List of Tables

Chapter 1

Introduction and Physics Motivation

The left-right asymmetry, A_{LR}, is a highly sensitive probe of the electroweak sector of the Standard Model of Particles and Fields. The measurement of A_{LR} presented in this thesis was performed using the SLD detector at the Stanford Linear Collider (SLC) at the Stanford Linear Accelerator Center (SLAC). The SLC produced, accelerated and collided electrons with positrons at a center of mass energy of 91.26 GeV, producing Z bosons. The decay products of the Z bosons were detected by the SLD, situated at the e^+e^- Interaction Point of the SLC (SLC IP). The data used in the analysis presented in this thesis was obtained during the 1993 running period of the SLC/SLD program, which lasted from February to August of 1993.

A_{LR} is highly sensitive to the weak mixing angle, $\sin^2 \theta_W$. The measurement of A_{LR} and subsequent determination of the effective weak mixing angle, $\sin^2 \theta_W$, was the principal goal of the SLC/SLD program. The analysis presented herein constitutes the single most precise determination of $\sin^2 \theta_W$ available to date.

1.1   The Electroweak Standard Model

The theory of electroweak interactions introduced by Glashow, Weinberg, and Salaam [1] [2] [3] in the 1960s has been experimentally verified with increasing precision since the discovery of the predicted $W^{\pm}$ and Z bosons in 1981 [4].

1.1.1 The electroweak interaction

The electroweak interaction is the product of the successful unification of quantum electrodynamics (QED) with a theory of weak interactions. Weak interactions such as β-decay were traditionally viewed as four-point interactions with a coupling constant of G_F. The theory of Glashow, Weinberg and Salaam (GWS) cast them as exchanges of one or another of three bosons, labelled the $W^\pm$ and Z. The weak nature of the interaction arises naturally from the large mass of these bosons, $M_W = 80.22 \pm 0.26$ Gev, and $M_Z = 91.187 \pm 0.007$ GeV [5].

We present a short derivation of the main points of the theory, and introduce conventions used in later chapters. The theory begins with an introduction of a non-abelian gauge group with $SU(2) \times U(1)$ symmetry. The $SU(2)$ group is called the *weak isospin*. The $U(1)$ group is the *weak hypercharge*. The $SU(2)$ weak isospin group generator introduces three fields, $W_\mu^1, W_\mu^2, W_\mu^3$, and a conserved charge $T^\alpha, \alpha = 1, 2, 3$. The $U(1)$ weak hypercharge group generator introduces one field B_μ, and a conserved charge, Y.

The charges introduced by these fields are related to the electric charge by the expression

$$Q = T^3 + \frac{Y}{2},$$

where Q is the familiar conserved electric charge of QED. This yields the current relation

$$j_\mu^{em} = J_\mu^3 + \frac{1}{2} j_\mu^Y \tag{1.1}$$

among the electromagnetic current j_μ^{em}, the weak isospin current J_μ^α, and the weak hypercharge current j_μ^Y. The currents are defined as follows:

$$j_\mu^{em} = \bar{\psi}_f \gamma_\mu \psi_f$$
$$J_\mu^\alpha = \bar{\psi}_f \frac{1}{2} \gamma_\mu (1 - \gamma^5) T^\alpha \psi_f$$
$$j_\mu^Y = \bar{\psi}_f \gamma_\mu Y \psi_f \tag{1.2}$$

where $\psi, \bar{\psi}$ are Dirac spinors and the γ_μ are Dirac γ-matrices in the convention used by Halzen and Martin [6].

The basic electroweak interaction, in terms of the fields and currents defined, is now

$$-ig(J^\alpha)^\mu W_\mu^\alpha - i\frac{g'}{2}(j^Y)^\mu B_\mu, \tag{1.3}$$

where the coupling constants g and g' are introduced. The constant g is the coupling of the $SU(2)$

17

weak isospin field W_μ^α to the current J_μ^α and the constant g' is the coupling of the $U(1)$ weak hypercharge field B_μ to the current j_μ^Y.

The first two components of weak isospin combine to create the *charged weak isospin* component.

$$W_\mu^\pm = \sqrt{\frac{1}{2}}\left(W_\mu^1 \mp W_\mu^2\right)$$

The mass eigenstates of the $W_\mu^\pm$ fields, the charged weak vector bosons $W^\pm$, couple only to left-handed fermions due to the presence of the projection operator $1 - \gamma^5$ in the definition of the weak isospin current.

The third component of weak isospin combines with weak hypercharge to yield fields A_μ and Z_μ.

$$
\begin{aligned}
A_\mu &= B_\mu \cos\theta_W + W_\mu^3 \sin\theta_W \\
Z_\mu &= -B_\mu \sin\theta_W + W_\mu^3 \cos\theta_W
\end{aligned}
\tag{1.4}
$$

The mass eigenstates of A_μ and Z_μ are the photon and the Z boson, respectively. The mixing angle, θ_W, is an arbitrary parameter not predicted by the theory which must be determined experimentally. Since the photon is observed to couple to right-handed and left-handed fermions, the Z boson must as well, since they are both composed of the same fields.

We write the neutral-current component of the basic electroweak interaction introduced in Eq. 1.3, using the fields introduced in Eq. 1.4 as

$$
\begin{aligned}
-ig(J^3)^\mu W_\mu^3 - i\frac{g'}{2}(j^Y)^\mu B_\mu ={} & \\
& -i\left(g\sin\theta_W J_\mu^3 + g'\cos\theta_W \frac{j_\mu^Y}{2}\right)A^\mu \\
& -i\left(g\cos\theta_W J_\mu^3 - g'\sin\theta_W \frac{j_\mu^Y}{2}\right)Z^\mu.
\end{aligned}
\tag{1.5}
$$

We identify the field A_μ as the standard electromagnetic vector field, and the quantity in parenthesis before A^μ as the electromagnetic coupling and current. Taken with the current relation in Eq. 1.1, we obtain

$$g\sin\theta_W = g'\cos\theta_W = e,\tag{1.6}$$

where e, the electromagnetic charge, determines the coupling to the photon.

We see the two coupling constants, g and g', can be related to the weak mixing angle, θ_W. We can now use the current relation from Eq. 1.1 and the coupling constant relation from Eq. 1.6 and

express the weak part of the neutral current interaction from Eq. 1.5 as

$$-i\frac{g}{\cos\theta_W}J_\mu^{NC}Z^\mu \tag{1.7}$$

where the weak neutral current, J_μ^{NC} is given by

$$J_\mu^{NC} = J_\mu^3 - \sin^2\theta_W j_\mu^{em}. \tag{1.8}$$

Low energy, charged-current weak interactions: G_F

Low energy, charged current weak interactions have historically been described as a four-point interaction (as for instance in μ^--decay, where the four particles, μ^-, e^-, ν_μ, and $\bar{\nu}_e$, all interact at one point) with the empirical invariant amplitude

$$\mathcal{M}^{CC} = \frac{4G_F}{\sqrt{2}}J^\mu J_\mu^\dagger \tag{1.9}$$

where the current $J_\mu \equiv \frac{1}{2}(J_\mu^1 + iJ_\mu^2)$ and $G_F = 1.16637(2) \times 10^{-5}$ GeV^2, the Fermi coupling constant. We write the charged-current component of the basic electroweak interaction introduced in Eq. 1.3 as

$$-i\frac{g}{\sqrt{2}}(J^\mu W_\mu^+ + J^{\mu\dagger}W_\mu^-),$$

where $W_\mu^\pm$ have already been introduced, as the fields whose mass eigenstates are the charged W bosons. This leads to rewriting the amplitude for low-q^2 W-mediated charged-current interactions as

$$\mathcal{M}^{CC} = \left(\frac{g}{\sqrt{2}}J_\mu\right)\left(\frac{1}{M_W^2}\right)\left(\frac{g}{\sqrt{2}}J_\mu^\dagger\right). \tag{1.10}$$

Comparison of Eq. 1.9 with Eq. 1.10 leads to the (tree-level) relationship

$$\frac{G_F}{\sqrt{2}} = \frac{g^2}{8M_W^2}. \tag{1.11}$$

The V-A nature of the charged weak interaction is manifest in the $(1 - \gamma^5)$ left-handed projection operator which is part of the weak isospin interaction. We identify left-handed fermions as isodoublets of

$$T^3 = \begin{pmatrix} +\frac{1}{2} \\ -\frac{1}{2} \end{pmatrix}_L,$$

and right-handed fermions as isosinglets of $T^3 = 0$. Table 1.1 lists the isospin quantum numbers for the known quarks and leptons.

$$\begin{pmatrix} \nu_e \\ e \end{pmatrix}_L \quad \begin{pmatrix} u \\ d \end{pmatrix}_L \quad (e)_R \quad (u)_R \quad (d)_R$$

$$\begin{pmatrix} \nu_\mu \\ \mu \end{pmatrix}_L \quad \begin{pmatrix} c \\ s \end{pmatrix}_L \quad (\mu)_R \quad (c)_R \quad (s)_R$$

$$\begin{pmatrix} \nu_\tau \\ \tau \end{pmatrix}_L \quad \begin{pmatrix} t \\ b \end{pmatrix}_L \quad (\tau)_R \quad (t)_R \quad (b)_R$$

Table 1.1: The known fermions grouped in left-handed isodoublets of $T^3 = \pm\frac{1}{2}$ and right-handed isosinglets of $T^3 = 0$.

1.1.2 Boson masses and the Higgs mechanism

The bosons introduced in the preceeding section, the $W^\pm$ and the Z, mediate the weak charged and neutral currents. The very weakness of interactions involving these currents (at low q^2) has been attributed to the high mass of these bosons. To be completely successful, the theory must also predict (or at least accommodate) the observed masses. We briefly introduce a mechanism to generate these masses, called the Higgs mechanism [7]. We note that other mechanisms to generate boson masses have been proposed [8], but they will not be discussed in this thesis.

The basic electroweak interaction introduced in Eq. 1.3 is part of the electroweak Lagrangian

$$\begin{aligned}
\mathcal{L} = \ & -\frac{1}{4}\vec{W}_{\mu\nu}\vec{W}^{\mu\nu} - \frac{1}{4}\vec{B}_{\mu\nu}\vec{B}^{\mu\nu} \\
& + \bar{L}\gamma^\mu \left(i\partial_\mu - g\frac{1}{2}\vec{T}\cdot\vec{W}_\mu - g'\frac{Y}{2}B_\mu \right) L \\
& + \bar{R}\gamma^\mu \left(i\partial_\mu - g'\frac{Y}{2}B_\mu \right) R \\
& + \left| \left(i\partial_\mu - g\frac{1}{2}\vec{T}\cdot\vec{W}_\mu - g'\frac{Y}{2}B_\mu \right)\phi \right|^2 - V(\phi),
\end{aligned} \tag{1.12}$$

where the first two terms are the $W^\pm$, Z, and photon kinetic energies (the shorthand $\vec{X}_{\mu\nu} \equiv \partial_\mu X_\nu - \partial_\nu X_\mu$ has been introduced). The third and fourth terms are the fermion kinetic energies and their interaction with the bosons. Note that the left and right projection operators, $\frac{1}{2}(1 \pm \gamma^5)$, have been subsumed into the spinors, yielding left and right handed spinors L and R. The fifth and final term (including the $V(\phi)$ term), is due to the introduction of four scalar fields ϕ_i. The $V(\phi)$ term is called the Higgs potential. The term before it is necessary to maintain the $SU(2)_L \times U(1)_Y$ gauge invariance of the Lagrangian. In addition, gauge invariance of this expanded Lagrangian requires that the ϕ_i inhabit $SU(2)_L \times U(1)_Y$ multiplets, most conveniently chosen to be the $Y = 1$ isodoublet

$$\phi = \begin{pmatrix} (\phi_1 + i\phi_2)/\sqrt{2} \\ (\phi_3 + i\phi_4)/\sqrt{2} \end{pmatrix}.$$

We now choose the Higgs potential

$$V(\phi) = \mu^2 \phi^\dagger \phi + \lambda(\phi^\dagger \phi)^2 \qquad (1.13)$$

with $\mu^2 < 0$ and $\lambda > 0$, creating a locus of $V(\phi)$ minima for values of ϕ such that

$$\phi^\dagger \phi = \frac{1}{2}(\phi_1^2 + \phi_2^2 + \phi_3^2 + \phi_4^2) = -\frac{\mu^2}{2\lambda} \equiv \frac{1}{2}v^2.$$

We define the vacuum field

$$\phi_0 \equiv \sqrt{\frac{1}{2}} \begin{pmatrix} 0 \\ v \end{pmatrix}, \qquad (1.14)$$

and fluctuations from this vacuum

$$\phi(x) = \exp(i2\vec{T} \cdot \vec{\theta}/v) \begin{pmatrix} 0 \\ \frac{v+h(x)}{\sqrt{2}} \end{pmatrix}.$$

We have introduced the four independent fields $\theta_1 \theta_2 \theta_3$, and h. Since $\vec{\theta}$ only appears in the overall phase, we are free to gauge it away, leaving

$$\phi(x) = \sqrt{\frac{1}{2}} \begin{pmatrix} 0 \\ v + h(x) \end{pmatrix}. \qquad (1.15)$$

We take the form of the field in Eq. 1.15 and the potential as defined in Eq. 1.13 and substitute into the Lagrangian in Eq. 1.12. We obtain terms $\frac{1}{2}(\partial_\mu h)^2$ and $-\lambda v^2 h^2$, corresponding to the kinetic energy and mass terms of the scalar particle, h. We call this particle the *Higgs particle*. By substituting the vacuum expectation value of the Higgs field from Eq. 1.14 into the Lagrangian, we obtain

$$\mathcal{L} = \left(\frac{1}{2}vg\right)^2 W_\mu^+ W^{\mu-} + \frac{1}{8}v^2 \left[gW_\mu^3 - g'B_\mu\right]^2 + 0\left[g'W_\mu^3 - gB_\mu\right]^2$$

where the first term is to be compared to expected mass term for a charged boson, $M_W^2 W^+ W^-$, giving

$$M_W = \frac{1}{2}vg, \qquad (1.16)$$

and the last two terms, chosen to be orthogonal in the (W_μ^3, B_μ) basis, are identified with the Z_μ and A_μ mass terms, yielding, upon normalization,

$$A_\mu = \frac{g'W_\mu^3 + gB_\mu}{\sqrt{g^2 + g'^2}} \text{ with } M_A = 0$$

$$Z_\mu = \frac{gW_\mu^3 + g'B_\mu}{\sqrt{g^2 + g'^2}} \text{ with } M_Z = \frac{1}{2}v\sqrt{g^2 + g'^2}. \quad (1.17)$$

We now use the relationship of Eq. 1.6 in terms of the weak mixing angle θ_W. We can relate M_W from Eq. 1.16 and M_Z from Eq. 1.17 and obtain the result

$$\frac{M_W}{M_Z} = \cos\theta_W. \quad (1.18)$$

The Higgs mechanism not only generates the masses of the bosons from the mixed weak isospin and weak hypercharge fields, but also makes a testable prediction for the ratio of the masses of the charged and neutral bosons in terms of the mixing angle. Unfortunately, the masses themselves are not predicted by the theory, and must be determined experimentally.

1.1.3 Electroweak parameters

In the preceeding sections, we have introduced the $SU(2)$ weak isospin field with coupling g and the $U(1)$ weak hypercharge field with coupling g', as well as the Higgs field with a vacuum expectation value $\langle\phi_0\rangle$. These parameters are not directly measurable, so we must choose the tree-level Standard Model relations to define a complete set of *observable* parameters. We naturally choose parameters with the smallest associated measurement uncertainties. From Eq. 1.6 we obtain

$$\alpha = \frac{g^2 g'^2}{4\pi(g^2 + g'^2)},$$

where $\alpha = e^2/4\pi$ is the electromagnetic fine-structure constant. Equations 1.9 and 1.11 yield

$$G_F = \frac{1}{2\sqrt{2}\langle\phi_0\rangle^2},$$

and equations 1.14 and 1.17 give us

$$M_Z = \frac{1}{\sqrt{2}}\langle\phi_0\rangle\sqrt{g^2 + g'^2}.$$

The measured values of these observables [5] are shown in Table 1.2.

We note that the value listed for the electromagnetic fine-structure constant, α, is that determined at $q^2 = 0$. At higher energies, such as $q^2 = M_W^2 \, or \, M_Z^2$, the running nature of the coupling constant raises the value to $\alpha(q^2 = M_Z^2) \approx 1/128$. The value at these higher values of q^2 is not nearly as precisely determined, and constitutes the main theoretical uncertainty in precision tests of the

22

Observable	Value	Precision (ppm)
$\alpha(q^2 = 0)$	1/137.0359895(61)	0.045
G_F	$1.16639(2) \times 10^{-5}$ GeV^{-2}	20
M_Z	91.187(7) GeV	77

Table 1.2: Complete set of tree-level electroweak observables.

Standard Model at $q^2 = M_Z^2$. This running of the coupling constant is a consequence of effects beyond the tree-level. In addition to the parameters listed in Table 1.2, the fermion masses and the Higgs scalar boson mass are not specified in the Standard Model. These quantities also appear in radiative corrections to the tree-level processes, and effect the value of precision electroweak measurements. A sufficiently precise measurement of an electroweak observable can be sensitive to these corrections, and yield insight into unknown or poorly known parameters such as the Higgs mass and top quark mass.

1.2 The Process $e^+e^- \rightarrow Z \rightarrow f\bar{f}$

The Z boson defined in the last section is a neutral vector particle, similar to the photon. The main differences from the photon lie in the large mass of the Z, and the couplings to fermion currents. Any process that contains a *virtual* photon propagator can have that propagator replaced by a Z and remain a valid process. The process $e^+e^- \rightarrow \gamma \rightarrow f\bar{f}$, is an example. In this process, q is the momentum of the virtual vector boson. The propagators for the photon and Z are

$$\frac{-ig_{\mu\nu}}{q^2} \quad : \quad \gamma \text{ propagator},$$

$$\frac{-ig_{\mu\nu} + \frac{iq_\mu q^\nu}{M_Z^2}}{q^2 - M_Z^2} \quad : \quad Z \text{ propagator},$$

We see that at values of $q^2 \ll M_Z^2$, the photon propagator dominates. However, at q^2 approaches M_Z^2, the Z propagator becomes singular. This is referred to as the Z *pole*, and the mass term in the denominator is modified, $M_Z^2 \rightarrow M_Z^2(1 + i\Gamma_Z/M_Z)$, in order to avoid the singularity.
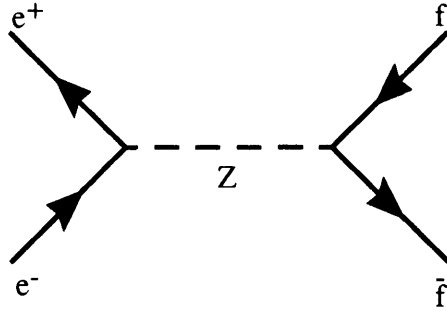
Figure 1-1: The tree-level Feynman diagram for $e^+e^- \rightarrow Z \rightarrow f\bar{f}$.

1.2.1 Coupling of the Z to fermions

We now examine the coupling of the Z propagator to fermion currents. From equations 1.7 and 1.8 we obtain the neutral current interaction for $Z \rightarrow f\bar{f}$:

$$- i\frac{g}{\cos\theta_W} \bar{\psi}_f \gamma^\mu \left[\frac{1}{2}(1 - \gamma^5)T_f^3 - \sin^2\theta_W Q_f\right] \psi_f Z_\mu. \tag{1.19}$$

Figure. 1-1 shows the Feynman diagram for the process $e^+e^- \rightarrow Z \rightarrow f\bar{f}$. There are two vertices of the type described by Eq. 1.19. The *initial* vertex is the coupling of the Z propagator to the electron current. The *final* vertex is the coupling to the final state fermion-antifermion pair. The vertex factor is conventionally expressed in terms of vector and axial-vector coupling constants to the Z:

$$- i\frac{g}{\cos\theta_W}\gamma^\mu\frac{1}{2}\left(c_v^f - c_a^f\gamma^5\right), \tag{1.20}$$

where

$$
\begin{aligned}
c_v^f &= T_f^3 - 2Q_f\sin^2\theta_W \\
c_a^f &= T_f^3
\end{aligned}
\tag{1.21}
$$

and Q_f is the charge of the fermion and T_f^3 is the third component of its weak isospin as listed in Table 1.1. The vector and axial-vector coupling constants are listed in Table 1.2.1.

1.2.2 The Z production cross section

The resonant production of Z bosons gives rise to a large peak in the $e^+e^- \rightarrow f\bar{f}$ cross-section at $q^2 = M_Z^2$. At low values of $\sqrt{s}$ the process is dominated by the photon. However, the $1/q^2$ dependence of the photon propagator suppresses this contribution at higher $\sqrt{s}$. At the Z peak

fermion	c_v^f	c_a^f
ν_e, ν_μ, ν_τ	$\frac{1}{2}$	$\frac{1}{2}$
e^-, μ^-, τ^-	$-\frac{1}{2}$	$-\frac{1}{2} + 2\sin^2\theta_W$
u, c, t	$\frac{1}{2}$	$\frac{1}{2} - \frac{4}{3}\sin^2\theta_W$
d, s, b	$-\frac{1}{2}$	$-\frac{1}{2} + \frac{2}{3}\sin^2\theta_W$

Table 1.3: Vector and axial-vector couplings for Fermion-Z.

at $\sqrt{s} = 91.2$ GeV, the contribution from the Z propagator ~ 800 times that from the photon. Therefore, we justifiably ignore pure photon-exchange terms in calculating the cross section. In addition, the $\gamma - Z$ exchange terms also vanish at the Z pole. This leaves only the pure Z exchange terms. However, some small correction ($\approx 2\%$) for the $\gamma - Z$ exchange terms must be made due to initial state radiation effects. We now derive the cross section for the process $e^+e^- \rightarrow Z$ where the electron beam is polarized. We define the polarization, $\mathcal{P}$, in a given direction n, as follows:

$$\mathcal{P}(\hat{n}) = \frac{N_e(s, n \text{ parallel}) - N_e(s, n \text{ antiparallel})}{N_e(s, n \text{ parallel}) + N_e(s, n \text{ antiparallel})},\tag{1.22}$$

where $\hat{s}$ is the direction of the electron spin-vector. In what follows, we choose n such that the magnitude of $\mathcal{P}$ is maximized. We then define $\mathcal{P}_z$ as the longitudinal polarization (in the direction of the momentum vector, $\vec{p}$), and $\mathcal{P}_t$ as transverse polarization. We write the polarization dependent cross section for $e^+e^- \rightarrow f\bar{f}$ at the Z-pole.

$$
\begin{aligned}
\frac{d\sigma}{d\Omega} = {} & \frac{\alpha^2}{4\sin^4 2\theta_W} \times \frac{s}{(s - M_Z)^2 + \Gamma_Z^2 s^2/M_Z^2} \times \\
& \left\{ (1 - \mathcal{P}_z^+\mathcal{P}_z^-)\left[(1 + c^2)\left(c_v^{e\,2} + c_a^{e\,2}\right)\left(c_v^{f\,2} + c_a^{f\,2}\right) - 8cc_v^e c_a^e c_v^f c_a^f\right] \right. \\
& + (\mathcal{P}_z^+ - \mathcal{P}_z^-)\left[2(1 + c^2)c_v^e c_a^e\left(c_v^{f\,2} + c_a^{f\,2}\right) + 4c\left(c_v^{e\,2} + c_a^{e\,2}\right)c_v^f c_a^f\right] \\
& \left. + \mathcal{P}_t^+\mathcal{P}_t^- \cos\Phi(1 - c^2)\left(c_v^{e\,2} + c_a^{e\,2}\right)\left(c_v^{f\,2} + c_a^{f\,2}\right) \right\}
\end{aligned}\tag{1.23}
$$

where c is the cosine of the polar angle of the outgoing fermion. We have allowed for positron polarization: $\mathcal{P}_z^+, \mathcal{P}_t^+$ are the longitudinal and transverse polarization of the positron beam, defined in the same way as for the electron beam, with $\mathcal{P}_z = +(-)1$ corresponding to right (left) handed particles. The angle Φ is defined by $\Phi = 2\phi - \phi^- - \phi^+$, where ϕ is the azimuthal angle of the outgoing fermion and $\phi^\pm$ the azimuth of the electron and positron transverse polarization direction.

At the SLC, only the electron beam is polarized (we will discuss the case of possible positron polarization in section 9.1), and the polarization is entirely longitudinal. In this case, Eq. 1.23

simplifies to

$$\frac{d\sigma}{d\Omega} = k\left\{\left[(1+c^2)\left(c_v^{e\,2}+c_a^{e\,2}\right)\left(c_v^{f\,2}+c_a^{f\,2}\right)-8cc_v^e c_a^e c_v^f c_a^f\right]\right.$$
$$\left.-\mathcal{P}_z^-\left[2(1+c^2)c_v^e c_a^e\left(c_v^{f\,2}+c_a^{f\,2}\right)+4c\left(c_v^{e\,2}+c_a^{e\,2}\right)c_v^f c_a^f\right]\right\}, \qquad (1.24)$$

with

$$k \equiv \frac{\alpha^2}{4\sin^4 2\theta_W}\cdot\frac{s}{(s-M_Z)^2+\Gamma_Z^2 s^2/M_Z^2}$$

The pure photon propagator can be neglected near the Z-pole. We now consider the $\gamma - Z$ interference term

$$\left.\frac{d\sigma}{d\Omega}\right|_{\gamma-Z} = -2Q_f\left(1-\frac{M_Z^2}{s}\right)k\left\{\left[(1+c^2)c_v^e c_v^f + 2cc_a^e c_a^f\right]-\mathcal{P}_z^-\left[(1+c^2)c_a^e c_v^f + 2cc_v^e c_a^f\right]\right\}, \quad (1.25)$$

where Q_f is the charge of the outgoing fermion. This term vanishes at the Z-pole, but as we noted earlier, the effects of initial state radiation ensure that no collider can run exactly on the pole, hence the interference effects necessitate a correction to any electroweak observable measured near the pole.

1.3 Electroweak Asymmetries

The differential cross section in Eq. 1.24 has a polarization dependent part, the sign of which depends upon the sign of $\mathcal{P}_z^-$. In addition, both the polarization dependent and independent parts have terms that are symmetric and antisymmetric in polar angle, leading to a difference in cross section for Z decays between the forward and backward hemispheres. We discuss these differences in cross section, and create electroweak observables that are sensitive to the Z-fermion coupling constants at the intial and final vertices.

We avoid the systematic uncertainties inherent in measuring the absolute cross section by forming ratios of differences of cross sections. Cross sections with different initial or final state characteristics (such as beam polarization or polar angle of decay) are chosen . Such ratios are called electroweak asymmetries, and terms in the cross sections which do not depend on the characteristic being changed divide away, significantly reducing the systematic uncertainty in the measurement of the observable.

26

1.3.1 Forward-backward asymmetry

Forward-backward asymmetries are sensitive to the polar angle anti-symmetric term in the cross section (Eq. 1.24). The conventional forward-backward asymmetry does not require the use of polarized beams to create the Z. We define the forward-backward asymmetry for the process $e^+e^- \rightarrow f\bar{f}$ as

$$A_{FB}^f \equiv \frac{\int_0^{c_0} \frac{d\sigma_f}{dc} dc - \int_{-c_0}^0 \frac{d\sigma_f}{dc} dc}{\int_{-c_0}^{c_0} \frac{d\sigma_f}{dc} dc}, \qquad (1.26)$$

where the c is the polar angle and $\pm c_0$ are the integration limits in c. The σ_f term in the cross section necessitates an identifiable final state decay channel. In practice, this is usually the $\mu^+\mu^-$ or $b\bar{b}$ channel. Upon integration of Eq. 1.24 we obtain

$$A_{FB}^f = \frac{4c_0}{3 + c_0^2} \cdot \frac{3c_a^\epsilon c_v^\epsilon c_a^f c_v^f}{\left(c_v^{\epsilon\,2} + c_a^{\epsilon\,2}\right)\left(c_v^{f\,2} + c_a^{f\,2}\right)}. \qquad (1.27)$$

We introduce the notation

$$A_f \equiv \frac{2c_a^f c_v^f}{c_v^{f\,2} + c_a^{f\,2}}, \qquad (1.28)$$

and obtain for the forward-backward asymmetry:

$$A_{FB}^f = \frac{3}{4} \cdot \frac{4c_0}{3 + c_0^2} \cdot A_\epsilon \cdot A_f. \qquad (1.29)$$

1.3.2 τ-polarization asymmetry

The dependence of the cross section on helicity of the electron current at the initial vertex is mirrored at the final vertex. However, determination of the helicity of the final state fermions is difficult. For the quark final states, the subsequent hadronization of the quarks into jets dilutes the helicity information beyond hope of measurement. The $\mu^+\mu^-$ and e^+e^- final states do not decay at all, making helicity determination impossible. Decays to $\tau^+\tau^-$ however, offer some hope of determining the helicity information of the final state.

Decay products of the τ lepton exhibit characteristic distributions in polar angle depending on the helicity of the τ. Using this information, one can make a determination of the final-state polarization. We define the final state polarization of a Z decay at a particular polar angle to be

$$\mathcal{P}_f(c) \equiv \frac{\frac{d\sigma}{d\Omega}(f_L) - \frac{d\sigma}{d\Omega}(f_R)}{\frac{d\sigma}{d\Omega}(f_L) + \frac{d\sigma}{d\Omega}(f_R)},$$

where f_L and f_R denote left- and right-handed final state fermions. Substitution of terms from the

27

cross section in Eq. 1.24 yields

$$P_f(c) = \frac{2A_e c + A_f(1+c^2)}{(1+c^2) + 2A_e A_f c},$$

where c is the cosine of the polar angle. Upon integration over symmetric polar angle limits we obtain

$$\langle P_f \rangle = A_f$$

In this case, the final state fermion f is the τ lepton. Therefore the τ-polarization analysis is sensitive to A_τ, a function of the coupling constants at the final vertex only.

1.4 The Left-Right Asymmetry

The left-right asymmetry, A_{LR}, differs from the asymmetries defined in the previous section in that it probes the coupling constants at the initial vertex. It requires longitudinal polarization of the beam, but does not make any requirements of the final state, except that it not be e^+e^-. The process $e^+e^- \rightarrow e^+e^-$ can proceed through a t-channel photon exchange. The photon exchange amplitude interferes with the s-channel amplitude corresponding to the Z-exchange process we wish to observe, and dilutes the measured asymmetry. However, all other lepton final states of Z decay are acceptable, as are all the quark final states. This gives A_{LR} a statistical advantage over asymmetries which use a specific lepton or quark final state.

The left-right asymmetry is defined as

$$A_{LR} \equiv \frac{\sigma(e^+_R e^-_L \rightarrow Z \rightarrow f\bar{f}) - \sigma(e^+_L e^-_R \rightarrow Z \rightarrow f\bar{f})}{\sigma(e^+_R e^-_L \rightarrow Z \rightarrow f\bar{f}) + \sigma(e^+_L e^-_R \rightarrow Z \rightarrow f\bar{f})}$$

$$A_{LR} \equiv \frac{\sigma_L - \sigma_R}{\sigma_L + \sigma_R} \tag{1.30}$$

where σ_L and σ_R are the the shorthand notation to denote the total Z cross section using left- and right-handed polarized electrons respectively. We note that since the Z is a vector boson, the helicity of the positron used in the annihilation is opposite that of the electron, in the center of mass frame.

We obtain the total cross section $\sigma_{L,(R)}$ by integrating Eq. 1.24 over the solid angle and taking the longitudinal electron beam polarization (P_z^-) to be $-(+)1$. The effect of finite beam polarization $(P < 1.0)$ appears as a linear dilution term. If we assume that the machine luminosity, the beam polarization and energy, and the detector efficiency have no left-right bias, and there is no

28

polarization of the positron beam, then we can write a simple equation,

$$A_{LR} = \frac{1}{\mathcal{P}_e} \cdot \frac{N_L - N_R}{N_L + N_R} \equiv \frac{1}{\mathcal{P}_e} \cdot A_m,$$ (1.31)

where $N_L(N_R)$ are the number of Z decay events detected when the electron beam had left- (right-) handed helicity. $\mathcal{P}_e$ is the beam polarization. We define A_m as the *measured asymmetry*. We can also write the corresponding error on A_{LR} as

$$\delta A_{LR} = \sqrt{\frac{1}{\mathcal{P}_e^2 N_{Tot}} + A_{LR}^2 \left(\frac{\delta \mathcal{P}_e}{\mathcal{P}_e}\right)},$$ (1.32)

where $N_{Tot} = N_L + N_R$ is the total number of Z events. We have ignored terms of order $\mathcal{O}(A_{LR}^2)$ and higher. The first term in the square root is the statistical error term; the second is the systematic error term. We note that the dominant systematic error in A_{LR} is the error in the beam polarization measurement.

Obviously, Eq. 1.31 is too simplistic, the beam parameters assumed to be symmetric with respect to left- and right-handed beam need not be. Also, there may be finite positron polarization. The effects of these biases in the beam parameters have been investigated, and will be discussed in detail in section 9.1. Using conservative estimates of the beam biases, we find that their combined effect on A_{LR} is less than 0.1%, relative. The main systematic uncertainties in the A_{LR} measurement are associated with the determination of beam polarization and backgrounds in the Z event sample — in other words, determination of $\mathcal{P}_e$, N_L and N_R.

The left-right asymmetry is sensitive to the initial vertex coupling constants only,

$$A_{LR} = A_e = \frac{2c_v^e c_a^e}{c_v^{e\,2} + c_a^{e\,2}}.$$

Since A_{LR} is independent of the Z decay final state, we can use all quark and lepton final states of the Z, with the exception of e^+e^- final states, (Bhabha events). The dependence of A_{LR} on the vertex couplings is similar to that of the τ-polarization. Assuming lepton universality, $A_\tau = A_{LR}$. The value expected for A_τ and A_{LR} within the Standard Model is $\sim 14\%$. This large value of the asymmetry arises because only a single power of the vector coupling, c_v, appears in the numerator. Forward-backward asymmetries suffer from having the vector coupling from both the initial and final vertex in the numerator, with the result that most forward-backward asymmetries are $\sim 2\%$ for lepton final states.

In the final section of this chapter, we investigate the dependence of A_{LR} on $\sin^2 \theta_W$ detail. We note here that the A_{LR} and $\mathcal{P}_\tau$ are quite sensitive to $\sin^2 \theta_W$, with $\delta A_{LR} = \delta \mathcal{P}_\tau \approx 7.9 \cdot \sin^2 \theta_W$.
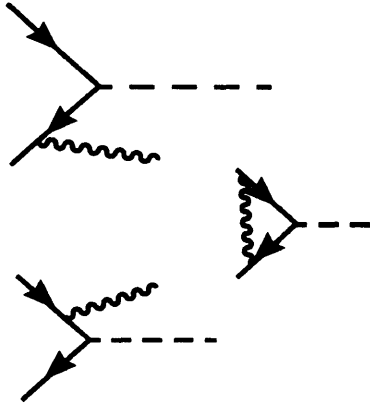
Figure 1-2: Feynman diagrams for first-order initial state radiation correction terms for the interaction $e^+e^- \to Z$.

The forward-backward asymmetries are significantly less sensitive, with $\delta A_{FB}^{\text{lepton}} \approx 1.5 \cdot \sin^2 \theta_W$ and $\delta A_{FB}^{b-quark} \approx 5.6 \cdot \sin^2 \theta_W$.

1.5 Radiative correction

The cross section for the $\gamma - Z$ interference term has already been presented in Eq. 1.25. The contribution from interference terms vanishes at the Z pole, where $\sqrt{s} = M_Z$. However, photons coupling to the initial electron current can move $\sqrt{s}$ off the Z-pole, where interference terms can contribute. Additionally, higher order terms can affect both the initial and final Z vertex, as well as the propagator. In this section, we investigate higher order correction to Z production and decay.

1.5.1 Initial state radiation

In e^+e^- annihilation, there is a finite probability for the electron or positron to emit a photon before interacting. This interaction is called *initial state radiation* and has the effect of lowering $\sqrt{s}$, the center-of-mass energy. Fig. 1-2 shows the Feynman diagrams for processes responsible for the leading-order initial state radiation correction to the Z cross section [9].

In order to calculate the effects of initial state radiation on the observed cross section, Bonneau and Martin [10] calculated the electron structure function $D_e(x, s)$, which is the probability of an electron (or positron) of center-of-mass energy $\sqrt{s}$ retaining a fraction x of its energy after emitting a photon. The corrected cross section is then

$$\sigma_{corr} = \int_0^1 D_e(x_1, s) dx_1 \int_0^1 D_e(x_2, s) dx_2, \tag{1.33}$$
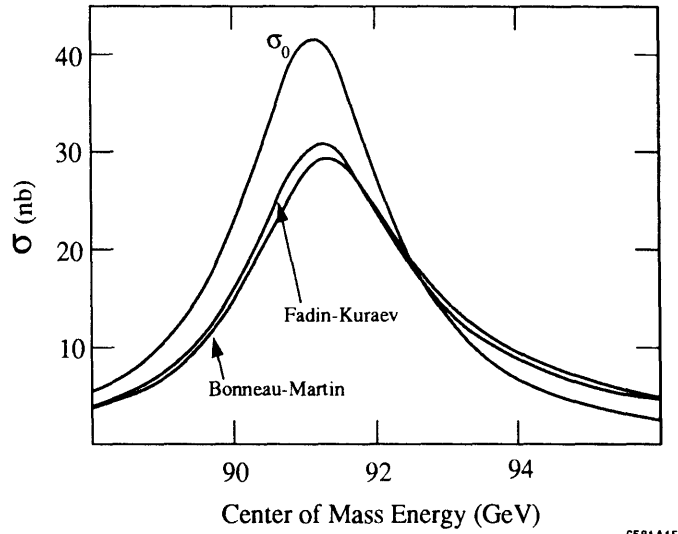
Figure 1-3: Cross-section for the process $e^+e^- \to f\bar{f}$ near the Z pole, for the Born (σ_0), first-order (Bonneau and Martin), and second order (Fadin and Kuraev) corrections.

where $x_{1(2)}$ is the energy retained by the electron (positron) after initial state radiation.

The calculation by Bonneau and Martin was to leading order only, incorporating the diagrams in Fig. 1-2. These terms led to a correction of $\sim 29\%$ in the peak cross section. Such a large correction indicates that second order terms need to be included in the correction. The calculation by Fadin and Kuraev [11] incorporates second order correction and yields

$$D_e(x) = \frac{\beta}{2}(1-x)^{\frac{\beta}{2}-1}\left[1 + \frac{3}{8}\beta\right] - \frac{1}{4}\beta(1+x)$$

$$\text{where } \beta = \frac{2\alpha}{\pi}\left(\log\frac{s}{m_e^2} - 1\right)\Big|_{s=M_Z^2} = 0.108 \tag{1.34}$$

for the electron structure function. The term before the square brackets is from the first order structure function of Bonneau and Martin. Fig. 1-3 shows a plot of the cross section versus $\sqrt{s}$ for the process $e^+e^- \to Z$. The uncorrected cross section is compared to the first-order corrected cross section of Bonneau and Martin and the first-and-second order correction of Fadin and Kuraev.

Initial state radiation lowers the center of mass energy of the initial state e^+e^-. The integrations in Eq. 1.33 are taken over the entire range of emitted photon energy. The lower limit, 0, is obtained when the electron or positron retains all its initial energy, while the upper limit, 1, is obtained when the electron or positron loses all its initial energy to initial state radiation. These limits are not strictly correct if the Z selection process imposes total-energy and geometrical event-symmetry criteria for accepting Z events, as indeed the event selection for A_{LR} does (see section 8.2). In such a case, the upper limit on the integrations in Eq. 1.33 must be changed to be commensurate with the selection criteria, since if either the electron or the positron (or both) radiate away a significant

31
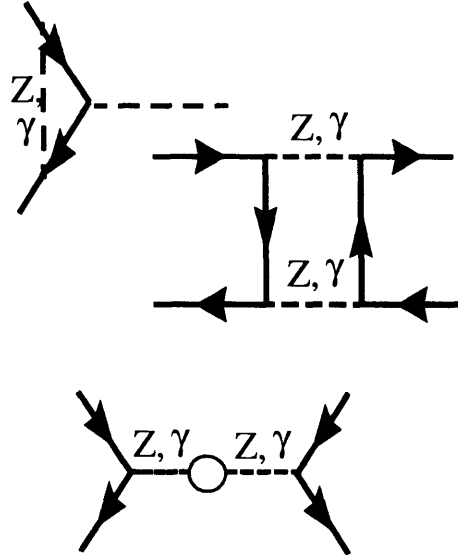
Figure 1-4: Feynman diagrams illustrating virtual QED, electroweak corrections. Vertex corrections (top); Box-diagram corrections (middle); and vacuum-fluctuation loop (*oblique*) corrections to the propagator (bottom).

portion of their initial energy, the event may no longer pass total-energy or event-symmetry cutoffs necessary to be included in the Z sample.

The effects of event-selection cuts have been incorporated into the calculation of the initial state radiation correction, and shown to have a negligible effect on the calculation [12]. The total effect of initial state radiation on A_{LR} is small. There is a small (few hundred MeV) shift in the energy dependence of A_{LR}, but due to the weak energy dependence of A_{LR} near the Z pole, the correction to A_{LR} is only $\approx 2\%$ of the measured value.

1.5.2 Virtual correction

Virtual corrections consist of vertex corrections, propagator corrections, and box-diagram corrections. Of the three, propagator corrections are the most interesting, since they introduce couplings to Standard Model elements such as the top quark [13] and Higgs particle through loop corrections to the tree-level propagator. Fig. 1-4 shows typical Feynman diagrams for the three types of virtual corrections.

Vertex and box corrections

Vertex corrections arise from the coupling of virtual γ, Z, or W boson to the fermion current at the $Z - f\bar{f}$ vertex. The effects of such corrections on A_{LR} is small, $\approx 2\%$, and reasonably well

32

understood. Similarly, the effects of box diagrams has also been calculated and found to contribute a negligible amount ($< 0.5\%$) to A_{LR}.

Propogator corrections

Vacuum polarization loop that leads to modification of the tree-level propagator can incorporate any allowed current in the loop. These corrections are also referred to as *oblique* corrections since they effectively modify the coupling constants, as opposed to the direct corrections to the interaction from the vertex and box diagrams.

Oblique corrections due to Standard Model effects have been calculated. The primary modification that must be made is the well known "running" of the coupling constants with energy. The electromagnetic coupling constant, α, changes from $\approx 1/137$ at $q^2 = 0$ to $\approx 1/128$ at $q^2 = M_Z^2$. Additional changes to the coupling constants occur due to a fermion current in a vacuum fluctuation loop.

If we neglect the effect of running coupling constant, the oblique corrections due to known and expected effects — such the ones due to the known quarks, and leptons and the MSM Higgs boson — are small but significant, since the masses of the particles created in the vacuum fluctuation loops appear in the formulation of the correction. Oblique corrections make A_{LR} sensitive to the as-yet poorly determined top quark mass and the unknown Higgs boson mass.

Several schemes exist that parameterize oblique corrections to electroweak observables in a general way, making very few assumptions about the currents in the vacuum fluctuation loops. One such scheme, due to Peskin and Takeuchi, parameterizes oblique corrections assuming only that the $SU(2) \times U(1)$ symmetry of the electroweak sector Lagrangian, and the so-called *custodial* $SU(2)$ symmetry of the Higgs symmetry-breaking sector hold. Given these assumptions, oblique corrections can be parameterized in three variables, called S, T, and U, whose are close to zero if only Standard Model expectations are included. Any deviation of these variables from zero may be an indication of phenomena beyond the Standard Model. Appendix A explores the significance of these variables in more detail.

1.5.3 Corrected A_{LR}

The electroweak corrections listed in the previous sections were calculated by the ZFITTER [14] program. The effects of initial state radiation, as well as direct and oblique electroweak corrections discussed in the previous sections, were all incorporated into the program. As mentioned previously,
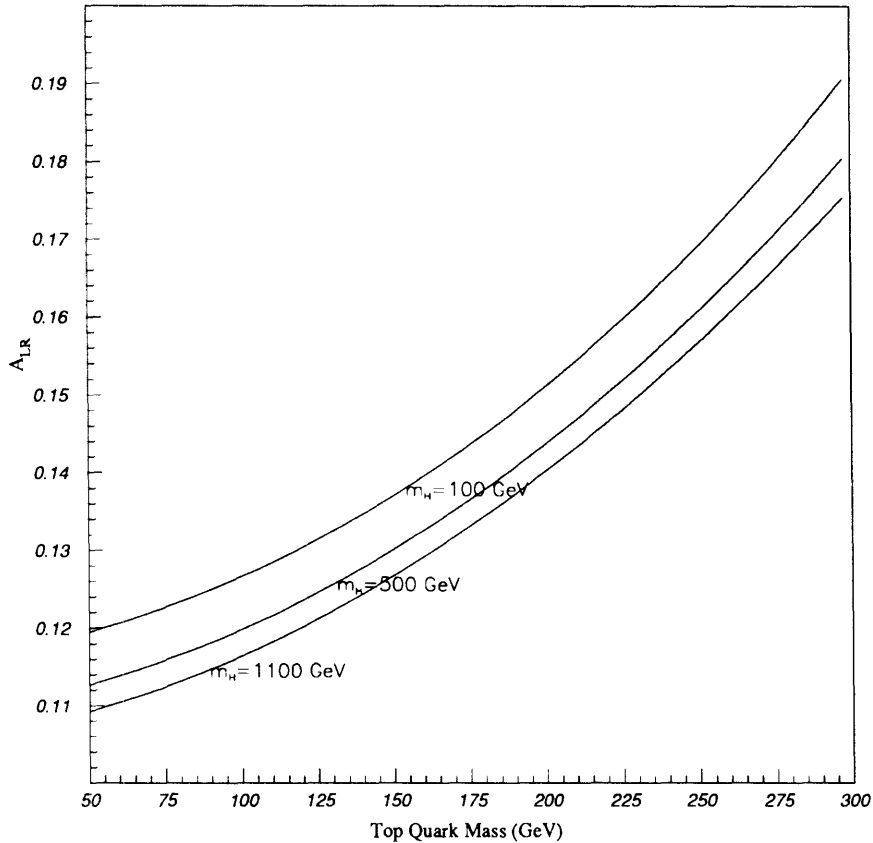
Figure 1-5: Expected values of A_{LR} versus the top quark and Higgs Boson mass from the Standard Model.

the calculation of the initial state radiation correction incorporated the effect of event acceptance criteria.

Once all the corrections have been made, we can examine the size of the correction. Fig. 1-5 shows the dependence of A_{LR} on the masses of the top quark and Higgs boson. When combined with other precise electroweak measurements with different dependencies on the top quark and Higgs boson masses, A_{LR} can be used to determine these masses with some precision.

1.5.4 Sensitivity to corrections and weak mixing angle

The direct and oblique corrections discussed in the previous sections have a larger relative effect on some electroweak observables than on others. Since lepton forward-backward asymmetries measure a small asymmetry, direct and oblique effects beyond tree-level constitute a larger relative correction to these asymmetries than to the A_{LR} or τ-polarization.

34

The sensitivity of the various asymmetry measurements to the weak mixing angle is found by differentiating the equations relating the observables to c_v and c_a, after proper substitution for c_v in terms of $\sin^2 \theta_W$ has been made. We note that the relation between the coupling constants and the weak mixing angle given in Eq. 1.21 is correct for tree-level expressions only. As noted before, the effects of corrections can be thought of as changes to the coupling constants. Another definition of the weak mixing angle uses the masses of the weak bosons. Yet another definition uses the precisely determined parameters α, G_F, and M_Z, where α has been allowed to run up to $q^2 = M_Z^2$. We present the various definitions in some detail.

The weak mixing angle at tree level

The tree-level expression for $\sin^2 \theta_W$, in terms of the gauge couplings g and g' are given by

$$\sin^2 \theta_W^{bare} \equiv \frac{g'^2}{g'^2 + g^2}. \tag{1.35}$$

No experiment measures this bare value of the mixing angle, just as no experiment measures the bare value of the QED electric charge, ϵ.

s_*^2 of Kennedy and Lynn

The vertex corrections to the tree level process can be divided into two sets. The first set are called *universal* corrections, and consist of corrections independent of fermion flavor. The second set, *non-universal* corrections, depend on the fermion flavor. Kennedy and Lynn [15] have shown that the effects of oblique corrections and a particularly defined set of universal corrections can be absorbed into the definition of the propagator and vertex couplings. The form of the interactions remain the same. The neutral current Lagrangian can be rewritten in terms of these modified elements. We can then extract the left-right asymmetry, correct for all orders of vacuum polarization and most universal vertex corrections

$$A_{LR}(q^2) = \frac{2\left[1 - 4s_*^2(q^2)\right]}{1 + \left[1 - 4s_*^2(q^2)\right]} \tag{1.36}$$

This quantity is close to that measured by experiment; the discrepancies arising from the non-universal vertex corrections and box diagrams are small.

s_s^2 of Sirlin

One definition, due to Sirlin [16] defines the weak mixing angle as

$$s_s^2 \equiv 1 - \frac{M_W^2}{M_Z^2}.$$ (1.37)

This quantity is limited in precision by the measurement of M_W. Currently, $M_W = 80.22 \pm 0.26$ GeV. This yields a value of

$$s_s^2 = 0.2261 \pm 0.0050,$$

which is surpassed by the precision of the electroweak asymmetry measurements. The Sirlin definition is also referred to as the *on-shell scheme*.

s_0^2 of Lynn, Peskin, and Stuart

A definition of the weak mixing angle in terms of well defined constants is suggested by Lynn, Peskin and Stuart [17] as

$$s_0^2(1 - s_0^2) \equiv \frac{4\pi\alpha_*}{\sqrt{2}G_F M_Z^2},$$ (1.38)

where the electromagnetic coupling constant has been allowed to run from $\alpha \approx 1/137$ to a value calculated [18] to be $\alpha_* = \alpha(M_Z^2) = 1/(128.80 \pm 0.12)$. Eq. 1.38 now yields

$$s_0^2 = 0.23135 \pm 0.00031,$$

where the dominant error is in the running of the coupling constant α. The value of s_0^2 serves as a Standard Model reference value for the mixing angle.

The effective weak mixing angle, $\sin^2 \theta_W^{\text{eff}}$

We choose a definition of the weak mixing angle strictly defined at the Z pole,

$$A_{LR}(q^2 = M_Z^2) \equiv \frac{2\left[1 - 4\sin^2\theta_W^{\text{eff}}\right]}{1 + \left[1 - 4\sin^2\theta_W^{\text{eff}}\right]} = A_e^0,$$ (1.39)

where $\sin^2\theta_W^{\text{eff}}$ is the *effective* weak mixing angle. A_e^0 is the effective eZ coupling asymmetry, which yields effective vector and axial vector coupling constants

$$A_e^0 = \frac{2c_v^{e\,\text{eff}} c_a^{e\,\text{eff}}}{c_v^{e\,\text{eff}\,2} + c_a^{e\,\text{eff}\,2}},$$

using the same relations as Eq. 1.28.

The effective weak mixing angle incorporates direct and oblique corrections, including both universal and non-universal vertex corrections and box diagrams. The corrections due to initial state radiation are modified due to event selection criteria, as previously described. The ZFITTER program incorporated all the necessary corrections to first order, and yielded values for $\sin^2 \theta_W^{\text{eff}}$, or, equivalently, A_e^0, using the accepted Standard Model values for correction parameters. Two of these parameters, the top quark mass (m_t) and the Higgs boson mass (m_H), are not well known. In practice, ZFITTER is run for a range of m_t and m_H values.

Chapter 2

Polarized Electron Production and Transport

The SLAC Linear Collider (SLC) was a significant achievement in e^+e^- accelerators. The SLC was completed in 1987 and began colliding electrons and positrons in 1989 to produce Z bosons for the Mark II detector, which was replaced by the SLD in 1991. Unlike e^+e^- storage rings which store and collide counter-rotating beams of electrons and positrons, the SLC created, accelerated, collided, and discarded electrons and positrons at a rate of 120 Hz. This single-pass design had a drawback in that the SLC luminosity was not competitive with storage ring luminosities. However, starting in 1992, the SLC created, transported and collided longitudinally polarized electrons, thus allowing precision measurements such as A_{LR}.

This chapter describes the creation and transport of the electron and positron beams. The Polarized Electron Source and the SLC are discussed in some detail, and special consideration is paid to subtleties involved in polarized electron transport. The description is valid for the 1993 run of the SLC.

The decays of Z bosons created by the SLC were detected by the SLD. The electron beam polarization was determined precisely by a Compton scattering polarimeter, downstream of the SLD. The SLD and the Compton Polarimeter are discussed in greater detail in the next chapter.

2.1 The Polarized Electron Source

The Polarized Electron Source (PES) consisted of a photoemissive cathode, pumped by light from lasers of energy close to the semiconductor band-gap energy. We first discuss the physics of a photoemissive cathode capable of producing spin-polarized electrons.

2.1.1 The photocathode

The cathode used in the 1993 run was a strained-lattice GaAs photocathode. Until recently, most photo-emissive cathodes were limited to 50% electron polarization. The strained lattice photocathode, which delivered electrons of polarization greater than 60% to the SLC IP.

The energy level diagram for a conventional GaAs photocathode and a strained lattice GaAs photocathode are shown in Fig. 2-1. In order to extract electrons from either type of cathode, laser light was passed through a right- (left-) handed helicity filter, and supplied incident photons of spin +1 (-1) which excited electron transitions indicated by the solid (dashed) arrows, from the top of the valence band to the bottom of the conduction band. Two degenerate transitions compete in a conventional photocathode. The Clebsch-Gordan coefficient for the unwanted transition is in a 1:3 ratio with that of the desired one, limiting a conventional cathode to 50% maximum polarization. Such a cathode was used in the 1992 run of the SLC/SLD and produced $\approx 22\%$ electron polarization at the SLC IP.

In strained-lattice cathodes, a mechanical strain is created in the photocathode crystal lattice, breaking the degeneracy of pumped states. The second figure in Fig. 2-1 shows such a strained-lattice photocathode. The degeneracy in the $P_{\frac{3}{2}}$ states is broken. A laser tuned to the right wavelength can pump the transition from the $P_{\frac{3}{2}}, m_j = \pm\frac{3}{2}$ state exclusively, populating only the $S_{\frac{1}{2}}, m_j = \pm\frac{1}{2}$ state, theoretically leading to electron polarizations of close to 100%.

The mechanical strain that breaks the degeneracy in the $P_{\frac{3}{2}}$ m_j states is created by depositing an epitaxial layer of GaAs over a substrate layer of GaAsP. The GaAsP substrate has a smaller lattice spacing, and the GaAs grown over it conforms to this smaller spacing, creating a strain which breaks the degeneracy. The energy difference in the m_j states is very small, $\Delta E_{strain} = 0.05$ eV. This small energy difference, coupled with the difficulties of depositing GaAs epitaxial layers evenly over the substrate, limits the extracted electron polarizations to be far less than 100%. In 1993, the electron beam polarization was 63.0 % at the SLC IP. Since then, polarizations of above 80% have been achieved.

Fig. 2-2 shows the polarization of the extracted electrons vs. wavelength of the laser illuminating

39

Lowest Conduction Band Energy Level
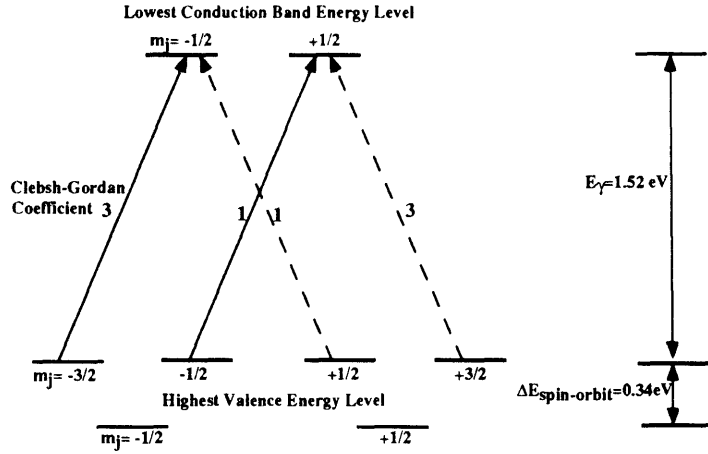
Conventional Gallium Arsenide
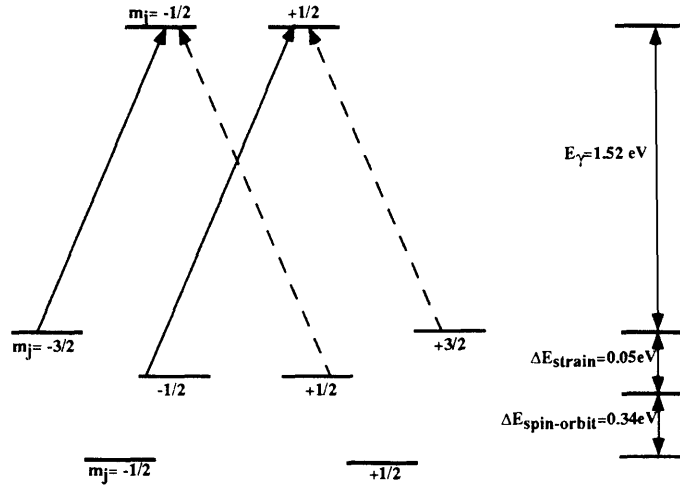
Strained-Lattice Gallium Arsenide

Figure 2-1: Energy levels for a GaAs photocathode (top), and a strained-lattice GaAs photocathode (bottom).

the photocathode. For the strained lattice GaAs cathodes, as the laser wavelength is increased, the $P_{\frac{3}{2}}, m_j = \frac{3}{2} \rightsquigarrow S_{\frac{1}{2}} m_j = \frac{1}{2}$ transition is excited exclusively, leading to $\approx 80\%$ polarization.

The electrons had to be extracted from the conduction band. Photoemission probability is quantified by the quantum efficiency (QE) of a material. QE is the probability that one photon incident on the photocathode surface will result in the emission of one electron. Since the energy gap between the conduction band of GaAs and the free-electron states is on the order of 2.5 eV, GaAs photocathodes have rather small QE. However, studies [19] have found that application of cesium to a photocathode serves to reduce the work function to zero and below. In such a photocathode, electrons excited into the conduction band can be easily extracted [20].

Cathode Polarization vs. Source Laser Wavelength
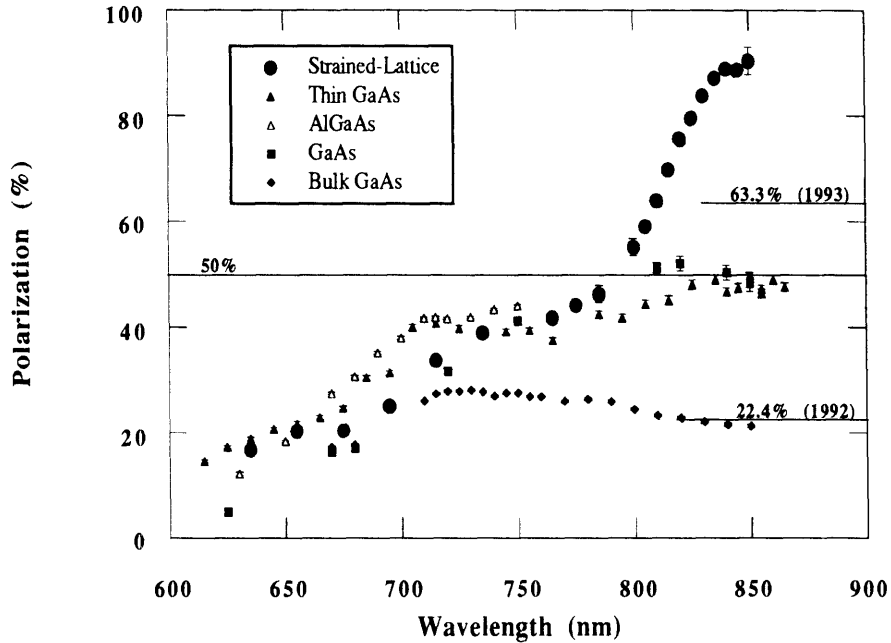
Figure 2-2:   Electron polarizations versus laser wavelength (nm) for different photocathodes.

2.2   The SLC Polarized Electron Gun

The cathodes described in the previous section are held in an assembly referred to as the polarized electron gun. A schematic diagram of the polarized gun used in for 1993 SLC operation is shown in Fig. 2-3. The entire gun was under vacuum, since it was coupled directly to the first accelerating section of the linear accelerator. The cathode was installed in a special assembly which allowed illumination of the cathode by the source laser, as well as application of the high voltage necessary to extract the electrons.

A voltage of -120 kV was applied to the cathode. The space-charge limit on the current drawn from a cathode with a given voltage depends on both the voltage applied and the geometry of the gun in which the cathode is installed. The space-charge limit for the gun was 8.9 amperes, or 1.1×10^{11} electrons in a 2 ns bunch. However, the factor limiting the charge extracted from the gun was not the space-charge limit, but another effect, labelled the *charge-limit effect*. The exact cause of this effect was unknown. The symptoms were as follows: The charge extracted from the gun increased as expected with laser power, but levelled off at $\approx 7 \times 10^{10}$ electrons. This limit was significantly lower than the space-charge limit for the gun, and was possibly due to effects at the cathode surface.

41
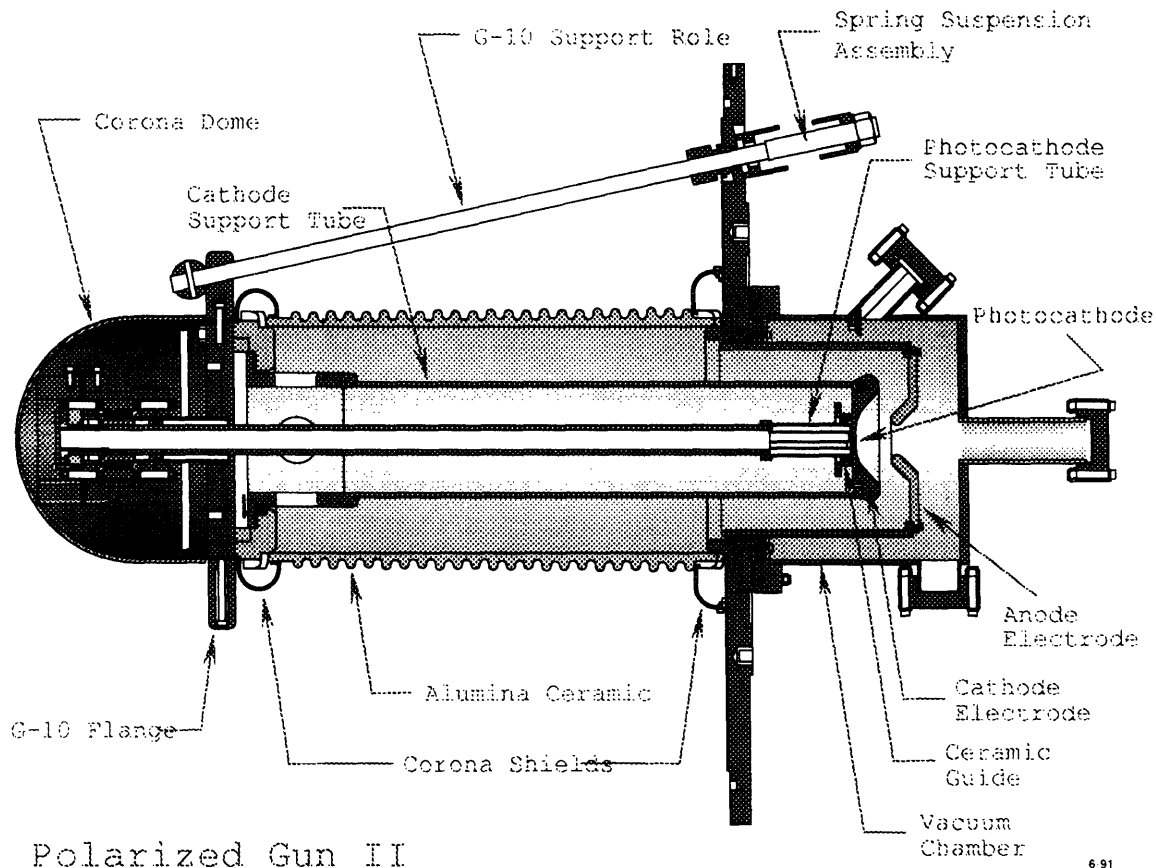
Figure 2-3: The Polarized Electron Source (PES), used in the 1993 SLC run.

2.2.1 The Source Laser

The cathode was illuminated by two Ti:Sapphire lasers. The Ti:Sapphire cavities output beams of 864[1] nm and 707 nm for the main electron pulse and the "scavenger" pulse, respectively. The scavenger pulse was transported to the positron source. A given scavenger pulse was used to create positrons to collide with the electrons from the next set of pulses.

Both Ti:Sapphire lasing cavities were pumped by two Nd:YAG lasers operating at 60 Hz. interleaved, to output electrons at the 120 Hz. required of the SLC. The light went through a Pockels cell — an electro-optic crystal described in more detail in chapter 5 — which transformed the linearly polarized light into right or left-circularly polarized light depending on the sign of a high-voltage driving pulse. The light helicity was chosen by a shift-register random-number generation algorithm [21], giving each light pulse a randomly chosen handedness. The light, incident upon the cathode, liberated electrons of the same helicity. Thus the helicity of each electron pulse was chosen

---

[1] At the start of the 1993 run, the laser ran at a wavelength of 790 nm for the main pulse. The wavelength was later optimized to 864 nm

pseudo-randomly, so that the helicity of the beam could not become accidentally synchronized with any possible periodicity in the SLC machine.

The "scavenger" pulse used to create positrons was created by a laser pulse of wavelength 707 nm. Since the Pockels Cell and related optics were chosen for light of 864 nm, the polarization was low for the photons used to create the scavenger pulse, leading to low scavenger electron polarization. Even if the scavenger pulse contained electrons of finite polarization, and even if this polarization were somehow transferred to the created positrons, and even if, through a series of coincidences, this polarization survived through the positron transport system and the positrons arrived at the SLC IP with finite polarization, their polarization state would be completely uncorrelated with the polarization state of the electrons since the positrons were created by a scavenger bunch formed with the previous electron bunch. In other words, the electrons from i^{th} pulse collided with positrons created with the $(i - 1)^{th}$ pulse. Random helicity selection ensured that the ith and $(i - 1)^{th}$ polarization state were not correlated.

2.2.2 Polarization state information

The sign of the high voltage on the Source Pockels cell determined the helicity state of the source laser, and thereby the helicity state of the electrons. This information was transmitted to the various detectors (SLD, Compton) via three redundant systems: the KVM (Klystron Veto Module), the MACH line (Machine Highway, direct signal wires from the source to the SLD), and the PMON (Polarization Monitor) system. The helicity transmission system was tested thoroughly: by comparing the redundant information on the three lines; by checking the helicity pattern against the predicted pattern from a simulation of the (deterministic) pseudo-random number generator [22]; and by dedicated machine tests where one helicity of light was extinguished (and did not produce electrons), so that electrons of only the other helicity were accelerated in the SLC. The SLD was triggered on these electrons, and absence of "wrong" helicity triggers used to put a limit on possible helicity transmission errors. All tests of the helicity-transmission system confirmed perfect transmission.

2.2.3 Cesiation

The quantum efficiency (QE) of the cathode in the gun dropped over time. The QE was improved by *cesiation*, a process in which cesium was deposited on the cathode to lower its work function. During the 1993 run, the cathode was cesiated approximately once every two weeks, whenever the QE dropped low enough to hamper proper SLC operations. A small inverse correlation of polarization with QE was observed [23]. This correlation manifested itself as an increase in polarization as a

43
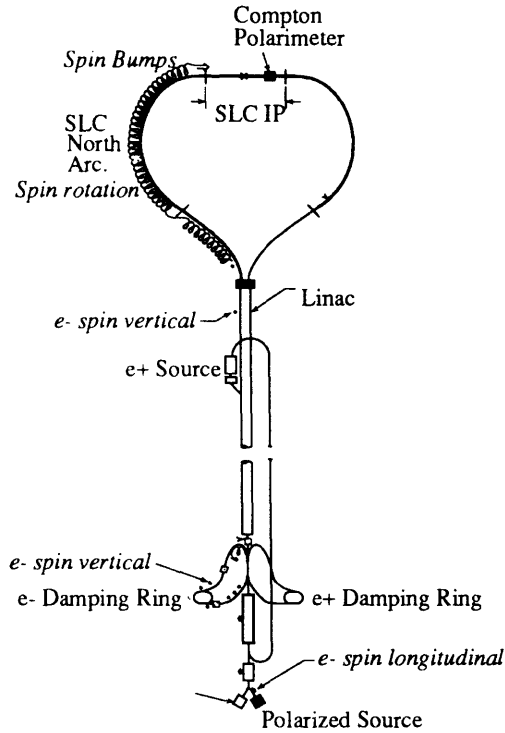
Figure 2-4: The polarized Stanford Linear Collider.

function of the time from the last cesiation. As the time from the last cesiation grew, the QE dropped, and the beam polarization increased. The detailed mechanism for this dependence of polarization on QE is still unknown.

2.3 The SLAC Linear Collider

Fig. 2-4 shows a schematic diagram of the SLC. The polarized source is indicated at the bottom, and the Damping Rings, located at the beginning of the accelerating sections of the Linac, are indicated separately as the electron Damping Ring (North) and positron Damping Ring (South). The Damping Rings were used to cool the electron and positron beams. In this context, cooling refers to reduction of the beam energy spread through synchrotron radiation damping. The positron source is also indicated, approximately three-fourths of the way along the Linac. Scavenger electrons incident upon a target created gammas, which in turn produced e^+e^- pairs. The positrons were collected and returned to the beginning of the Linac and cooled in the South Damping Ring.

2.3.1 The North Damping Ring

The North Damping Ring (NDR), used to cool electrons, contained a few elements not present in the South Damping Ring (SDR), which preserved the polarized nature of the electron spin. The electron beam could not pass through the NDR longitudinally polarized, as the energy dependent horizontal spin precession about the vertical axis due to the bending fields would have effectively randomized the spins. Therefore, a solenoid in the Linac-to-Ring (LTR) transfer line rotated the spins into a vertical orientation. The beam was then cooled in the ring in the normal manner, without losing polarization.

The detailed dynamics of spin rotation at the injection from the Linac to the Damping Ring (LTR) are illustrated in Fig. 2-5. The LTR consists of bends, which precess the spin. This precession is described fully by the BMT equation [24]. For planar motion through transverse bending fields, this yields

$$\frac{d\theta_{spin}}{d\theta_{bend}} = \gamma \frac{g-2}{2}, \tag{2.1}$$

where θ_{spin} is the angle of precession of the component of spin perpendicular to the guide field during an orbital turn of net angle θ_{bend}. The anomalous part of the magnetic moment of the electron, $(g-2)/2 = 1.163 \times 10^{-3}$, prevents the spin vector from following the momentum vector exactly.

The bend angle of the LTR was chosen such that the spin vector was perpendicular to the momentum vector in the horizontal plane. The spin vector was then rotated to vertical using a *spin-rotator* solenoid. A solenoidal field precesses a transverse spin component by

$$\theta_{spin} = \frac{eL\left(\vec{B} \times \dot{s}\right)}{m_e c\gamma}, \tag{2.2}$$

where L is the length of the solenoid and B is the field strength and s is the spin unit-vector. The electron direction of motion is the $\dot{z}$ axis, and the vertical is the y axis. The electrons left the cathode with longitudinal polarization, the spin vectors pointed in the z direction (arrow labelled 1 in Fig. 2-5). The LTR bend magnets precessed the spin to the x axis (arrow labelled 2 in the figure). The LTR solenoid then precessed the spin into the $\hat{y}$ axis (arrow labelled 3). The electrons were then injected into the Damping Ring and cooled (arrow labelled 4). The design of the Damping Rings and the various bends called for electrons of energy 1.21 GeV, while the electrons had an energy of 1.19 GeV at the Damping Ring during the 1993 run. This led to an 0.8% loss of polarization at the Damping Ring.

Upon extraction from the Ring, the electrons traversed the Ring-to-Linac transfer line. The bends here were not as important since the spin orientation was vertical. However, the RTL transfer

Solenoid

B

$\int \bar{B} dl = 6.34 \, Tm$

B ⊙

θ_s P

θ_P

$\theta_s = \gamma \frac{g-2}{2} \theta_P$

$90° = 2.74 \times 32.8°$

e^-

North Damping Ring (e^-)

RTL Solenoid

5

On

Off

3

LTR Solenoid

B

$5 \times 32.8°$

2

Linac Solenoid

$3 \times 32.8°$

e^- Linac

B

e^+ from South Ring

e^+

6 7

1

RTL Solenoid On

Linac Solenoid On

RTL Solenoid Off

Linac Solenoid Off
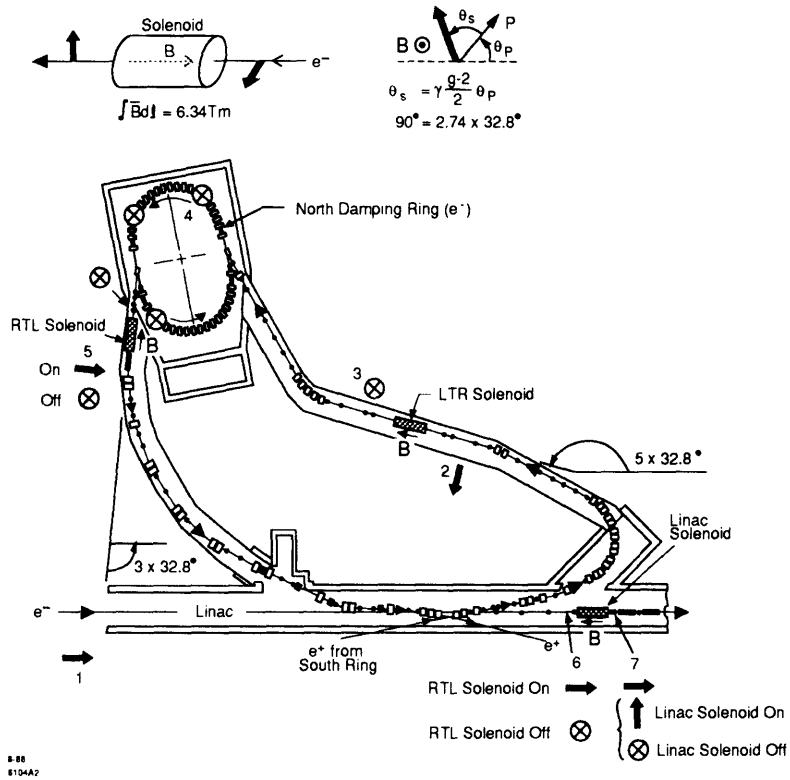
Figure 2-5:   The North Damping Ring. The orientation of the electron spin vector is indicated throughout.

line contained a second solenoid (the RTL solenoid) that could also orient the spin vector (arrows labelled 5 show the spin orientations with this solenoid fully energized and off). A third solenoid in the Linac (Linac solenoid), located just after the injection point from the Damping Ring could also be used to orient spins (arrows labelled 6 and 7 show the different spin orientations possible with the combination of RTL and Linac solenoids fully energized and off). The RTL and Linac solenoids were used to achieve longitudinal polarization at the SLD IP during the 1992 run. In 1993, they were only used for special tests, for normal running both the RTL and Linac solenoids remained turned off.

2.3.2 Flat Beams

After exiting the Damping Rings the beams had a flat profile ($\epsilon_x/\epsilon_y \approx 9$). They were injected into the Linac and accelerated to 46 GeV. The spin vector was still oriented in the vertical direction. The RTL and Linac solenoids were turned off, since their use would have rotated the flat beam profile.

The flat beam profiles allowed small spot sizes at the SLC IP, of $\sigma_x = 0.8\mu m$ and $\sigma_y = 2.6\mu m$, leading to a significant increase in luminosity over the 1992 SLC run, which used round beam profiles.

However, without the RTL and Linac solenoids to rotate the spin vector into an arbitrary direction and compensate for the arbitrary rotation of the North Arc, SLC was forced to make use of the spin rotation properties of the North Arc to orient the spin vector properly at the IP.

2.3.3 Spin Bumps

The use of flat beams in 1993 precluded the use of the RTL and Linac solenoids to orient the spin vector at the IP. However, introduction of large amplitude betatron oscillations in the North Arc (so called *spin bumps*) was found to be an effective way of orienting the spin vector at the IP.

During the 1992 run, the magnitude of the polarization was found to be very sensitive to the vertical orbit in the arc. The reason for this sensitivity was an accidental match of the betatron and spin tunes of the North Arc.

The SLC North Arc was comprised of 23 achromats, each of which consisted of 20 combined function magnets. The spin precession in each achromat was $1085°$, while the betatron phase advance was $1080°$. The North Arc was therefore operating near a spin-tune resonance. The result of this resonance was that vertical betatron oscillations in an achromat (which move the beam along the vertical axis) caused the beam spin vector to rotate away from the vertical. This rotation was a cumulative effect in successive achromats, due to the spin-resonance. Fig. 2-6 shows the close matching between the vertical oscillation in the North Arc and the longitudinal component of the spin vector. Properly placed vertical oscillations of the right amplitude could thus be used to orient the spin vector.

A pair of large amplitude vertical betatron oscillations were introduced in the North Arc (spin bumps). The amplitudes of these oscillation were adjusted empirically, to maximize longitudinal polarization at the IP [25].

The concern that the spin bumps did not orient the spin in the longitudinal direction perfectly was satisfied by special narrow energy spread round-profile beam tests. These tests, called *three-state measurements*, used the RTL and Linac spin-rotator solenoids to orient to spin vertically at the SLC IP. The RTL and Linac spin-rotators, located at the beginning and end points of the Damping Ring extraction line, which can orient the spin vector arbitrarily, compensate for any arbitrary spin transport element downstream. Therefore, the three-state measurements — so called because three separate measurements were made with the spin vector launched into the Linac with three orthogonal spin-orientations — determined the maximum polarization achievable. The three state measurements and the spin bump tests showed no discrepancy in maximum polarization measured with the Compton Polarimeter.
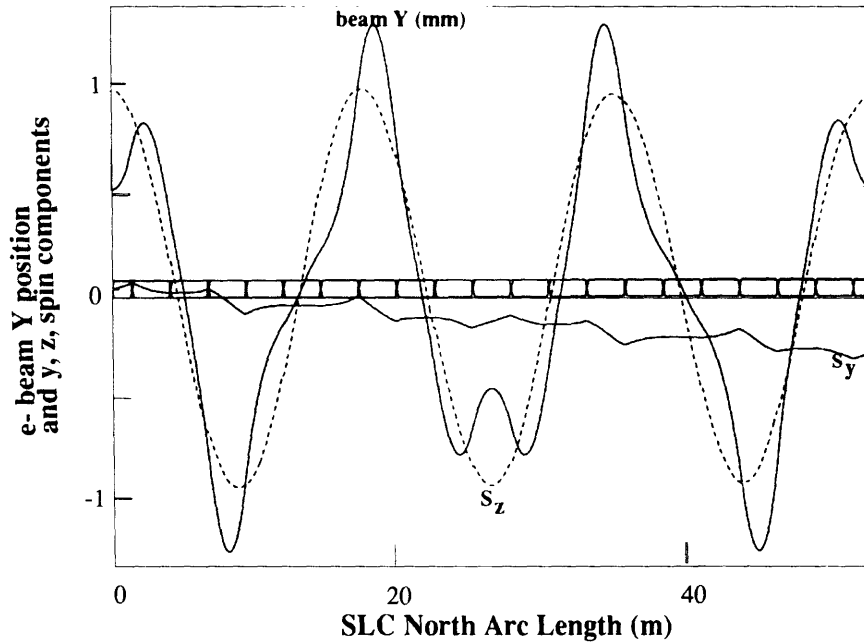
Figure 2-6: The vertical position of the beam in the North Arc (mm) and the vertical (S_Y) and longitudinal (S_Z) spin component of the electrons.

2.3.4 Dependence of polarization of beam energy

The large spin tune of the North Arc meant that the beam polarization depended very heavily on the beam energy. A perfectly polarized beam with a spread in energy would therefore lose polarization since the spin vector of the electrons in the core of the energy distribution would not precess the same number of times as the spin vectors of the electrons in the tail of the energy distribution. This effect has been termed *spin diffusion*, and is not equivalent to *depolarization*, which implies randomization of the spin vectors. Spin diffusion is due to the different rotations suffered by electrons of different energy. If, somehow, the beam were made to go back through the same fields, the electron spin and momentum vectors would perform inverse rotations and full polarization would be restored.

The North Arc achieved this restoration of polarization, albeit partially. The first section of the North Arc consisted of dipole fields that rotated the momentum vector approximately 90° (the reverse-bend). The second section of the North Arc bent the momentum vector by $\approx -90°$, thus recovering much of the polarization. A small amount of polarization loss occurred in the third section of the North Arc. Detailed prediction of the spin precession in the North Arc was not possible. Fortunately, the dependence of the polarization on energy was measured, using a test beam with narrow energy spread ($\Delta E/E < 0.1\%$), and low currents ($\approx 1 \times 10^{10} e^-$/pulse) – essentially a δ-function in energy. A dedicated test of the North Arc spin transport was performed with this narrow-energy spread test beam [26]. The beam polarization was measured using the Compton

48

	Value	Error
P$_{max}$	0.644	0.007
Spin turns	17.86	0.41
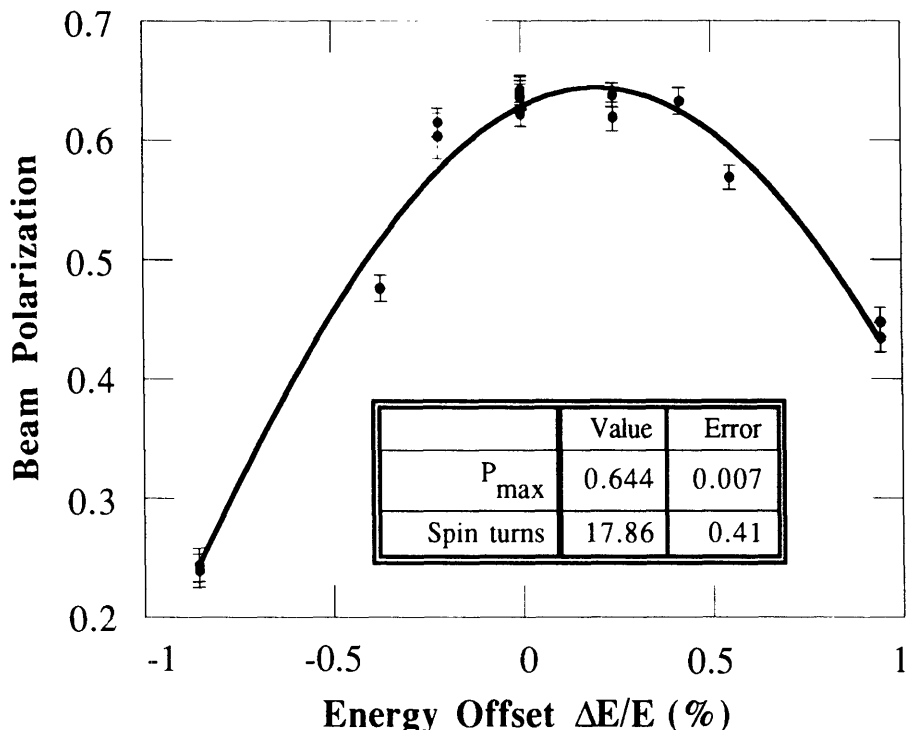
Figure 2-7: The results of the narrow energy spread beam tests. The cosine fit (line) yields 17.9 effective spin rotations in the North Arc.

Polarimeter. The data is shown in Fig. 2-7, along with a fit to the equation

$$\mathcal{P}_i = \mathcal{P}_e^{linac} \cdot \cos\left(2\pi N \cdot \frac{\Delta E}{E}\right), \tag{2.3}$$

where $\mathcal{P}_e^{linac}$ is the beam polarization at the Linac, presumably the maximum achievable. $\mathcal{P}_i$ is the polarization measured with the test beam at an energy E_i. N is the *effective* number of spin rotations, for electrons at the nominal energy. The peak of the curve is shifted ≈ 90 MeV from nominal ($\Delta E/E = 0.2\%$).

The narrow test beam experiments gave $N = 17.9$. This number is slightly smaller than 26, the number expected from a simple, planar model of the North Arc. More sophisticated models, incorporating the non-planar geometry of the North Arc, indicate that the spin vector had a significant vertical component that did not precess, until the spin bumps in the final section rotated it into the longitudinal direction. Therefore, the polarization loss in the North Arc was less than anticipated. The loss for a beam of energy spread $\Delta E/E = 0.15\%$, considered to be a conservative minimum for the nominal beam spread in 1993, was $\Delta\mathcal{P}/\mathcal{P} \approx 1.4\%$. The dependence of beam polarization upon energy, coupled with the strong focusing used at the SLC Final Focus in 1993 and a low-energy

tail in the beam, manifested itself as a chromatic correction that had to be applied to the beam polarization measurement. This correction is discussed in detail in chapter 7.

Chapter 3

Experimental Apparatus

This chapter introduces the SLC Large Detector (SLD) and the Compton Polarimeter, the two main pieces of equipment used in the A_{LR} analysis. The previous chapter described the creation and transport of positrons and polarized electrons. This chapter will concentrate on the equipment used to analyze the e^+e^- collisions, and measure the polarization of the e^-.

3.1   The SLD Detector

The SLD detector, was situated at the e^+e^- collision point of the SLC. The SLD, proposed in 1984 [27] was designed to be the main detector for Z physics at the the SLC IP. The SLD was a typical collider detector with nearly complete solid angle coverage. The geometry of the SLD is evident in the cutaway perspective drawing shown in Fig. 3-1. SLD was approximately a cylinder of length 10 meters, and radius 4.5 meters. The e^+e^- beams entered along the central axis of the cylinder, and the various detector subsystems were arrayed radially along this cylinder, known as the *barrel*. The cylinder was closed off at the faces by *endcaps*, which also contained part of the support structure for the beampipe.

The various subsystems of the SLD detector are shown in the quadrant-display of Fig. 3-2. The division between barrel and endcap systems is evident. The data from the SLD subsystems was read out almost entirely through the FASTBUS data acquisition protocol. Certain slowly monitored quantities were read out using the CAMAC protocol.

SLD

Warm Iron Calorimeter (WIC)

Liquid Argon Calorimeter (LAC)

e⁻

e⁺

Drift Chambers
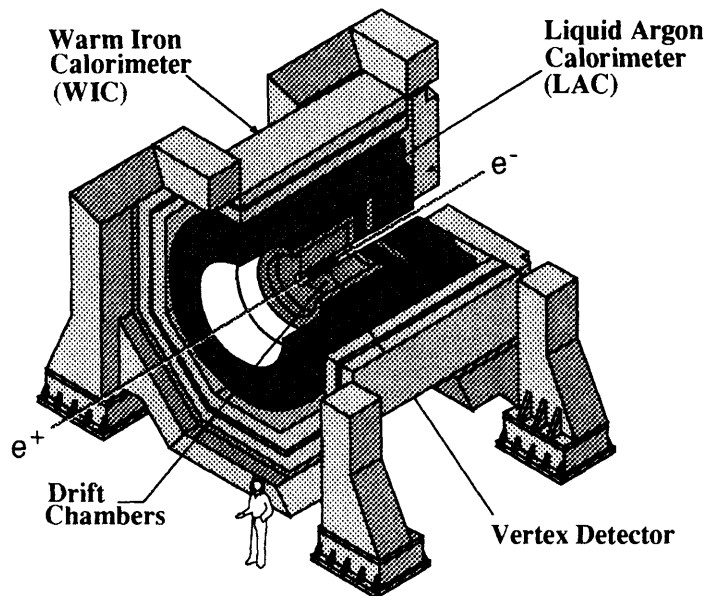
Vertex Detector

5731A2

Figure 3-1: A perspective, cutaway diagram of the SLD detector at the SLC.

3.1.1 Vertex Detector

Closest to the SLC IP was a vertex detector [28], designed to distinguish vertices from secondary decays of heavy quarks and τ leptons. The vertex detector was a multi-pixel device, composed of 480 silicon charged-coupled devices (CCDs) with a total of 120 million pixels. Each $22\mu m \times 22\mu m$ pixel provided an independent measurement of track position close to the IP. The CCDs were laid out in rows of eight along 60 "ladders", which were arranged in four concentric cylinders along the beampipe, at radii of 29.5 mm to 41.5 mm.

3.1.2 Luminosity Monitor

The SLD Luminosity monitors were also situated close to the beampipe, about 1 m along the beam axis from the SLC IP. The measurement of luminosity was made by measuring the small angle Bhabha event rate in a calorimeter called the luminosity monitor/small angle tagger (LMSAT) [29]. The LMSAT was a segmented silicon calorimeter with a tungsten radiator, and covered the region from 23 mr to 68 mr in polar angle. The LMSAT consisted of two complementary sections opposite the SLC IP. Each section had 23 tungsten plates each 3.5 mm thick, spaced 4.5 mm apart for a
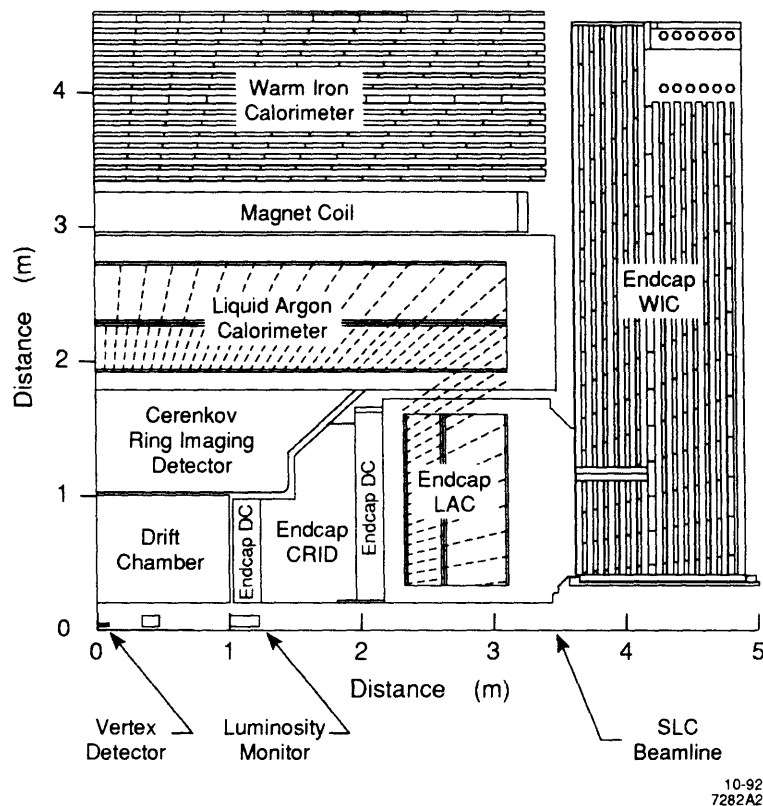
Figure 3-2: A quadrant view of the SLD detector, and associated subsystems.

total of 21 radiation lengths (which will contain $> 99.5\%$ of a 45 GeV electromagnetic shower). The active element was provided by interleaved silicon detectors segmented transversally into $\sim 1\text{cm}^2$ cells. Projective towers were formed by connecting the appropriate cells in two separate radial sections consisting of the first six and remaining 17 layers respectively.

3.1.3 The Drift chambers

The vertex detector was surrounded by a drift chamber [30]. The central drift chamber (CDC) was 2 m long and had an inner radius of 20 cm and an outer radius of 1 m. It was composed of ~ 50 mm-wide cells forming ten concentric superlayers. Each cell consisted of field-shaping wires, guard wires and eight anode sense wires. The detector was filled with $CO_2 - Ar$ gas with H_2O to reduce carbon deposition on the sense wires and isobutane to increase gain. The high-voltage on the field wires was chosen appropriately to operate the detector in the proportional streamer mode. Electron drift distances in the chamber were known to $\sim 100\mu$m, defining the transverse position resolution. The sense wires were read out on both ends, and charge division yielded the longitudinal hit position, to ~ 15 mm.

53
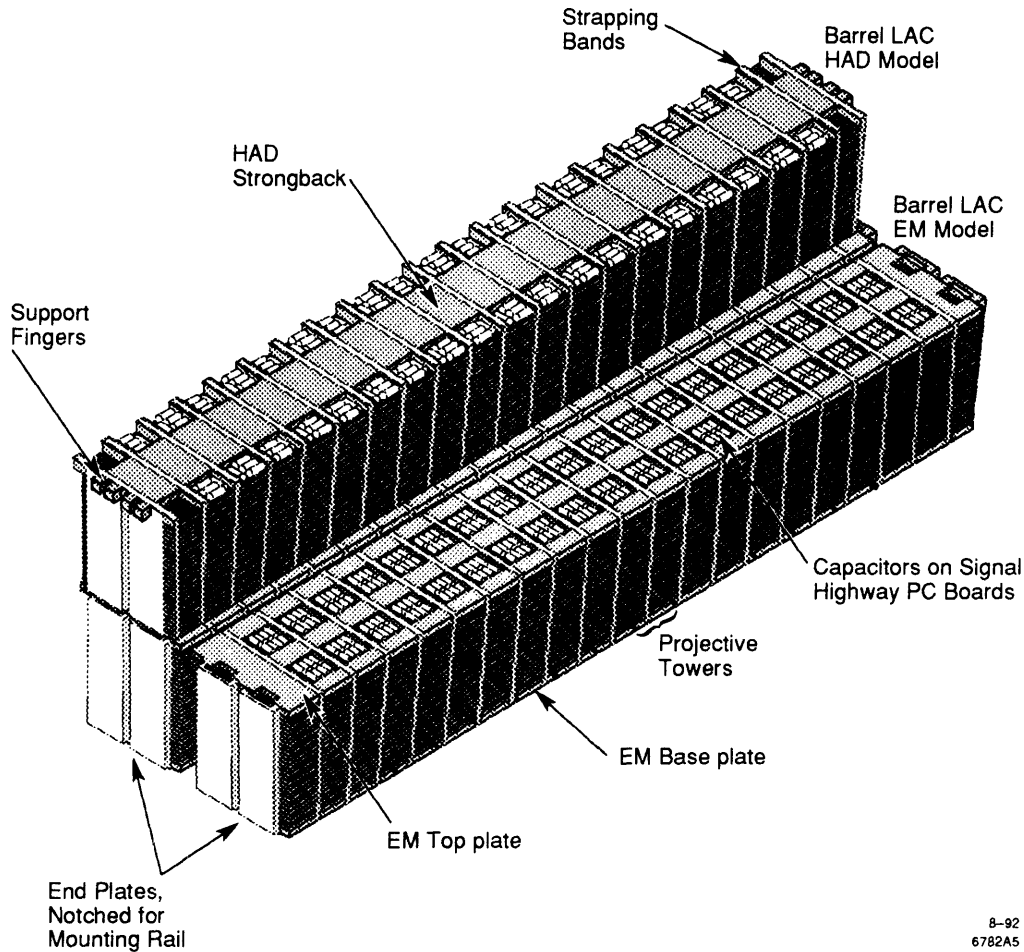
Figure 3-3:   Schematic diagram of a LAC module. The inner EM sections and the outer HAD sections are shown.

Tracks with polar angle less than 30° were not well measured in the CDC, as these tracks passed through only a small number of layers. The endcap drift chambers (EDCs) covered the region between 12° and 40° in polar angle. The two pairs of EDCs were mounted at 1.12 m and 2.06 m along the beam axis from the IP. Each EDC was composed of three superlayers rotated 120° with respect to each other. The inner and outer chamber superlayers respectively comprised of 22 and 34 cells each, with six sense wires in each cell.

3.1.4   The Liquid Argon Calorimeter

Calorimetry at SLD was performed mainly by the Liquid Argon Calorimeter (LAC). The LAC was composed of lead plates which induced showers for incident electromagnetic and hadronic particles, separated by liquid argon. The LAC absorbed all the electromagnetic energy incident upon it from Z decays at the IP, and most of the hadronic energy.

A schematic drawing of a LAC module is shown in Fig. 3-3. The LAC was a sampling calorimeter consisting of a barrel section and two endcap sections. The barrel LAC was six meters in length with an inner radius of 1.8 m and an outer radius of 2.9 m. It provided calorimetric coverage for polar angles $\theta < 33°$. The endcap sections fit inside the barrel LAC, and provided polar angle coverage in the region $8° < \theta < 35°$. The barrel and endcap LAC together provided covered 98% of the polar angle. Since the barrel LAC was situated within the SLD solenoid, there was no loss of resolution due to incident particles traversing the coil. A common volume of 35,000 litres of liquid argon bathed the LAC, and cooling loops carrying 10,000 liters of liquid nitrogen per day stabilized the liquid argon temperature.

The LAC was composed of 320 modules (288 in the barrel and 16 each in the endcaps), each of which was made up of stacked parallel-plate liquid argon ionization chambers. The chambers consisted of stacked lead tiles alternating with lead plates, separated by spacers, with liquid argon flowing in between. The lead plates were grounded and each stack of tiles within a module was ganged together electrically across the plates and held at high voltage to form the charge collecting anode. Thus the absorber also served as the electrode, allowing compact calorimeter design.

The LAC was segmented radially, and each segment contained separate types of modules: Electromagnetic (EM) modules were mounted on the inside radial section, and hadronic (HAD) modules were mounted on the outside. In the EM calorimeter, the lead plates and tiles were 2 mm thick with a 2.75 mm spacing in between for the liquid argon, providing 0.79 X_0/cm with a dE/dX sampling fraction of 18% to normally incident particles. The EM calorimeter was further divided into two radial sections, EM1, of six radiation lengths, and EM2, of fifteen radiation lengths. The total EM thickness contained 50 Gev electrons with only 1-2% energy leakage. The EM energy resolution was $\sim 15\%/\sqrt{E}$. The HAD calorimeter was made up of 6 mm thick lead plates, separated by 2.75 cm of liquid argon, which yielded a density of 0.044λ/cm. The HAD calorimeter was also segmented further into two radial sections, the HAD1 and HAD2, each of which was 1 absorption length thick. The total EM+HAD thickness was 2.8 absorption lengths, which contained 80-90% of the total energy of a hadron shower. The HAD energy resolution was $\sim 65\%/\sqrt{E}$ [31].

The spatial resolution of the LAC was determined by the tile size. The inside of the barrel was divided azimuthally into 192 sections, each subtending 33 mr of azimuth, and was divided in polar angle into 68 sections of size from 21 mr to 36 mr. The tile size increased toward the endcaps in order to provide a constant projective area for electromagnetic showers. HAD segmentation was twice as large as the EM in both transverse dimensions. A single projective unit of EM or HAD tiles was called a *tower*. Each endcap was segmented azimuthally into 192 EM sections at large radii, 96 sections at intermediate radii, and 48 sections at the center, maintaining an approximately constant projective area for electromagnetic showers. The endcaps were segmented into 17 EM sections in

polar angle. The HAD segmentation was twice as large as the EM in the endcaps as well.

The LAC towers were connected to front end electronics, resident on the detector face, called *tophats*. Each tophat contained amplifiers and analog to digital converters (ADCs) that amplified ionization signal from the liquid argon and digitized it. The signal was then converted into a light signal and sent to a FASTBUS crate via an optical fiber.

The signal from the LAC was recorded as counts from the respective ADCs connected to the towers. An energy calibration converted this raw signal into an energy that could be assigned to an incident particle or set of particles. Calibration of sampling calorimeters is an art, since many factors, including details of the geometry and construction, play large roles. The SLD LAC calorimeter response has been well studied by González [31], and we refer to this calibration in the section on event selection.

3.1.5 The beam energy measurement

The beam energies in the SLC were measured by a wire imaging synchrotron radiation detector (WISRD) [32], present in each of the two SLC arcs, near the beam dumps for the electron and positron beams. A schematic drawing of the WISRD energy spectrometer is shown in Fig. 3-4. The beam three dipole magnets in a split-beam configuration. The first magnet induced a horizontal bend, which created a horizontal swath of synchrotron radiation that provided a reference pedestal for the bending downstream. The second magnet was a precisely calibrated analyzing dipole, and bent the beam vertically. A third horizontal bend magnet provided further calibration. The synchrotron photons were detected on multiwire screens. The mean center-of-mass energy for the 1993 run was 91.26 Gev.

3.2 The Compton Polarimeter

The Compton Polarimeter provided a precise measurement of the beam polarization by measuring the asymmetry in polarized Compton scattering [33]. It was situated in the Final Focus area of the South Arc of the SLC, approximately 30 meters from the SLC IP. It had two major components, a system to generate, transport and collide photons with the beam electrons, and a system to detect and analyze the Compton scattered electron flux from the electron-photon interaction.

Circularly polarized light from a laser of wavelength 532 nm was brought into collision with the electrons that had left the SLC IP at a point called the Compton IP. The distance between the SLC IP
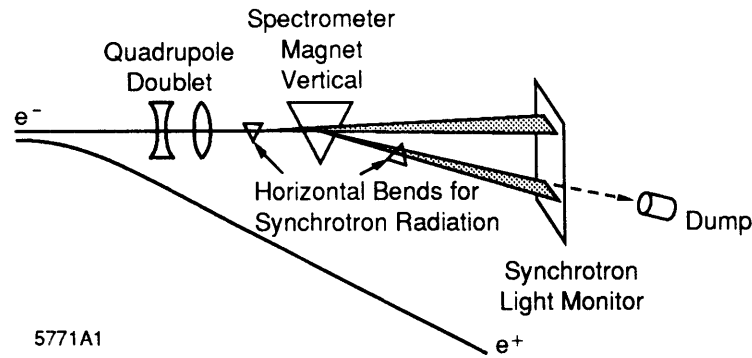
Figure 3-4: The Wire Imaging Synchrotron Radiation Detector (WISRD), used to determine the beam energies at the SLC.

and the Compton IP contained only quadrapole focussing magnets and no dipole bend magnets that would have precessed the spin. The electrons Compton scattered off the photons, after which they remained essentially collinear with the unscattered electron beam (within a 10 μr cone), since the electrons had an energy of $\approx$ 46 GeV and the photons had 2.33 eV. However, the scattered electrons had a spread in energy, depending on the center-of-momentum scattering angle of the electron-photon system. The lowest energy electrons had $E \approx$ 17 GeV, which corresponded to complete backscattering in the center-of-momentum frame. The Compton scattered electron were separated from the main (unscattered) beam after they passed through the analyzing bend field provided by two SLC South Arc dipole magnets, SB1 and B1 whose effective bend center was approximately 3.6 m upstream of the polarimeter detectors. There were two transversally segmented detectors that intercepted the fan of Compton scattered electrons as they were bent out by the analyzing field. The first was a nine-channel Čerenkov threshold counter (the Čerenkov detector). The second was 16 channel multiwire proportional tube detector (the PTD). The Čerenkov detector was the primary detector used for polarimetry.

The other major component of the Polarimeter was the laser, situated in a trailer (the "laser shack") on a hill above the SLC South Arc, and the laser helicity-control and transport system. The helicity control and transport of the light from the laser was achieved by a system consisting of various pieces of optics in the vicinity of the laser to control the polarization state of the light, a system of several mirrors, windows, and a lens to bring this light into the SLC beampipe and focus it for collision, and an *Analysis Box*, which served as a laser beam dump and light-polarization analyzer. Fig. 3-5 shows a schematic of the Compton Polarimeter system, in relation to the SLD

Compton Polarimeter
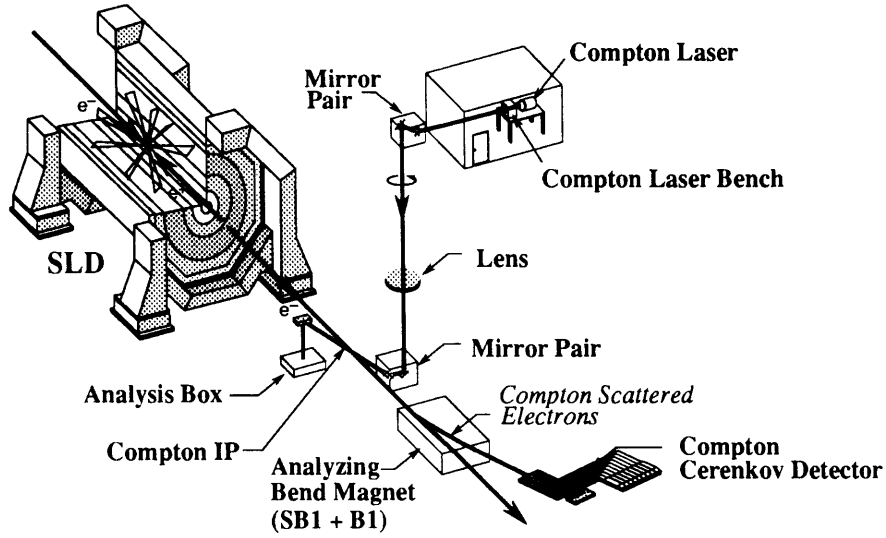
Figure 3-5:   Schematic of the Compton Polarimeter in the South Final Focus region of the SLC, showing the electron beam intercepted by the Compton laser after it leaves the SLD detector.

detector.

3.2.1   The Compton Čerenkov detector

A nine-channel Čerenkov threshold device served as the main detector for the Compton scattered electrons. The requirements made of the Compton Polarimeter electron detectors were good position and linearity calibration, and suppression of background. The positions of the relevant Černekov detector channels were determined to a precision of $\sim \pm 250\mu m$, (section 6.2). The backgrounds at the Compton detectors were caused mainly by radiation from beam-beam interaction at the SLC IP (*beamsstrahlung* radiation), which had energies of ~ 1 GeV, but degraded to a few MeV after scattering from accelerator elements. Another source of backgrounds was synchrotron radiation from the South Arc bend magnets, ~ 1 MeV. The Čerenkov threshold of the gas used in the detector was ≈ 10 MeV, effectively making the detector blind to this soft background. A schematic diagram of the Compton Čerenkov detector (and PTD) is shown in Fig. 3-6. The beampipe, shown at the top, ran North-South. The detectors were located east of the beampipe, where the analyzing bend field steered the fan of Compton scattered electrons. There were two remotely insertable lead plates, called *preradiators*, in front of the detector. The preradiator blocked soft electrons and photons from entering the detector through the front face, and amplified the signal due to Compton
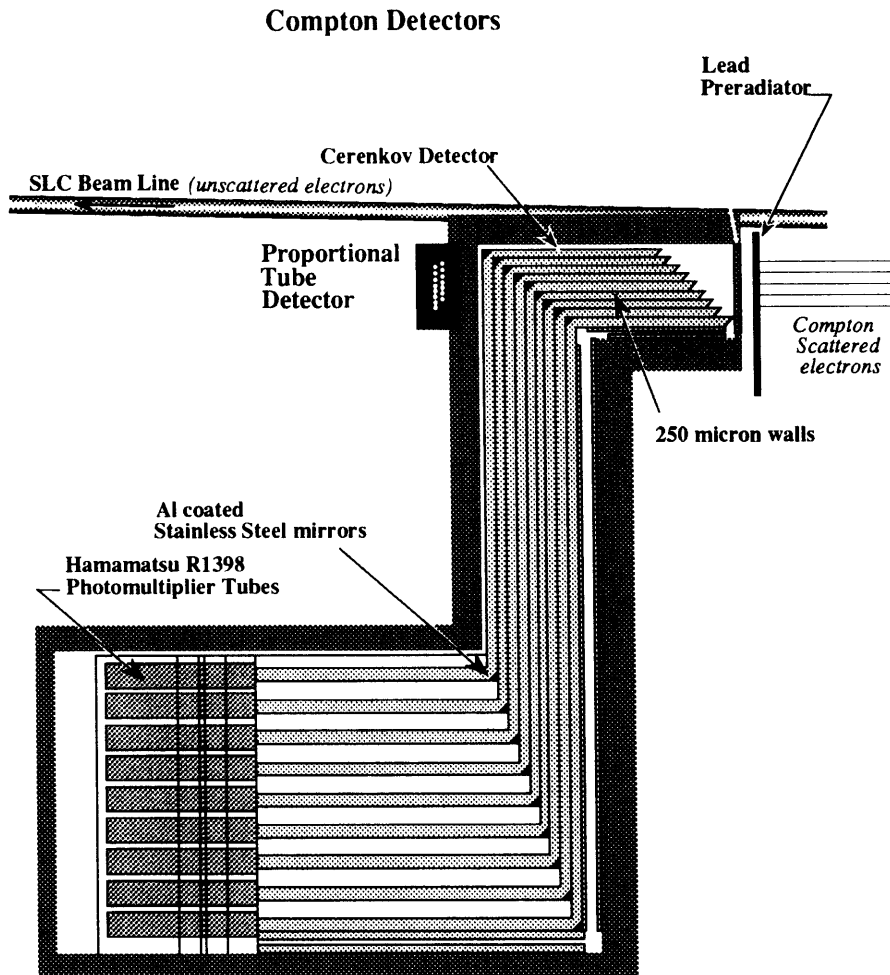
Compton Detectors

Figure 3-6:   A top-view illustration showing the Compton Čerenkov detector and PTD with respect to the SLC beamline. The encasing lead is not shown.

scattered electrons by causing the electrons to shower within the lead. The detector body consisted of nine channels, each 1 cm wide and 20 cm long, separated by 250 μm thick aluminum walls. All reflective surfaces throughout the detector were buffed along the channel axis and coated with 1000 Å pure aluminum. The detector channels were projective back to the bend point of the magnetic field. The channels had a 3 mr/channel angular offset to achieve this projective geometry. Čerenkov radiation created in the space between the detector body and the start of the channels was blocked by thin aluminum tabs at the beginning of the channels.

Čerenkov photons were emitted at 55 mr relative to the electrons in the front section of the detector. These photons were were reflected by the channel walls and by two sets of polished, aluminum-coated stainless steel mirrors set at 45° along the bend points of the channel into nine

Hamamatsu R1398 photomultiplier tubes. The bends in the light path allowed the photomultiplier tubes to be situated relatively far away from the beampipe and associated sources of noise. The entire detector was encased in several inches of lead for shielding, so that any direct path to a photomultiplier tube went through at least 4 inches of lead. The transmission efficiency of the 253.7 nm ultraviolet light through the detector was measured to be $\sim$ 50%. The interior of the detector was filled with cis- and trans-2 butene at atmospheric temperature and pressure, which yielded a 10 MeV cutoff energy for producing Čerenkov light. The entire detector, along with the lead shielding on top, was placed on a movable stage, called the detector table. This table could be moved transverse to the beampipe, and a precision linear potentiometer readback provided relative position information. In addition, microswitches provided confirmation when the detector was in its nominal position.

The photomultiplier tubes used for the Čerenkov detector were Hamamatsu R1398: $1\frac{1}{8}$" ten-stage design with a linear focused dynode chain for high instantaneous signal linearity. These tubes had a fused-silica glass window which admitted photons in the range from 200 to 600 nm. The Hamamatsu R1668 photomultiplier tubes were also used. The R1668 were identical to the R1398 except for a quartz window which admitted photons in the range from 160 to 650 nm The frequency cutoff for light propagating through the gas was 200 nm, and the two tubes were observed to have similar response. The width of the output pulses from each type of tube was $\sim$ 2 ns. The bases used with the tubes were of a special design, using two sources of high voltage, to ensure the tubes operated in the linear regime. The primary source of instantaneous non-linearity in a photomultiplier tube — space-charge saturation in the last stages of amplification — was controlled by keeping the voltage to the latter stages high, thereby maximizing the space-charge throughput (which is proportional to $V^{\frac{3}{2}}$), while lowering the voltage to the first few stages which decreased the current so as to stay within the space-charge throughput limit of the latter stages. Traditionally, tapered resistor chains in photomultiplier bases have provided progressively higher fields in the later stages. The bases used in for the Čerenkov detector improved on this concept by using two separate high-voltage sources to provide the fields for the initial and final stages. The cathode and the first six dynodes of the photomultiplier were controlled by the *front-end* voltage supply, while the final two dynodes were controlled by the *back-end* supply. The linearity of the photomultiplier tube response was measured as a function of the signal height by varying the front-end voltage, while keeping the back-end voltage constant, thus changing the gain while maintaining the saturation characteristics of the back-end. The results are discussed in section 6.1.

Figure 3-7: Compton Polarimeter Laser Bench layout for 1993.

3.2.2 The Compton laser system

The polarized photons used in the Compton Polarimeter were provided by a Spectra-Physics DCR-11 Nd:YAG (Neodymium Yittrium-Aluminum-Garnet) laser, frequency doubled to 532 nm wavelength. The laser was Q-switched to provide a $\sim 160kJ$, 8 ns pulse. The laser was triggered once every 11 SLC beam crossings. A 120 Hz. timing signal from the SLC, appropriately masked for 10 concurrent pulses, provided the triggers for the laser flashlamp and Q-switch. The goal of the laser and associated light transport was to deliver circularly polarized photons to the Compton IP. There were many optical elements in the path, including mirrors, windows and a lens, which caused the light to lose circular polarization. Two major effects of the light transport on the photons were unwanted phase shifts, and introduction of incoherent, unpolarized light. An upper limit was placed on the amount of unpolarized light. The phase shifts introduced by the transport system were monitored and corrected continuously during the run.

Fig. 3-7 shows the layout of the laser bench optics. The laser and bench were located in a trailer on the hill behind the CEH, situated almost directly above the South Final Focus region and the Compton IP. As the figure shows, two mirrors on the bench steered the laser through a beam expander into a phase-correction system consisting of a linearly polarizing Glan-laser prism and

61

X: 60mm

S: 18.2mm

W: 15.9mm

T: 5mm

L: 79mm

Cleveland Crystals Model TX3460
Pockels Cell

Figure 3-8: A schematic drawing of the Cleveland Crystals Model TX3460 Pockels cell.

two Pockels cells. The prism transmitted linearly polarized light, which could then be transformed into a state with arbitrary elliptical polarization by the Pockels cell. The two Pockels cells were labelled the CP and PS Pockels cell. Pockels cells are electro-optical devices capable of imparting an arbitrary phase to incident light. In normal polarimeter operation, the phases were chosen such that circularly polarized light was delivered to the Compton IP. The entire process is described in more detail in chapter 5.

The Pockels Cells

A Pockels cell is a voltage-dependent optical compensator. A compensator is an element that induces different phase shifts to polarization components along different axes. A preferred axis (the *fast axis*) has the smallest phase shift, while a perpendicular axis (the *slow axis*) has the largest. Fixed compensators are usually labelled by the difference in phase shift along the fast and slow axes, in units of incident light wavelength. A quarter-wave compensator induces a shift of $\frac{\lambda}{4}$, while a half-wave plate induces a shift of $\frac{\lambda}{2}$. A given Pockels cell has specific voltages where it acts as a quarter-wave and half-wave compensator, referred to as the quarter-wave and half-wave voltage for that cell. A quarter wave compensator aligned with its fast axis at $+45°$ ($-45°$) to the polarization axis of linearly polarized incident light transforms that light into right-handed (left-handed) circularly polarized light[1].

The Pockels cells used in the Compton laser system were Cleveland Crystal Optics model TX3460

---

[1] Right-handed light has positive helicity; left-handed light has negative helicity. This is the *particle physics* convention. The *optics* convention for the sign of circular polarization is exactly opposite.

M: Mirror
MP: Compensating Mirror Pair
GP: Glan Prism
CP: Circularly Polarizing
    Pockels Cell
PS: Compensating Phase Shift
    Pockels Cell
PP: Pickoff Plate
LTL: Laser Transport Line
L: Lens
PD: Photo-diode
W: Window
ND: Neutral Density Filter
CIP: Compton Interaction Point
P: Calcite Prism
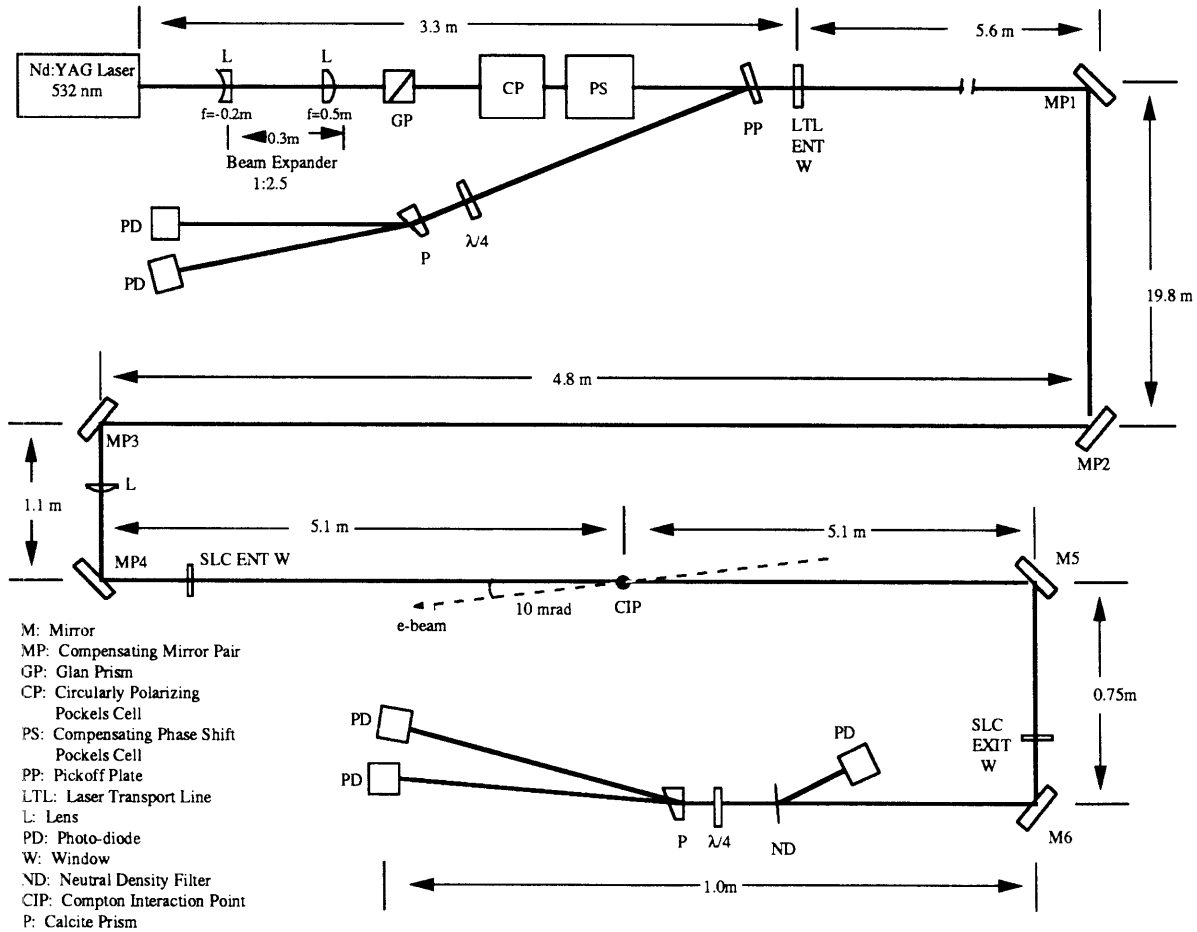
Figure 3-9: Compton Polarimeter Laser Transport System.

cells. A KD*P crystal was mounted, along with electrodes and high-voltage connections, in a metal housing approximately 8 cm long, which included the entrance and exit window mounts. The magnitude of the electric field applied along the crystal determined the phase-compensation properties. The polarization purity of these cells was measured to be better than 99.8%. The quarter-wave voltage for these cells was around 1600-1700 volts. The two Pockels cells were driven with a CAMAC module called PMON, built at SLAC. This unit provided two low voltage signals that were amplified a factor of 1000 by two high-voltage amplifiers. The PMON unit contained pseudo-random number generators [34], used to select between positive and negative voltages to apply to the Pockels cell for alternate pulses.

After the light left the laser bench, it was reflected by a set of compensated mirror pairs down into the SLC South final Focus area and into collision with the electrons exiting the SLD. Fig. 3-9 shows a diagram of the laser transport system. Individual mirrors may impart a phase shift, ϵ, to the reflected light. In general, ϵ may differ for S (senkrecht, or polarized perpendicular to the plane of reflection) and P (parallel, or polarized parallel to the plane of reflection) rays. If the incident ray

is an S ray, the first mirror imparts a phase shift ϵ_S upon reflection. The second mirror in the pair is oriented such that the ray is now incident as a P ray on the second mirror, suffering an additional phase shift ϵ_P. Therefore the total phase shift from both reflections is $\epsilon_S + \epsilon_P$. Similarly, if the ray is incident as a P ray on the first mirror, it will undergo a total phase shift of $\epsilon_P + \epsilon_S$ upon reflection from the mirror pair. Therefore, the phase shift *difference* between incident S and P rays is zero after reflection from the mirror pair. The mirrors used in the laser transport system were compensated pairs — both mirrors in a given pair coated in the same production run. Measurements of total phase shift imparted by such compensated pairs show it to be small.

After the Compton IP, two mirrors (single mirrors, not compensated pairs) directed the beam into the laser beam dump — the Analysis Box. Mirror 5, mounted within the beampipe, directed the laser through the vacuum exit window into the Analysis Box. Mirror 6 directed the light towards the analyzing optics. These two uncompensated mirrors introduced large phase shifts in the light after the Compton IP. The circular polarization measured in the Analysis Box was, therefore, different from that measured at the Compton IP.

Analysis Box

The Analysis Box, situated at the end of the laser light path, contained helicity filters to analyze the light polarization. Fig. 3-10 shows the layout of the Analysis Box, and associated optics. After reflection from Mirror 6, the light went through a helicity filter, composed of a quarter-wave plate and a calcite prism. Fig. 3-11 shows a schematic of how the calcite prism was used in the helicity filter. The calcite prism has a different index of refraction for light polarized perpendicular to a preferred axis (the ordinary ray), than for that polarized along this axis (the extra-ordinary ray). As Fig. 3-11 shows, the light is bent according to Snell's law as it leaves the prism, but the extra-ordinary ray is bent by 16.3°, while the ordinary ray is bent by 11.8°, creating a separation of $\approx 5°$, between the two states. Photodiodes were used to measure intensities of both rays coming from the calcite prism, thereby obtaining simultaneous measurements from both a right-handed and a left-handed helicity filter.

3.2.3 The Compton data acquisition system

The Compton polarimeter data acquisition was separate from the main SLD data acquisition system. The SLD read out several racks of FASTBUS modules based on a hardware trigger decision. The Compton data acquisition, by contrast, was composed of three real-time CAMAC crates, read out by a Micro-Vax at 120 Hz. The data from the various CAMAC modules were sent by Ethernet to the
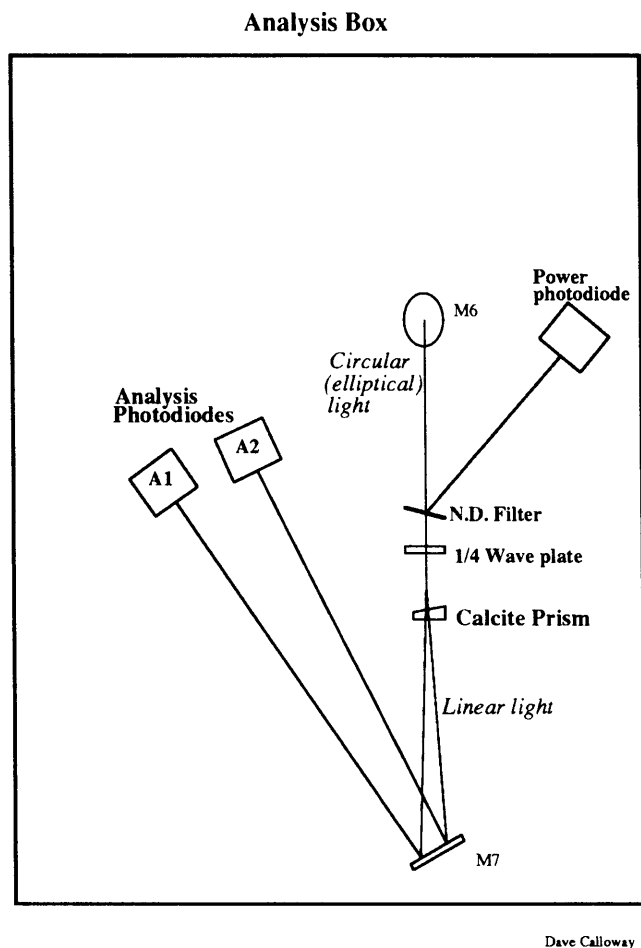
Analysis Box

Figure 3-10: Compton Polarimeter Analysis Box, which also serves as the light dump for the Compton Laser.

SLDACQ 8800 VAX. The SLDACQ then formed two streams of data. The "raw" stream consisted of every laser-on pulse and a corresponding laser-off pulse. The "summed" stream consisted of data summed in separate electron/photon helicity-indexed bins as appropriate.

The following data were logged to tape by the polarimeter data stream: the signals from each of the nine Čerenkov channels as well as the 16 PTD channels; the signals from the photodiodes on the laser bench and the Analysis Box; the voltages on the two Pockels cells; several SLC beam-current monitor toroids; and several monitored quantities indicating various Polarimeter status values such as detector table position, lens position, etc. In addition, information about the electron beam helicity from the polarized electron source and Compton laser helicity state was read from several bit-registers and logged.

The "summed" data stream contained information for $\approx 20,000$ SLC beam crossings. The
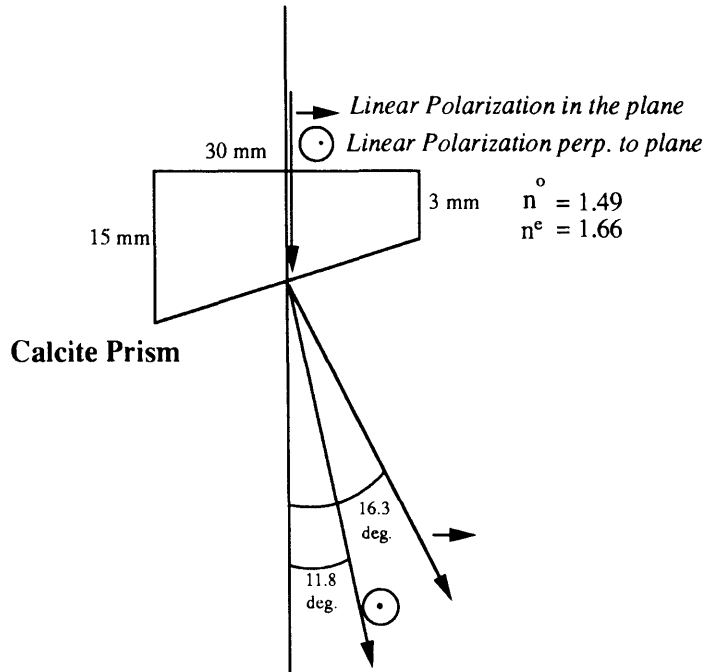
Figure 3-11: Schematic of calcite prism operation in the helicity filters.

data from the detectors was binned separately for the two electron-helicity states (right- and left-handed) as well as the three laser states (right- and left-handed, and laser-off), for a total of six bins. The laser-off data provided the background subtraction for the data. Since the laser was fired only once every 11 beam crossings, the statistical uncertainty on the background measurement was significantly smaller than that on the signal. The "raw" data stream contained data in packets of 150 beam crossings. Every Compton laser-on pulse, with a subsequent Compton laser-off pulse coinciding with a pulse from same Polarized Source laser as the laser-on pulse, was written. We used the "summed" data stream to determine the polarization of the electron beam. The "raw" data were examined for effects which could have biased the "summed" data, such as large, instantaneous fluctuations in the backgrounds (spiky noise). No such fluctuations were found.

Chapter 4

Compton Polarimetry and the Beam Polarization Determination

Electron beam polarization uncertainties contribute the single largest systematic error in the measurement of A_{LR}. The beam polarization measurement is therefore of great interest, since the care and precision exercised effect A_{LR} directly. For the 1993 SLD run, we determined the beam polarization, $\mathcal{P}_e$ with a systematic error of $\frac{\delta\mathcal{P}_e}{\mathcal{P}_e} = 1.3\%$.

Compton scattering of polarized electrons from polarized photons exhibits a large, spin-dependent asymmetry that can be used to determine beam polarization. At the SLC, the Compton scattered electrons were detected after they had passed through a dipole analyzing magnet. This technique offered the advantages of a large measured asymmetry and a spatially separated kinematic spectrum.

4.1   Compton scattering kinematics

Compton scattering can proceed through two channels, the s and t. The Feynman diagrams for these channels are shown in Fig. 4-1. The Compton cross-section can be derived in the electron rest frame; however, care must be taken to include the effects of the electron rest-mass, since the total energy of the electron and photon is less than 1 MeV. The expression for the Compton differential cross section in the electron rest frame is

$$\left(\frac{d\sigma}{d\Omega}\right) = \frac{1}{2}r_0^2\left(\frac{k'}{k}\right)\left[\frac{(k-k')^2}{kk'} + 1 + \cos^2\theta_0\right]\left\{1 - \mathcal{P}_\gamma\mathcal{P}_e A^{e\gamma}(\vec{k}\vec{k'})\right\}, \tag{4.1}$$
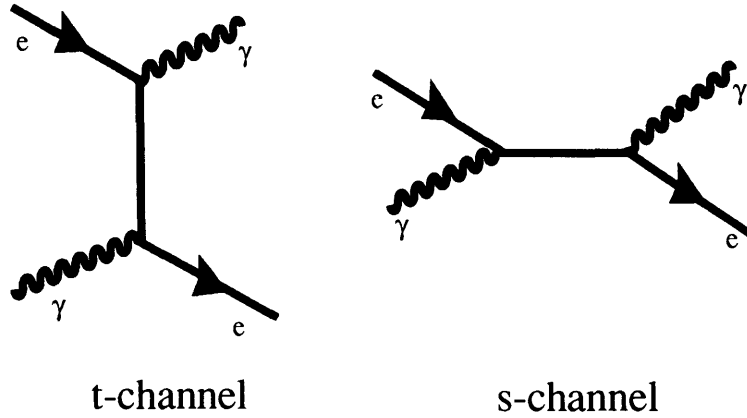
Figure 4-1: Feynman diagrams for Compton scattering.

where $r_0 = 2.82 \times 10^{-13}$ cm is the classical electron radius, $\vec{k}$ and $\vec{k'}$ are the incident and scattered photon momenta, θ_0 is the photon scattering angle with respect to the incident photon direction, and $\mathcal{P}_\gamma$ is the signed circular polarization of the photon. $\mathcal{P}_\gamma > 0$ denotes a photon with spin along the momentum direction. $\mathcal{P}_e$ is the electron polarization, and $A^{e\gamma}(\vec{k}\vec{k'})$ is the Compton polarization asymmetry function, given by

$$A^{e\gamma}(\vec{k}\vec{k'}) = \frac{(\frac{1}{k'} - \frac{1}{k})\left[\vec{k}\cos\theta_0 + \vec{k'}\right] \cdot s}{\frac{(k-k')^2}{kk'} + 1 + \cos^2\theta_0},$$

(4.2)

where $\hat{s}$ is the electron polarization direction. The signs in the asymmetry term $\mathcal{P}_\gamma \mathcal{P}_e A^{e\gamma}$ in Eq. 4.1 have been chosen so that the Compton cross-section is greater when the photon and electron spins are aligned in the same direction.

We now develop the expressions for Compton scattering in the SLC frame, where the electron momentum is 2×10^{10} that of the photon. The scattered electrons travel in the incident electron direction. We define the incident and final electron and photon energies in the laboratory frame as E, E', K, K'. We define the kinematical variable y as

$$y \equiv \left(1 + \frac{4EK}{m_e^2}\right)^{-1},$$

(4.3)

where m_e is the electron rest mass, and write the expressions corresponding to the case of complete backscattering in the center-of-momentum frame as

$$K'_{max} = E(1 - y)$$

$$E'_{min} = Ey.$$

(4.4)

For SLC Compton values of 2.33 eV and 45.5 GeV for the photon and electron energies, $y = 0.381$,
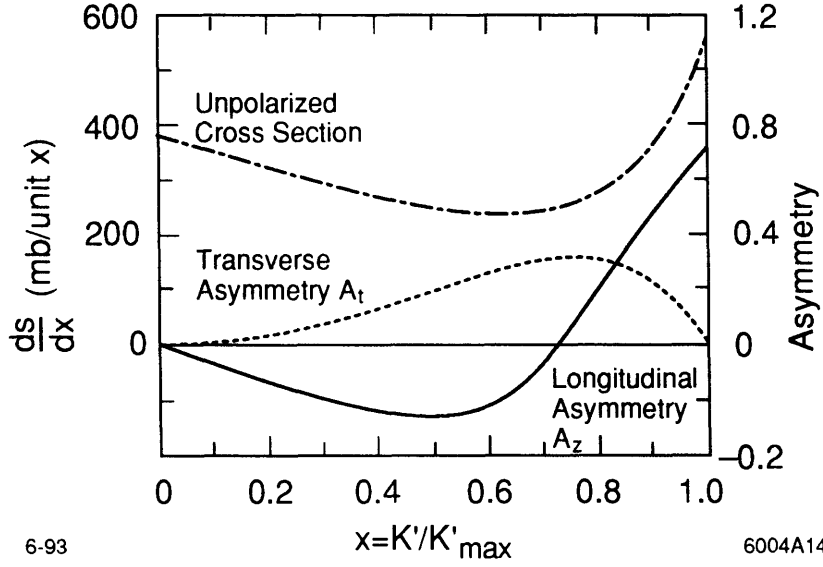
Figure 4-2: The transverse and longitudinal asymmetries for Compton scattering as a function of the kinematical variable x. $x = 1$ for the case of complete backscattering (kinematic edge).

giving a maximum scattered photon energy of 28.3 GeV and a minimum electron energy of 17.4 GeV. The angle of the scattered photon in the lab frame, θ_K, is given by

$$K' = K'_{max}\left[1 + y\left(\frac{E\theta_K}{m_e}\right)^2\right]^{-1} \equiv K'_{max} \cdot x, \tag{4.5}$$

which defines the kinematical variable x. The maximum electron scattering angle is given by

$$\theta_e^{max} = \frac{m_e}{2E}\frac{1-y}{y} = 9.1\mu r. \tag{4.6}$$

The scattered electrons remain within the unscattered beam since the maximum electron scattering angles are smaller than the beam divergence. To obtain the Compton cross-section in the laboratory frame from Eq. 4.1, we use the following transformation:

$$K = \frac{m_e}{2E}k$$

$$x = \frac{K'}{K'_{max}}$$

$$= \frac{1 - \cos\theta_0}{2y + (1 - y)(1 - \cos\theta_0)}.$$

The lab-frame cross-section can be written as a sum of longitudinal and transverse electron polar-

ization asymmetries,

$$\left(\frac{d^2\sigma}{dx\,d\phi}\right)_{Comp} = \left(\frac{d^2\sigma}{dx\,d\phi}\right)_{unpol} \cdot \left\{1 - \mathcal{P}_\gamma\left[\mathcal{P}_z A_z^{e\gamma}(x) + \mathcal{P}_t \cos\phi A_t^{e\gamma}(x)\right]\right\}, \tag{4.7}$$

where ϕ is the azimuth of the photon with respect to the electron transverse polarization. The term in the square brackets has two parts, the first, $\mathcal{P}_z A_z^{e\gamma}(x)$, is the longitudinal term, and the second, $\mathcal{P}_t \cos\phi A_t^{e\gamma}(x)$, is the transverse term. The unpolarized cross-section is given by

$$\left(\frac{d^2\sigma}{dx\,d\phi}\right)_{unpol} = r_0^2 y\left\{\frac{x^2(1-y)^2}{1-x(1-y)} + 1 + \left[\frac{1-x(1+y)}{1-x(1-y)}\right]^2\right\}, \tag{4.8}$$

and the longitudinal and transverse asymmetries are defined as

$$A_z^{e\gamma} \equiv r_0^2 y[1 - x(1+y)]\left\{1 - \frac{1}{[1-x(1-y)]^2}\right\} \cdot \left(\frac{d^2\sigma}{dx\,d\phi}\right)_{unpol}^{-1} \tag{4.9}$$

$$A_t^{e\gamma} \equiv r_0^2 yx(1-y)\frac{\sqrt{4xy(1-x)}}{1-x(1-y)} \cdot \left(\frac{d^2\sigma}{dx\,d\phi}\right)_{unpol}^{-1}. \tag{4.10}$$

Here the polarizations $\mathcal{P}_\gamma$ and $\mathcal{P}_z$ are signed such that positive denotes the spin vector in the same direction as the momentum vector. This convention is similar to the one for Eq. 4.1, and yields a larger cross-section when the electron and photon spins are parallel. Fig. 4-2 shows the longitudinal and transverse asymmetries plotted as a function of the kinematical variable x, which can take on values from zero (for no scattering) to one (for 180° backscattering in the center-of-momentum frame).

The longitudinal asymmetry function has some interesting features. Foremost, the asymmetry is large, approximately 75% in the case of complete backscattering (minimum scattered electron energy at the SLC was 17.4 GeV). This large asymmetry occurs at the kinematic edge of scattering, since the region beyond $x = 1$ is kinematically inaccessible. A dipole magnet was used to analyze the Compton scattered electrons. The region corresponding to $x = 1$ exhibits a "Compton edge", where the signal drops off sharply to zero. This edge was easily observed in the Compton detectors and was used in the position calibration. Another feature of the longitudinal asymmetry is the point at $x = \frac{1}{1+y}$ where the asymmetry goes to zero, the "zero-asymmetry point" (scattered electron energy at the SLC was 25.16 GeV). These two features, the Compton kinematic edge and the zero-asymmetry point were used to calibrate the relative position of the detector to within 250 μm. The transverse position of a given detector channel relative to the beamline determined the acceptance in scattered electron energy of that channel, since the analyzing magnets, SB1 and B1, had a single

effective bend point for all electrons, independent of energy.

First order radiative corrections to polarized Compton scattering were calculated [35]. The effect on the unpolarized cross-section was seen to be less than 0.3%, and the effect on the longitudinal Compton asymmetry function, $A_z^{e\gamma}$, was less than 0.0006 for all scattered electron energies detectable at the SLC. We took as negligible the effects of radiative corrections to Compton scattering in the analysis.

4.2 Compton experimental asymmetry

The asymmetry due to longitudinal polarization of the electrons is given by the $\mathcal{P}_\gamma \mathcal{P}_z A_z^{e\gamma}$ term in Eq. 4.7. This asymmetry is proportional to parallel and anti-parallel electron and photon spin combinations. We measured this asymmetry by forming the asymmetry of the Compton signal size for these states. For a given polarimeter channel, the signal, N_i can be written for the two states as

$$N_i^{\overline{\frac{\text{par.}}{\text{anti-par.}}}} = N_i^{\text{bkgd}} + \int_{x_1}^{x_2} \left(\frac{d\sigma}{dx}\right)_{\text{unpol}} \cdot [1 \pm A_z^{e\gamma} \mathcal{P}_\gamma \mathcal{P}_z] \cdot r(x) dx, \qquad (4.11)$$

where i is the polarimeter channel being observed, x_1, x_2 are the energies at the limits of the channel, $r(x)$ is the response function of the channel, and N_i^{bkgd} is the background signal in that channel. We used these N_i to form the experimental asymmetry (EA),

$$
\begin{aligned}
EA_i &= \frac{\langle N_i^{\text{par.}} \rangle - \langle N_i^{\text{anti-par.}} \rangle}{\langle N_i^{\text{par.}} \rangle + \langle N_i^{\text{anti-par.}} \rangle - 2 \cdot \langle N_i^{\text{bkgd}} \rangle} \\
&= \mathcal{P}_\gamma \mathcal{P}_z \cdot a_i, \qquad (4.12)
\end{aligned}
$$

where a_i, the *analyzing power* of the channel, is defined as

$$a_i \equiv \frac{\int_{x_1}^{x_2} \left(\frac{d\sigma}{dx}\right)_{\text{unpol}} \cdot A_z^{e\gamma}(x) \cdot r(x) dx}{\int_{x_1}^{x_2} \left(\frac{d\sigma}{dx}\right)_{\text{unpol}} \cdot r(x) dx}, \qquad (4.13)$$

which is just the normalized asymmetry function weighted by the response function of the channel and the Compton luminosity and integrated over the acceptance of the channel. The electron beam polarization is simple to extract:

$$\mathcal{P}_z = \frac{EA_i}{\mathcal{P}_\gamma \cdot a_i}. \qquad (4.14)$$

Clearly, several sources of systematic uncertainty affected the determination of $\mathcal{P}_z$. We had to measure EA, the Compton asymmetry, without bias. For the 1993 SLC run, we used dedicated studies to map out the linear range of the relevant channels in the detector, and ensured that we

71

stayed within that range during the run, away from bias-inducing non-linearities. We also had to measure $\mathcal{P}_\gamma$, the light polarization, with accuracy. By determining and compensating for the optical birefringence of the Compton light transport system, we determined the light polarization very accurately. Finally, we had to determine a_i, the analyzing power for the detector channels, with precision. We used the EGS4 Monte Carlo to calculate the response function of the channels, and used detector scans transverse to the beam to locate the Compton kinematic edge precisely (*edge scans*). These sources of systematic uncertainty in the polarization determination are discussed further in chapter 6 and chapter 5.

4.3 Monte Carlo Simulation of the Compton Čerenkov Detector

In order to calculate the analyzing power, a_i, for a given channel in the Compton Čerenkov detector, the Compton asymmetry function, $A_z^{e\gamma}$, had to be integrated over the acceptance of the channel, and normalized, as in Eq. 4.13. $A_z^{e\gamma}$ could be calculated analytically. The response function, $r(x)$, and the channel acceptance limits, required more consideration. For a perfect detector, the $r(x)$ would be constant within the channel walls and zero outside. The channel acceptance limits would be defined by the walls of the channel. This simple picture held down to a few percent level. To achieve a precision of a few tenths of a percent, we had to take into account effects of electromagnetic showers in the detector and the resultant smearing of the resolution function.

In practice, the detector normally operated with lead preradiator in front, as described in section 4.4. The preradiator was used to absorb soft gammas around the beamline, as well as to amplify the signal from the Compton scattered electrons. The finite spatial width of an electromagnetic shower meant that the response function of a given Čerenkov channel was inevitably smeared out beyond the limits of its walls. In lieu of a high-precision electron test-beam, we used Monte Carlo detector simulations to determine the Čerenkov channel response functions in the presence of lead preradiator. We confirmed the EGS simulation by comparing the predicted asymmetries for various preradiator configurations with measured asymmetries.

4.3.1 The EGS4 Monte Carlo program

The simulation of the Compton Čerenkov detector was performed using the Electron Gamma Shower (EGS4) Monte Carlo package [36]. The EGS package simulated the interactions of electrons, positrons and photons with matter over an energy range from 10 keV to 1 TeV. The program

x(cm)
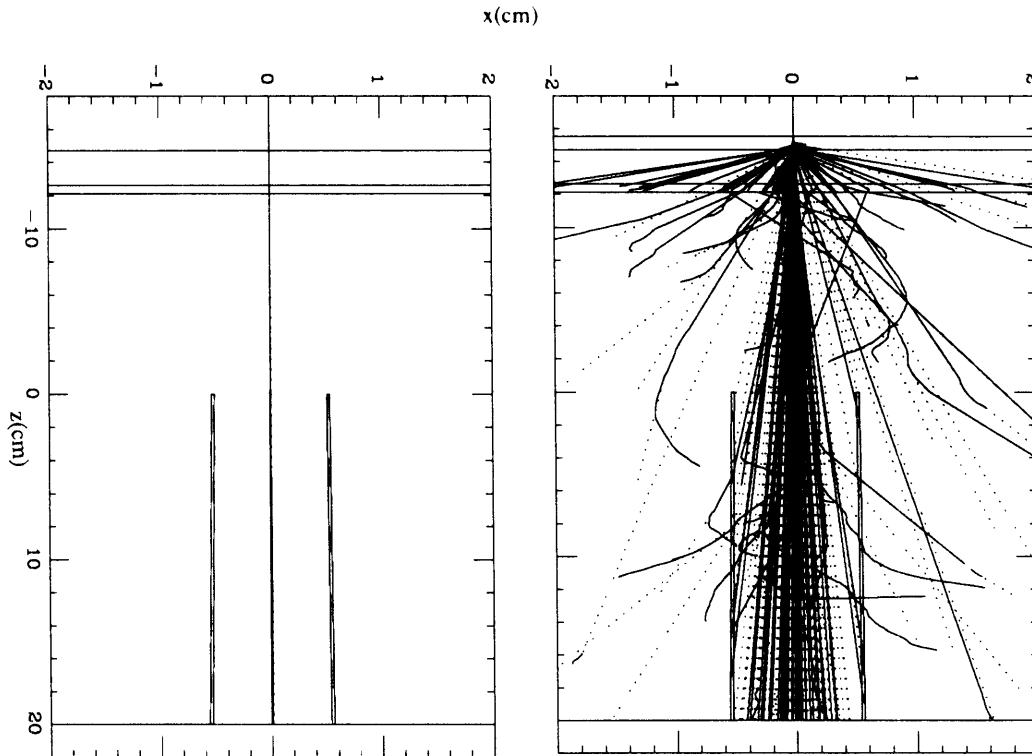
Figure 4-3: Top view of electromagnetic shower in the Compton Čerenkov detector for 10 incident e^-, with no lead preradiator (left) and 0.8 cm lead preradiator (right). The solid lines are electron tracks, while the dotted lines are photon tracks.

took into account photoelectric, Compton, and pair-production interactions, as well as bremsstrahlung, Molière multiple scattering, Møller and Bhabha scattering, as well as positron annihilation in flight. The EGS package recognized all elements and most commonly used metal alloys composite materials. The EGS program sets a world-wide standard and has been used in countless physics experiments over the years, and has been shown to properly simulate the effects of electromagnetic interactions over a wide kinematic range.

The Čerenkov detector modelling was done in two separate ways. The original method, used in the 1992 analysis of the detector, simulated a single channel of the detector. For the 1993 analysis, a full-detector simulation was used, which described all nine channels as well as salient features of the detector body and associated beamline components. The two separate approaches did not differ appreciably in their estimations of the analyzing powers.

Single channel EGS model

The single channel EGS model of the detector, used in the 1992 analysis, has been extensively described elsewhere [37]. We highlight here the features used in the 1993 analysis.
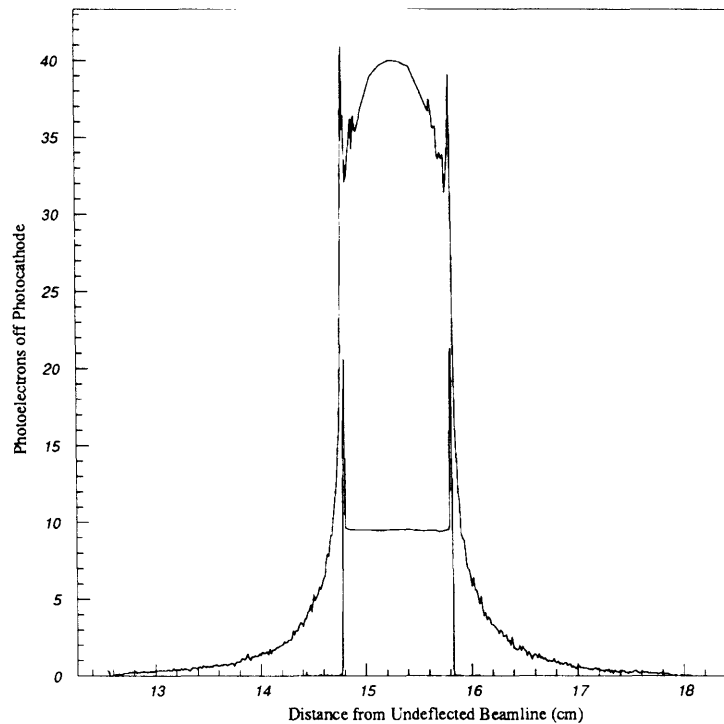
Figure 4-4: Response function for a Compton Čerenkov channel, as calculated by EGS, with 0.8 cm lead preradiator (outer curve) and without (inner curve).

The Compton scattered electron beam was modeled at the beginning of the effective center-of-bend point of the dipole magnets. The initial deviation of an electron from the center was determined from a gaussian distribution corresponding to the 190×10^{-4} cm spot size at the center-of-bend point. The initial angle was similarly determined from a gaussian distribution corresponding to the $50\mu r$ beam divergence. The energy of the electron, which determined the transverse kick of the dipole field, was determined from a flat distribution. This ensured the response function would be independent of the Compton cross-section.

The Compton detector hardware has been described in a previous chapter. There were two pieces of lead preradiator, 0.8 cm and 1.7 cm in thickness[1], that could be inserted into the space right before the detector entrance window. Their primary purpose was to shield the Compton detector from soft electromagnetic radiation that accompanied the SLC electron beam pulse. Their secondary purpose was to amplify the Compton signal by causing electromagnetic showers within the lead. This amplification of signal was achieved at a cost of lower resolution.

Fig. 4-3 shows top views of a single Čerenkov channel, as modelled by the EGS Monte Carlo. The left illustration depicts a detector with no lead preradiator, while the right illustration depicts one

---

[1] Periods of the 1993 run had preradiator thicknesses of 0.3 cm and 0.6 cm installed.

with 0.8 cm of lead preradiator in front of the detector body. Ten Compton scattered electrons are shown incident on the detector. The no-preradiator illustration on the left shows small amount of electromagnetic showering, well within the channel boundaries, while the lead preradiator illustration on the right shows significant showering in the lead. The showering produced by the preradiator both amplified the signal and smeared it out. Fig. 4-4 shows the response function for the two cases: with and without lead preradiator. Without lead preradiator, the response was smaller in amplitude, and quite flat across the acceptance of the channel. There were "ears" at the edges, due to the channel walls, but their effect was negligible. The response function with lead preradiator was much larger in amplitude, as expected, and had tails that extend well into the neighboring channel's acceptance. It was precisely these tails that we wished to model with the EGS Monte Carlo. If we did not have to use the lead preradiator in front of the detector, we could have made an acceptably precise measurement without any detector modelling or EGS.

Full detector simulation and analyzing power determination

The analyzing powers for the 1993 run were obtained from and EGS model of the entire Čerenkov detector, since an additional source of background was discovered. A strip of 0.1 inch thick lead shielding was placed between the outer wall of channel 1 and the aluminum gas containment cannister of the Compton detector. This strip of lead, called the *Pb shield*, was inserted to shield the Compton detector from soft radiation from the SLC Beamsstrahlung Monitor, located directly across the beampipe from the Compton detector. Since the shield was placed in a location close to the minimum of the Compton asymmetry curve, it had the unwanted effect of lowering the measured Compton asymmetry in the inner channels by rescattering negative asymmetry electrons that were initially outside the acceptance of the detector back into the detector. Later in the 1993 run, the Pb shield was found to be unnecessary, and removed. A full detector simulation with the lead shield added indicated negligible effects in the outer channels which were used to determine the polarization. Fig. 4-5 shows the EGS simulation for a single Compton scattered electron causing a shower in one of the inner channels, and the effects of the Pb shield. Fig. 4-6 shows a similar simulation for an electron incident on one of the outer channels. The inner channels suffered significant rescattering from the Pb shield. However, the outer channels were not noticeably affected.

Fig. 4-7 shows the response functions for channel 2 without and with the Pb shield. The top plot shows a typical response function for the channel. The bottom plot shows the response function for the same channel, with the effects of the Pb shield included. The shield had an observable effect on the inner channels. The outer channels were not affected. Fig 4-8 shows similar plots for channel 7. The two responses, with and without the shield, look identical. This is understandable, as the shield initiated small, localized electromagnetic showers that did not penetrate more than a few

x (cm)
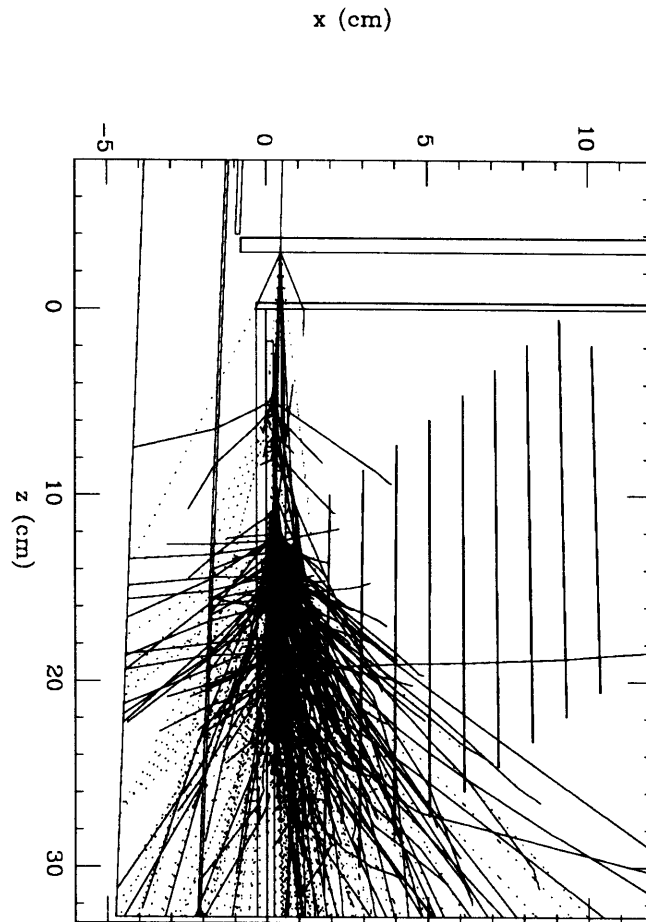
Figure 4-5: A top-view of a full-detector EGS simulation, with the Pb shield in between Čerenkov channel 1 and the containment cannister. A Compton scattered electron is shown incident on one of the inner channels. The inner channels suffered significant rescattering from the shield.

centimeters into the detector.

Due to the presence of the Pb shield for most of the 1993 run, we choose to include only channels 6 and 7 in the polarization determination. These channels have the advantage of being located in region of very high Compton asymmetry. Since the kinematic edge falls in channel 7, detector position scans, described in section 6.2, calibrated the position of these channels quite precisely, to $\approx 250\mu m$.

After the response functions of the Čerenkov channels were determined with the EGS simulations, we determined the analyzing power by using Eq. 4.13. The analyzing powers used for normal running during the 1993 run are presented in Table 6.4.

76
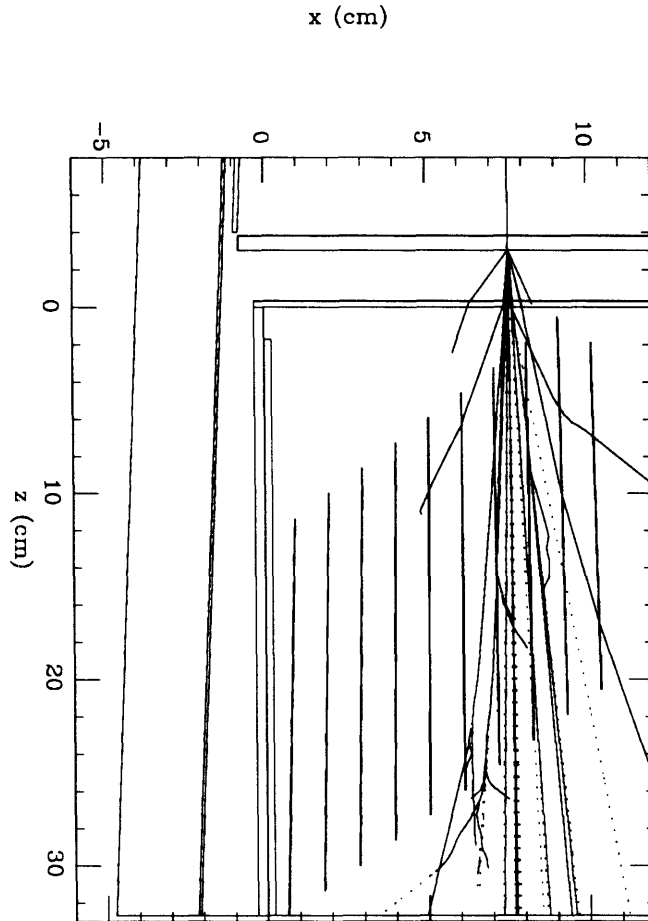
Figure 4-6: A top-view of a full-detector EGS simulation. with the Pb shield in between Čerenkov channel 1 and the containment cannister. A Compton scattered electron is shown incident on one of the outer channels. The outer channels did not suffer much rescattering from the shield.

4.4 Compton polarimeter operation

The Compton polarimeter was run continuously for the 1993 run, with some breaks for routine maintenance (flashlamp changes, Čerenkov gas changes), systematic checks (laser timing, position, phase scans, kinematic edge scans, linearity checks) and emergency repairs (laser hardware repairs, burnt optics replacement). The polarimeter running and online data selection are described in more detail below.

The data were written to tape in two separate groups. A "raw" polarimeter data stream was formed, containing the status and of all detector elements and ADCs for every laser-on pulse and a corresponding laser-off pulse, and written to tape every 150 beam crossings. A separate "summed" stream was formed, containing sums of all Čerenkov channels separately for each combination of photon and electron helicity (as well as laser-off), and written to tape every 20,000 beam crossings.

Detector Response Function (Channel 2)
with Pb Preradiator = 0.762 cm

No Pb Shield in place.

0.226 cm of Pb Shield in place
outside Ch 1

photoelectrons off photocathode

cm from undeflected beamline
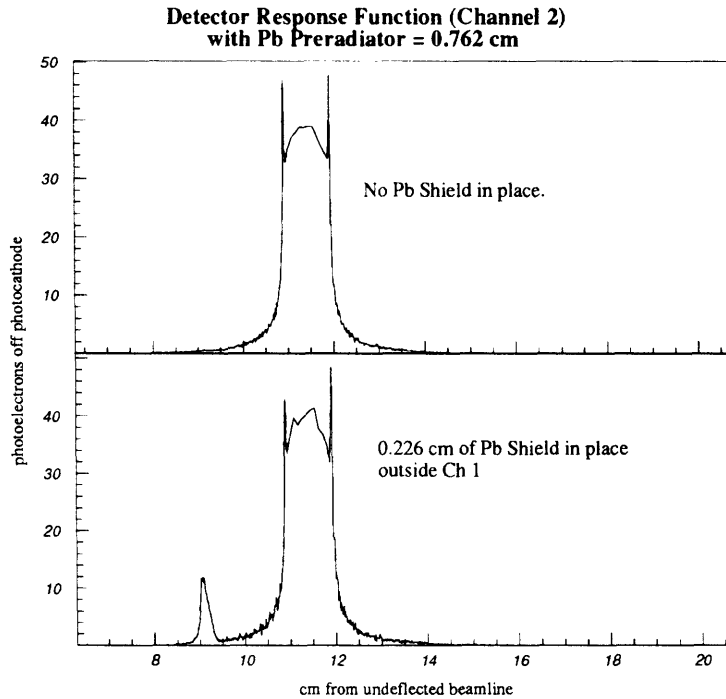
Figure 4-7: The response function for Čerenkov channel 2, with (bottom) and without (top) the Pb shield in place. The effect of the Pb shield is evident in the lower plot.

In addition, the summed data stream contained all photodiode sums were written out for each photon helicity and the laser-off state. The following data analysis involves mainly the "summed" data. The "raw" data was checked at random intervals to ensure the two data streams matched.

4.4.1 Compton polarimeter Online

The Compton polarimeter data acquisition has already been described in section 3.2. The polarimeter acquisition was a timed system, not a triggered system. Data were acquired from all polarimeter channels at 120 Hz. The following criteria were applied to the data as it came in:

- For the **raw** data stream:

  1. If the Compton laser fired, the beam crossing was included in the data stream.

  2. A subsequent pulse for which the Compton laser did not fire was also included in the data stream.

- For the **summed** data stream:

Detector Response Function (Channel 7)
with Pb Preradiator = 0.762 cm
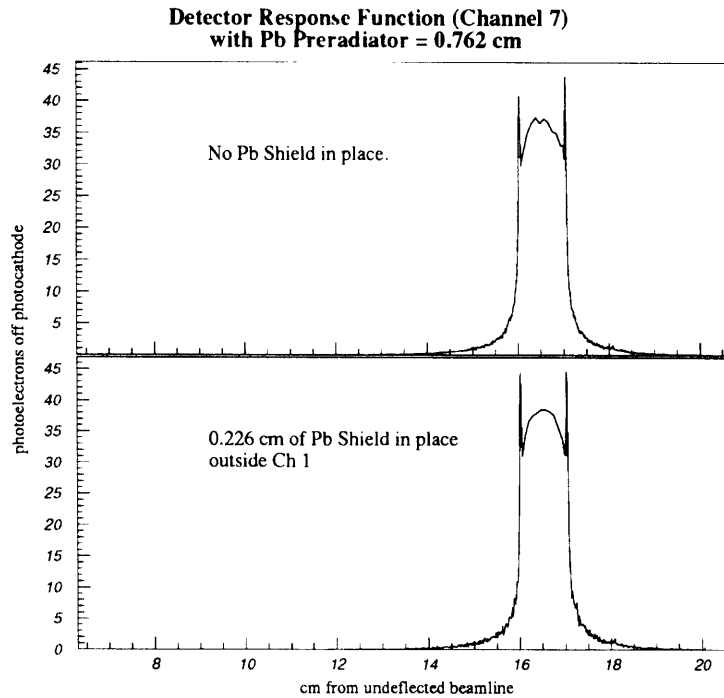
Figure 4-8: The response function for Čerenkov channel 7, with (bottom) and without (top) the shield in place. The shield had no effect on the outer channels.

1. If the electron and positron toroid signals in both the South and North Arc of the SLC passed a threshold (the *toroid veto*), ensuring that electrons were present and e^+e^- collisions were occurring at the SLC IP, and

2. if the signal in channel 9 of the Čerenkov was below a set threshold, ensuring that the noise in the polarimeter channels was tolerable,

then the data from that beam crossing was added to the running sum.

The raw data stream contained all the data from all the various polarimeter ADC's and bit registers. The summed stream contained in addition to the data from the polarimeter channels, slow analog monitor data and a *ringbuffer* of raw data from the last 100 beam-crossings used in the summation. Since the ringbuffer data was essentially a random sampling of raw data, it was very useful in estimating systematic errors such as electronic noise and biases in the Čerenkov channels and among laser photodiodes.

4.4.2 Data processing

The ADC counts from the each of the 9 Čerenkov channels were summed and written as a two dimensional matrix of data, one index denoting the two separate electron helicities, the other denoting the photon helicities (and the laser-off state). Separate summations were made of the number of beam crossings, the ADC counts, as well as the square of the ADC counts.

Approximately every three minutes, accumulated data from $\approx$ 20,000 beam crossings was written to tape in a format called a *data bank*. Not all polarimeter data banks contained 20,000 beam crossings, since the toroid and channel 9 threshold vetos prevented some beam crossings from being included in the sum. The following selection criteria were imposed on the banks before they were used in the polarization determination:

1. The bank had to have at least 100 beam crossings in each of the four photon – electron helicity-indexed banks, to ensure proper statistics for the Compton asymmetry measurement.

2. The voltages on the Compton Pockels Cells (the CP and PS) had to have been at the nominal values. The Compton light polarization analysis varied the voltages on the two Pockels Cells (section 5.2). Every third Compton measurement was made with the Pockels Cell voltages at the nominal point. The nominal voltages on the Pockels cells were chosen such that the light was circularly polarized at the SLC IP. These nominal voltages were changed as necessary.

3. We required that the electron toroid threshold veto, as described above, was operational. Erroneous inclusion of missing electron pulses in the Compton asymmetry calculation would have effectively lowered the measured asymmetries and the extracted polarizations.

4. We required that the lead preradiator thickness in front of the detector was either 0.6 cm, 0.9 cm, 0.85 cm or 2.5 cm, which were the thicknesses for which analyzing powers were calculated. The amount of preradiator used differed for different detector configuration and calibration eras.

5. We required that the detector table position, as determined by the linear potentiometer readback, was within 1.36 mm of the nominal position. Within this range, the analyzing powers were corrected for any deviation from nominal position.

6. The (laser-on) signal plus (laser-off) background from either channel 6 or 7 of the Čerenkov detector was required to be greater than 35 counts. To ensure that the photomultiplier tubes were operating in the linear regime, the pedestal subtracted large-signal (PH^+) was constrained for channels 6 and 7 to be: $40 > PH^+ > 440$. The linearity correction made within this region are discussed below. Compton runs with signal outside this region were discarded.

80

After the selection criteria were applied, the data from the banks remaining were used to form the raw Compton scattering asymmetries as in Eq. 4.12. The signals (N_i^{par}, $N_i^{\mathrm{anti-par}}$) and background (N_i^{bkgd}) were identified as $N_{e,\gamma}$, the mean ADC counts (sums divided by the number of beam crossings) for the channel under question for the electron index e and the photon index γ. The electron helicity index had two values, denoting right-handed and left-handed electrons. The photon helicity index had three values, denoting right-handed, and left-handed light, and another one indicating the laser was off (background measurement).

The statistical error on the individual $N_{e,\gamma}$ was calculated using the average sum of the counts squared, $S_{e,\gamma}$. The error is then simply

$$\delta N = \sqrt{\frac{S - N^2}{n}},$$

where n is the number of beam crossings collected for the e,γ helicity combination for which N is the mean of the ADC counts, and S is the mean of the ADC counts squared. The statistical error on the experimental asymmetry, δEA_i, was then calculated in the normal manner. The typical statistical error on the beam polarization determination from a data bank containing 20,000 beam crossings was 1%. We note that the error on beam polarization determination was limited not by statistics, but by various systematic errors, which are discussed in proceeding chapters.

From the experimental asymmetry, EA, we formed the electron beam polarization using the analyzing power of the appropriate channel and the light polarization, $\mathcal{P}_\gamma$, as used in Eq. 4.14. The light polarization (chapter 5) analysis yielded a list of $\mathcal{P}_\gamma$ relevant to different times of polarimeter operation. The analyzing power used also varied, depending on the position calibration and lead configuration era.

We obtained separate right-handed and left-handed beam polarizations, from experimental asymmetries calculated separately for right-handed and left-handed electrons. From this we determined the polarization asymmetry, $A_\mathcal{P}$, for use in correcting A_{LR} for systematic biases in section 9.1. Since the left and right handed electrons were polarized to almost exactly the same magnitude, this asymmetry was very small $(3.3 \pm 0.1) \times 10^{-3}$.

We averaged the right and left-handed beam polarizations and obtained the mean beam polarization. We then associated the SLD Z events with the polarization measurement nearest in time. We discarded events which were taken more than an hour before or after a valid beam polarization measurement. The results of this association are shown in Fig. 4-9. Since the A_{LR} measurement
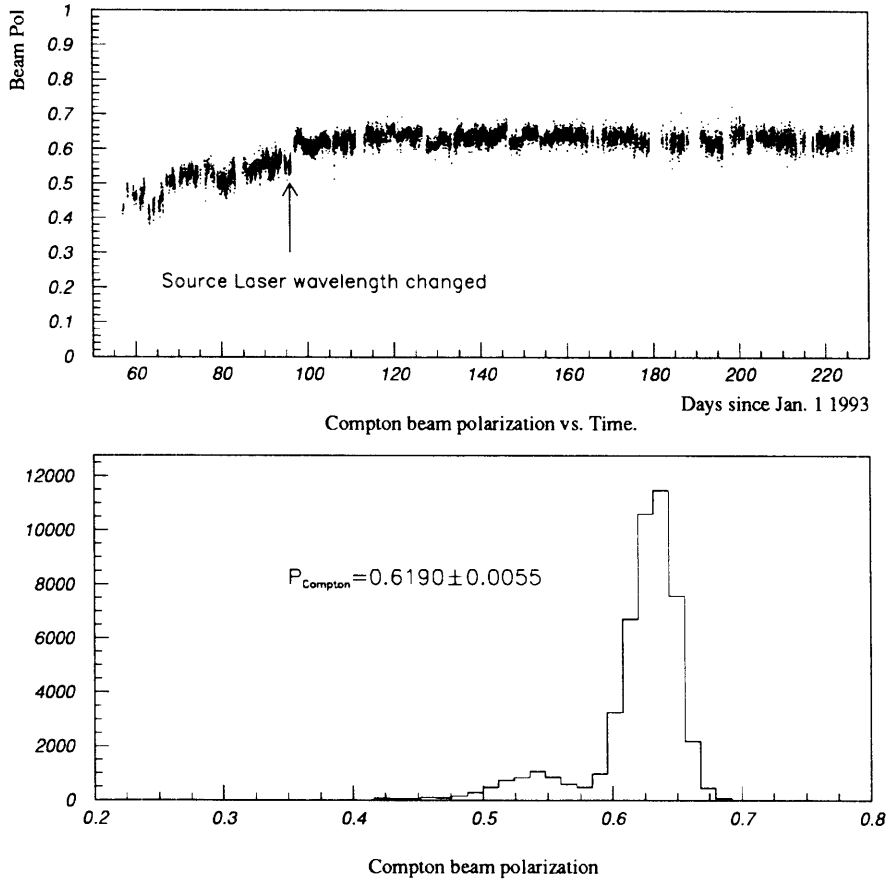
Figure 4-9: The Compton beam polarization as associated with each Z event. The upper plot shows a point for each Z event, and the lower plot is a histogram of the same data.

requires the luminosity weighted beam polarization, we formed the average,

$$\mathcal{P}_C = \frac{1}{N_Z} \cdot \sum_{i=1}^{N_Z} \mathcal{P}_i = 0.6190 \pm 0.0055 \qquad (4.15)$$

where $\mathcal{P}_C$ is the average luminosity-weighted polarization at the compton detector. However, before we can use this to determine A_{LR} we must correct for small effects that can make the polarization as measured at the Compton IP different from that at the SLC IP. This correction is estimated in chapter 7.

Chapter 5

Light Polarization determination for the Compton Polarimeter

This chapter presents the technique used to determine the light polarization used in the polarization determination by the Compton polarimeter. As Eq. 4.14 has shown, the circular polarization of the light, $\mathcal{P}_\gamma$, appears in the beam polarization determination linearly. The light polarization, $\mathcal{P}_\gamma$, was determined to an uncertainty of $\approx$ 2% for the 1992 run of the SLC. For the 1993 run, the light polarization determination was done separately for two eras. In the early part of the run, we did not have the ability to scan the laser polarization through its maximum value, and were unable to make a precise determination of the laser polarization. We have divided this era into seven epochs for further consideration. The systematic uncertainty on the light polarization for this part of the run $\delta\mathcal{P}_\gamma/\mathcal{P}_\gamma \approx 2.1\%$. Starting in late April, we installed two Pockels cells, and started automatic scanning of their voltages. During any particular scan, as the voltages on the Pockels cells varied, the circular polarization of the light swept through its maximum. Using data from these scans, we were able to determine the effects of light transport elements on the polarization, and achieve a systematic uncertainty on the light polarization of $\delta\mathcal{P}_\gamma/\mathcal{P}_\gamma = 0.6\%$ for the *AutoPockscan era*.

5.1   Optics Theory

We begin the discussion of polarized light with a brief introduction to the Stokes parameters and the Stokes vector [38], [39]. Any monochromatic, coherent, arbitrarily polarized light can be decomposed

into a superposition of two linearly polarized components:

$$\vec{E}_{x,y}(t) = \begin{bmatrix} E_x\, e^{i(kz-\omega t)}\, e^{i\delta_x} \\ E_y\, e^{i(kz-\omega t)}\, e^{i\delta_y} \end{bmatrix} \tag{5.1}$$

where $\delta_{x,y}$ are the phases of the two linear states, polarized along axes labelled x, y. The $e^{i(kz-\omega t)}$ denotes light travelling along the $+z$ direction. We will omit this term from now on.

The Stokes parameters, S_0, S_1, S_2, S_3 are defined as follows:

$$S_0 = <E_x^2> + <E_y^2>$$
$$S_1 = <E_x^2> - <E_y^2>$$
$$S_2 = 2 <E_x E_y \cos(\delta_y - \delta_x)>$$
$$S_3 = 2 <E_x E_y \sin(\delta_y - \delta_x)> \tag{5.2}$$

The time-averages denoted by $<E>$ are presumed to be over a large enough interval so as to be independent of the length of the interval.

The Stokes parameters can be determined by measurements of the intensity of the total light wave, I_0, and the intensities transmitted by ideal polarizers that transmit the x, y, u, v linear components (where the u, v axes are rotated $45°$ with respect to x, y), $I_{x,y,u,v}$, and polarizers adjusted to transmit l, r, — the left and right handed circular components — yielding $I_{l,r}$. Right (left) handed circular light, also referred to as positive (negative) helicity light, results when E_x, E_y in Eq. 5.1 are of equal amplitude, and $\delta_y - \delta_x = +(-)\frac{\pi}{2}$.

In terms of these intensities, the Stokes parameters are:

$$S_0 = I_x + I_y = I_u + I_v = I_l + I_r$$
$$S_1 = I_x - I_y$$
$$S_2 = I_u - I_v$$
$$S_3 = I_r - I_l \tag{5.3}$$

The Stokes parameters can be grouped as a four-vector, $\{S_0, S_1, S_2, S_3\}$. The Stokes representation is useful for decomposing the light wave into a *unpolarized* component, and a (fully) *polarized* component. The Stokes vector for unpolarized light is simply $\vec{S}_{unp} = \{S_0, 0, 0, 0\}$, where S_0 is the intensity of the light. The Stokes subspace (S_1, S_2, S_3) defines a sphere whose points correspond to specific states of elliptical polarization. The four-vector is then $\vec{S}_{pol} = \left\{ \sqrt{S_1^2 + S_2^2 + S_3^2}, S_1, S_2, S_3 \right\}$.

Most importantly, the unpolarized and polarized components can be added to describe the state of the light wave, $\vec{S} = \vec{S}_{unp} + \vec{S}_{pol}$, even when the unpolarized component is incoherent. Since $S_{1,2,3}$ are differences, the unpolarized part subtracts out. The intensity of the unpolarized component contributes to S_0, and the difference between S_0 and the others can be used to determine the fraction of unpolarized light.

For the 1993 data, we measured I_r and I_l. This determined S_0 and S_3. We did not explicitly measure S_1 and S_2, but by scanning the phase shifts (adjusting the amplitudes and $\delta_{x,y}$ in Eq. 5.1) we determined the operating point at which the light was circularly polarized. The only non-zero Stokes parameters at this point are S_0 and S_3, and the function $1 - \frac{S_0}{S_3}$ determines the amount of unpolarized light.

We work in the linearly-polarized (x, y) basis, using the two-component basis for the electric field vector already introduced, commonly known as the *Jones vector* representation. The initial light wave in Eq. 5.1 can be rewritten as follows:

$$\vec{E}_{initial} = \left[\begin{array}{c} E_x \\ \\ E_y \, e^{i\phi} \end{array} \right] \tag{5.4}$$

where E_x and E_y are the amplitudes polarized along the x and y axes, and ϕ is the relative phase.

In this basis, the various optical components can be represented as $2 \; X \; 2$ matrices. We define the matrices LIN, CP, and PS to describe a linear polarizer and compensators, which advance the phase of linear-polarization component along the fast axis.

The linear polarizer is defined such that it transmits light polarized along one axis only (chosen here to be the x axis):

$$LIN = \left(\begin{array}{cc} 1 & 0 \\ 0 & 0 \end{array} \right) \tag{5.5}$$

We define the first compensator, aligned along the u, v axes which are rotated by $45°$ with respect to the x, y axes:

$$CP = \begin{pmatrix} \cos\frac{\pi}{4} & -\sin\frac{\pi}{4} \\ \sin\frac{\pi}{4} & \cos\frac{\pi}{4} \end{pmatrix} \begin{pmatrix} 1 & 0 \\ 0 & e^{i\Phi_{CP}} \end{pmatrix} \begin{pmatrix} \cos\frac{\pi}{4} & \sin\frac{\pi}{4} \\ -\sin\frac{\pi}{4} & \cos\frac{\pi}{4} \end{pmatrix}$$
$$= \frac{\sqrt{2}}{2} \begin{pmatrix} 1 + e^{i\Phi_{CP}} & 1 - e^{i\Phi_{CP}} \\ 1 - e^{i\Phi_{CP}} & 1 + e^{i\Phi_{CP}} \end{pmatrix}, \tag{5.6}$$

where Φ_{CP} is the phase shift imparted by the first compensator. The rotation matrices are indicated explicitly.

We define the second compensator in a similar manner to the first, but aligned along the x, y axes, thus needing no rotation.

$$PS = \begin{pmatrix} 1 & 0 \\ 0 & e^{i\Phi_{PS}} \end{pmatrix}, \tag{5.7}$$

where. Φ_{PS} is the phase shift imparted by the second compensator.

After propagating through the linear polarizer (LIN), first compensator (CP) and second compensator (PS), the electric field vector is:

$$\vec{E}_{out} = A \begin{bmatrix} 1 + e^{i\Phi_{CP}} \\ e^{i(\Phi_{PS})}(1 - e^{i\Phi_{CP}}) \end{bmatrix} \tag{5.8}$$

where A^2 is the intensity of the light.

We rewrite Eq. 5.8 factoring out a common phase:

$$\vec{E}_{out} = A' \begin{bmatrix} \cos\frac{\Phi_{CP}}{2} \\ -i\,e^{i(\Phi_{PS})}\sin\frac{\Phi_{CP}}{2} \end{bmatrix} \tag{5.9}$$

Thus the CP phase shift controls the relative *amplitude* of the two components, and the PS phase shift controls the relative *phase* between the two. By adjusting the two compensators, we can create an *arbitrarily elliptically polarized* state. Equations 5.8 and 5.9 describe left-handed circular light if $\Phi_{PS} = 0$ and $\Phi_{CP} = \frac{\pi}{2}$. Right handed light differs by a phase shift of $e^{i\frac{\pi}{2}}$ in the E_y component, which changes the $-i$ to a $+i$.

Helicity Filter

After we have created and transported the circularly polarized light, we must measure it. We use helicity filters, which transmit either left or right handed light only, to analyze the light.

We construct a filter for left or right circularly polarized light in the linearly polarized basis. The physical elements of such a helicity filter are a $\frac{\lambda}{4}$ plate followed by a linear polarizer — the fast axis of the $\frac{\lambda}{4}$ plate aligned at $\pm 45°$ to the axis of the linear polarizer.

We present the matrices for helicity filters, (up to a normalization constant). The $\frac{\lambda}{4}$ plate at $45°$ is:

$$O_{\frac{\lambda}{4}} = \begin{pmatrix} 1+i & 1-i \\ 1-i & 1+i \end{pmatrix} \tag{5.10}$$

And the linear polarizer is given in Eq. 5.5.

Combining the two in the proper order to construct a helicity filter yields:

$$O_{R.H.Filter} = \begin{bmatrix} 1+i & 1-i \\ 0 & 0 \end{bmatrix} \tag{5.11}$$

for a right-handed helicity filter, and

$$O_{L.H.Filter} = \begin{bmatrix} 0 & 0 \\ 1-i & 1+i \end{bmatrix} \tag{5.12}$$

for a left handed helicity filter.

The electric field vector developed in Eq. 5.9 can now be propagated through the appropriate helicity filter, and the circular polarization determined. The intensity of the light described by Eq. 5.9 after a (right-handed) helicity filter is

$$1 - \sin \Phi_{CP} \cos \Phi_{PS} \tag{5.13}$$

We have neglected an overall gain factor. The circular polarization for the light described by Eq. 5.9 is:

$$\mathcal{P}_\gamma = \frac{S_3}{S_0}$$
$$\mathcal{P}_\gamma = - \sin \Phi_{CP} \cos \Phi_{PS} \tag{5.14}$$

where $\Phi_{CP,PS}$ are the phase-shifts imparted by the two compensators.
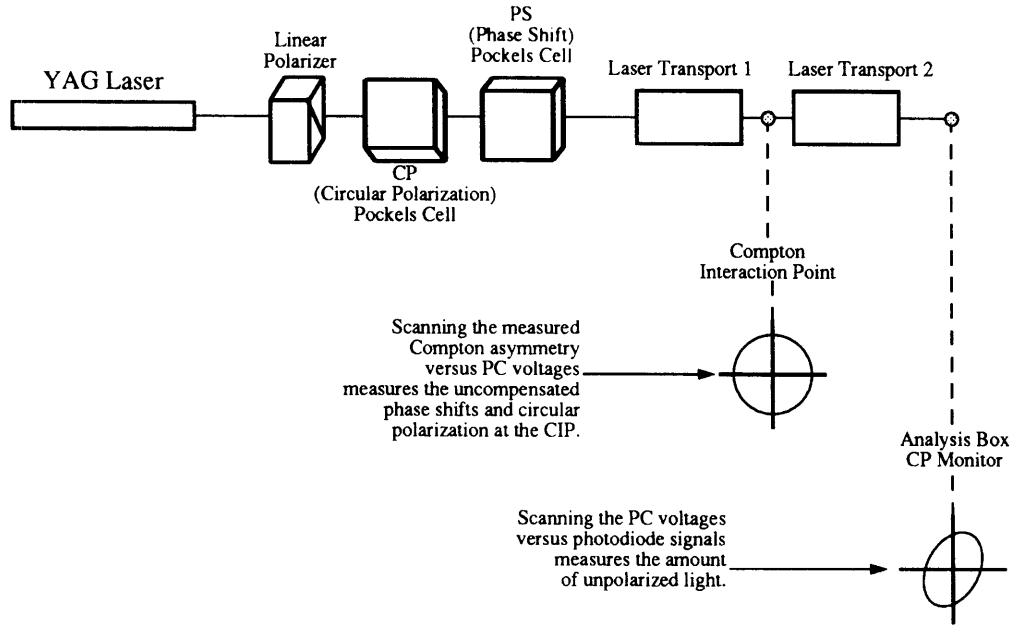
Figure 5-1: Block diagram of the Compton Polarimeter Laser Transport system. The two Pockels cells, CP and PS, produce arbitrary elliptical polarization, which, after it goes through the Laser Transport line, becomes circular at the Compton IP.

The rather complicated set of mirrors and windows that transported the light from the laser to the Compton IP has been presented in Fig. 3-9. We can model this group of mirrors and transports as one optical element, and measure its optical properties. Fig. 5-1 presents a block-diagram of the laser transport system. The set of optical elements from the end of the second Pockels cell to the Compton IP is labelled Laser Transport 1. The mirrors and window from the Compton IP to the Analysis Box is labelled Laser Transport 2. These two sets can be parameterized in the following way:

$$\vec{E}_{CIP} = A \left[\begin{array}{c} \cos\left(\frac{\Phi_{CP} + \phi_1}{2}\right) \\ i\, e^{i(\Phi_{PS} + \phi_2)} \sin\left(\frac{\Phi_{CP} + \phi_1}{2}\right) \end{array} \right] \tag{5.15}$$

The phases $\phi_{1,2}$ are variable phase-shifts, due to the effects of the mirrors, lenses, and windows of the laser transport line. If we construct an equation for the circular polarization, $\mathcal{P}_\gamma$, comparable to Eq. 5.14, we now obtain:

$$\mathcal{P}_\gamma = \sin\left(\Phi_{CP} + \phi_1\right) \cos\left(\Phi_{PS} + \phi_2\right) \tag{5.16}$$

Note that $\Phi_{CP} \to \Phi_{CP} + \phi_1$ and $\Phi_{PS} \to \Phi_{PS} + \phi_2$ due to the effects of the laser transport system. Eq. 5.16 gives the circular polarization assuming there is no unpolarized component, and that we have chosen to work with right handed light from Eq. 5.15 onward.

If $\Phi_{CP} + \phi_1 = \frac{\pi}{2}$, and $\Phi_{PS} + \phi_2 = 0$ then we have fully circular light at the Compton IP. We call this the *Empirical Model* of the laser transport system. A second, more complicated model of the optical transport system allows for arbitrary compensation for the polarized light, and arbitrary rotation of the major-axis of the resultant polarization ellipse. This model was referred to as the *Berek's model*, and is described fully in reference [40].

The photodiodes used to measure the light intensities were investigated for non-linearities in their response and noise pickup from the electronics associated with the laser firing, [41]. We quote a 0.1% systematic uncertainty in measurements made by the Analysis Box photodiodes due to non-linearities and noise pickup. The helicity filter formed by a quarter-wave plate followed by a calcite prism has already been presented. We multiply the $\vec{E}_{CIP}$ in Eq. 5.15 by the desired filter and take the absolute value to obtain equations for signals seen by photodiodes behind the helicity filters. For right and left handed light going through a right-handed helicity filter, we obtain an equation similar to Eq. 5.13 for the intensity of light, I_r, I_l, on the photodiode:

$$I_r = G(1 + \sin\left(\frac{\Phi_{CP} + \phi_1}{2}\right)\cos\left(\Phi_{PS} + \phi_2\right) + U)$$
$$I_l = G(1 - \sin\left(\frac{\Phi_{CP} + \phi_1}{2}\right)\cos\left(\Phi_{PS} + \phi_2\right) + U) \tag{5.17}$$

This is essentially the same as Eq. 5.13, but with the phase shifts $\phi_{1,2}$ added to parameterize the laser transport system. The variables G and U denote the photodiode gain and unpolarized light fraction respectively.

5.2 Automatic Pockels Cell Voltage Scan

The voltages on both Pockels cells were scanned continually about their nominal voltages in order to determine the phase shifts imparted to the light by the transport system. The nominal voltages were chosen to provide circular light at the Compton IP, and updated as necessary. During a typical scan, the voltage on the second Pockels cell (the PS Pockels cell) was held constant while the voltage on the first cell (the CP Pockels cell) was scanned about its nominal (usually $\approx \pm 1600$ volts). Then the first cell was fixed at nominal and the second scanned about its nominal (usually $\approx$ -200 volts).

The voltage on the CP Pockels cell alternated pseudo-randomly between positive and negative. The CP portion of a scan was therefore two portions, interleaved. The variation of the CP voltage around the positive high-voltage nominal point was referred to as the CP-Right portion and the

one around the negative voltage was the CP-Left portion. During the CP portion of a scan, the PS voltage stayed fixed at its nominal voltage.

During the PS portion of a scan, the CP voltage was alternated between the fixed positive and negative nominal voltages, while the voltage on the PS Pockels cell was varied around its nominal.

We performed two sorts of scans to determine the laser polarization parameters. One scan used the Compton scattering asymmetry seen in the scattered electrons by the Čerenkov detector as a function of the Pockels cell voltages, to determine the phase shifts at the Compton IP (EPOL scan). The other used the signal in the Analysis Box photodiodes to determine the phase shifts and the absolute light polarization in the Analysis Box (LP scan).

5.2.1 LP scans

An LP scan consisted of eighty points of 100 beam crossings each. Since the Compton laser fired for approximately 10 beam crossings per 100, the statistical uncertainty of the helicity filter photodiode signals per point was acceptably small. The CP and PS Pockels cell voltages were varied and the signals on the Analysis Box helicity filter photodiodes were noted as functions of these voltages.

A single LP scan consisted of forty CP points in which the CP Pockels cell voltage varied from $\pm800V$ to $\pm2000V$ while the PS Pockels cell voltage was held at a fixed nominal voltage. Then forty PS points were taken in which the PS voltage was varied from $-2000V$ to $+2000V$ and the CP Pockels cell was held at a fixed nominal voltage, (alternating in sign). Since each point consisted of 100 beam crossings, an LP scan took little over one minute to complete. They were performed approximately once per hour.

5.2.2 EPOL scans

An EPOL scan was similar to an LP scan in that the voltages on the two Pockels cells were varied. The difference was that rather than observing the change in photodiode signals, the EPOL scans were used to observe the change in the Compton scattering asymmetry as a function of the Pockels cell voltages. At each voltage, a full Compton run (usually 20,000 beam-crossings) was taken to achieve acceptably small statistical uncertainty on each scan point.

As with the LP scans, off-nominal voltages on the Pockels cell caused the light at the Compton IP to be less circularly-polarized (more elliptically polarized) This led to a smaller asymmetry measured in the Compton scattered electrons as detected by the Compton Čerenkov detector.

An EPOL scan consisted of approximately eighteen full Compton runs of 20,00 beam crossing each, and took about an hour to complete. Several points in an EPOL scan were taken with nominal voltages on the Pockels cells, and these *nominal runs* were used in the beam polarization determination. EPOL scans were performed continually during normal polarimeter operation. One of the assumptions in using these scans to determine laser polarization parameters was that the real electron polarization did not change during the time-span of an individual scan.

5.2.3   Pockels cell scan fits and $\mathcal{P}_\gamma$ determination

The LP scan data were fit to the following equation, obtained by propagating the electric field vector in the Analysis Box through the helicity filter matrix in Eq. 5.11. We allowed for varying photodiode gain and unpolarized light fraction by allowing those quantities to float in the fit along with the transport induced phase shifts and the quarter-wave voltages of the Pockels cells.

$$PD = G(1 \pm \sin \delta_1^{\mathrm{Abox}} \cos \delta_2^{\mathrm{Abox}} + U), \tag{5.18}$$

where PD is the background (laser off signal) subtracted signal seen on the photodiode being fit, G is the gain of the photodiode, and U the unpolarized fraction of the light. The sign after the 1 is $+$ ($-$) if the photodiode in question observed a large signal for positive (negative) voltage on the CP Pockels cell. We labelled this photodiode Analysis Box Photodiode A1 (A2). The variables δ_1^{Abox} and δ_2^{Abox} are defined as follows:

$$\delta_1^{\mathrm{Abox}} \equiv \frac{V_{CP} - \phi_{CP}^{\mathrm{Abox}}}{V_{\frac{\lambda}{4}CP}} \frac{\pi}{2} \tag{5.19}$$

Similarly,

$$\delta_2^{\mathrm{Abox}} \equiv \frac{V_{PS} - \phi_{PS}^{\mathrm{Abox}}}{V_{\frac{\lambda}{4}PS}} \frac{\pi}{2}, \tag{5.20}$$

where $V_{CP,PS}$ are the voltages on the CP and PS Pockels cells, $\phi_{CP,PS}^{\mathrm{Abox}}$ are the phase shifts (measured in volts) *at the Analysis Box*, and the $V_{\frac{\lambda}{4}CP,PS}$ are the quarter-wave voltages of the Pockels cells.

Fig. 5-2 shows data points taken during a typical LP scan, as well as the corresponding fit to Eq. 5.18. We allowed the PS phase shift to be fit separately for positive and negative voltage on the CP Pockels cell. These two cases are shown in Fig. 5-2 as the PS Max fit and the PS Min fit. The difference between the PS phase-shift for the two cases was ≈ 50 volts over the course of the run. This difference was a indication of the limitations of the empirical model of the laser transport system, and was taken into consideration when assigning systematic errors. We assign a systematic
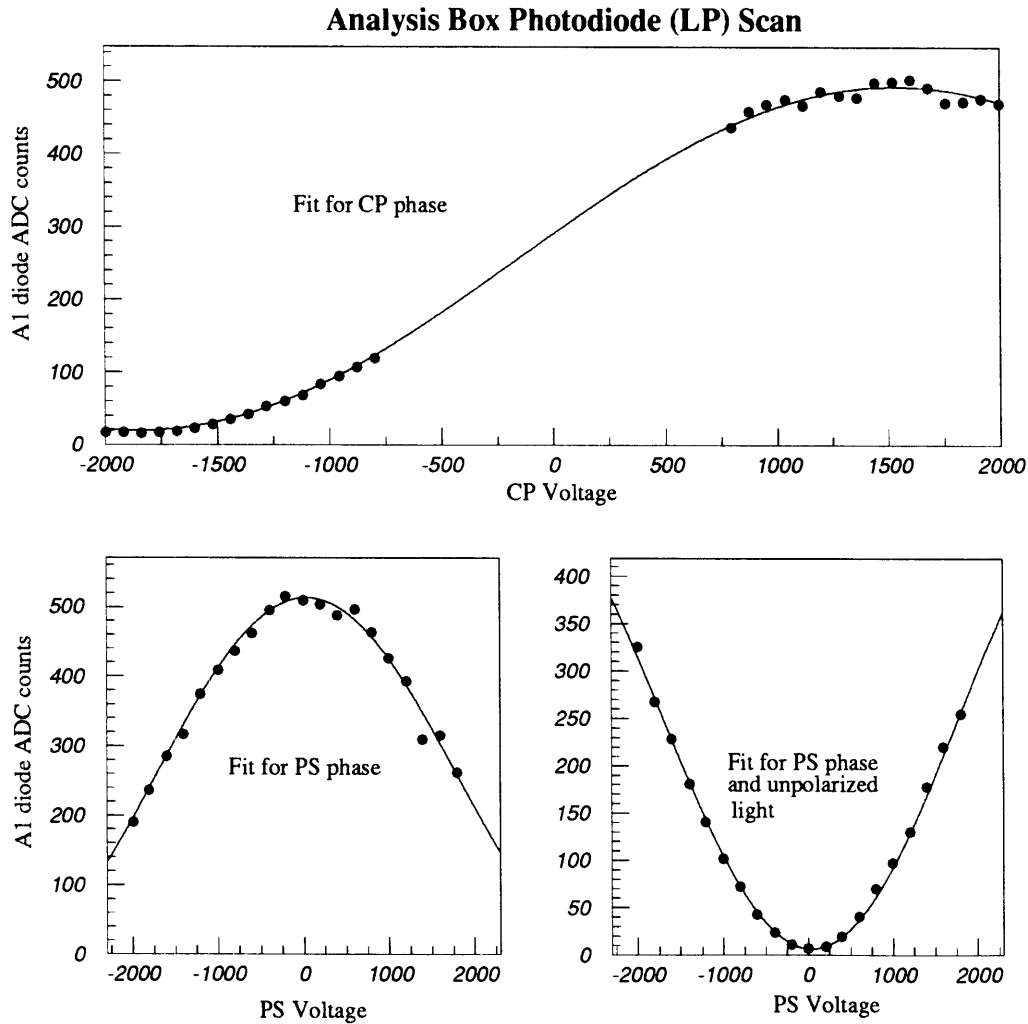
Figure 5-2: Analysis Box Diode data from Pockels cell scan (LP scan) with fit (line) showing CP scan (top) and PS scans (bottom).

error of 0.1% due to limitations of the laser transport model.

Fig. 5-3 shows a histogram of the fraction of unpolarized light as obtained from the fits over the course of the 1993 run. We quote a value of $U = (0.5 \pm 0.5)\%$ for the fraction of unpolarized light in the laser transport system. The width of the distribution in Fig. 5-3 was most probably due to the finite resolution of the Pockels cell high voltage readback.

The LP scans used data from the photodiodes in the Analysis Box. However, the large phase shift from the two uncompensated mirrors between the Compton IP and the Analysis Box made the LP scan data unsuitable for determining the light polarization at the Compton IP. The EPOL scans were used for this purpose. For the EPOL scans, we fit an equation to the asymmetry measured in the Compton scattered electrons, versus the Pockels cell voltages as they were varied in the scans:

Unpolarized Fraction from LP Scans
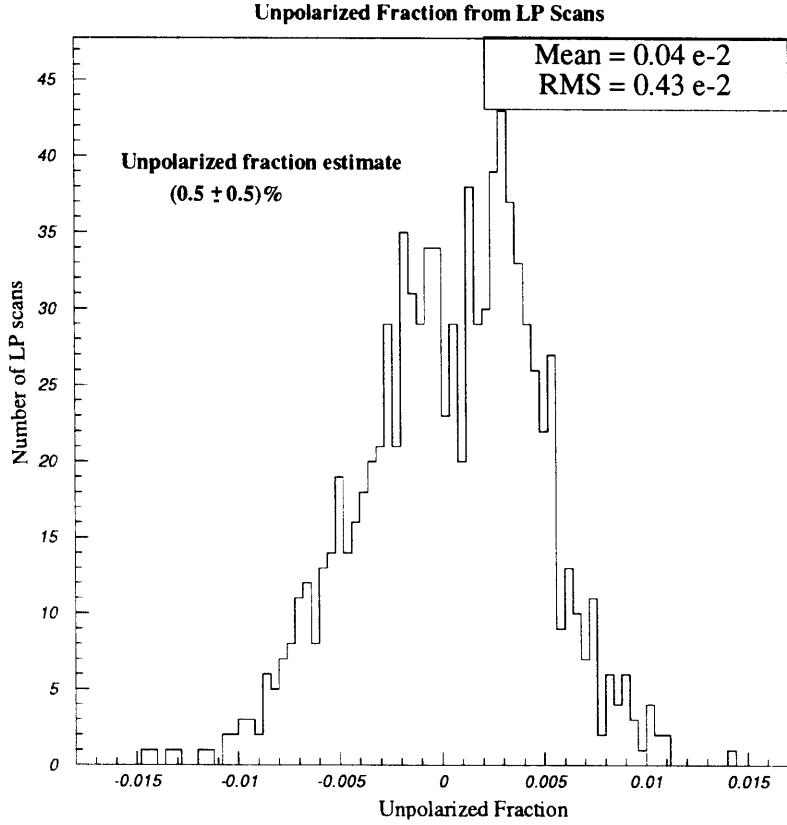
Figure 5-3: Histogram showing the unpolarized light fraction from all the LP scan fits. The unpolarized fraction was estimated to be $(0.5 \pm 0.5)\%$ from this distribution.

$$A_{Ch6} \propto \mathcal{P}_e \mathcal{P}_\gamma$$

$$\mathcal{P}_\gamma = \sin \delta_1 \cos \delta_2 \qquad (5.21)$$

A_{Ch6} is the (raw) asymmetry in the Compton scattered electrons measured by channel 6 of the Compton čerenkov detector. $\mathcal{P}_e \mathcal{P}_\gamma$ is the product of the electron and photon polarizations, and δ_1 and δ_2 are the phase shifts as defined in Eqs. 5.19 and 5.20, but *at the Compton IP*. Fig 5-4 shows points taken during a typical EPOL scan. The points are superimposed on a best-fit curve in which only the phase shifts were allowed to float. The quarter-wave voltages for the Pockels cells were determined from the LP scans and fixed for the EPOL scans.

We took the product of of the phase shifts along the two axes, and multiplied by a factor of 0.995 (to account for the unpolarized light) to determine $\mathcal{P}_\gamma$ from a particular scan. We list the systematic uncertainties for this determination of light polarization below as corrections to be applied to the

Beam Polarization (EPOL) Scan
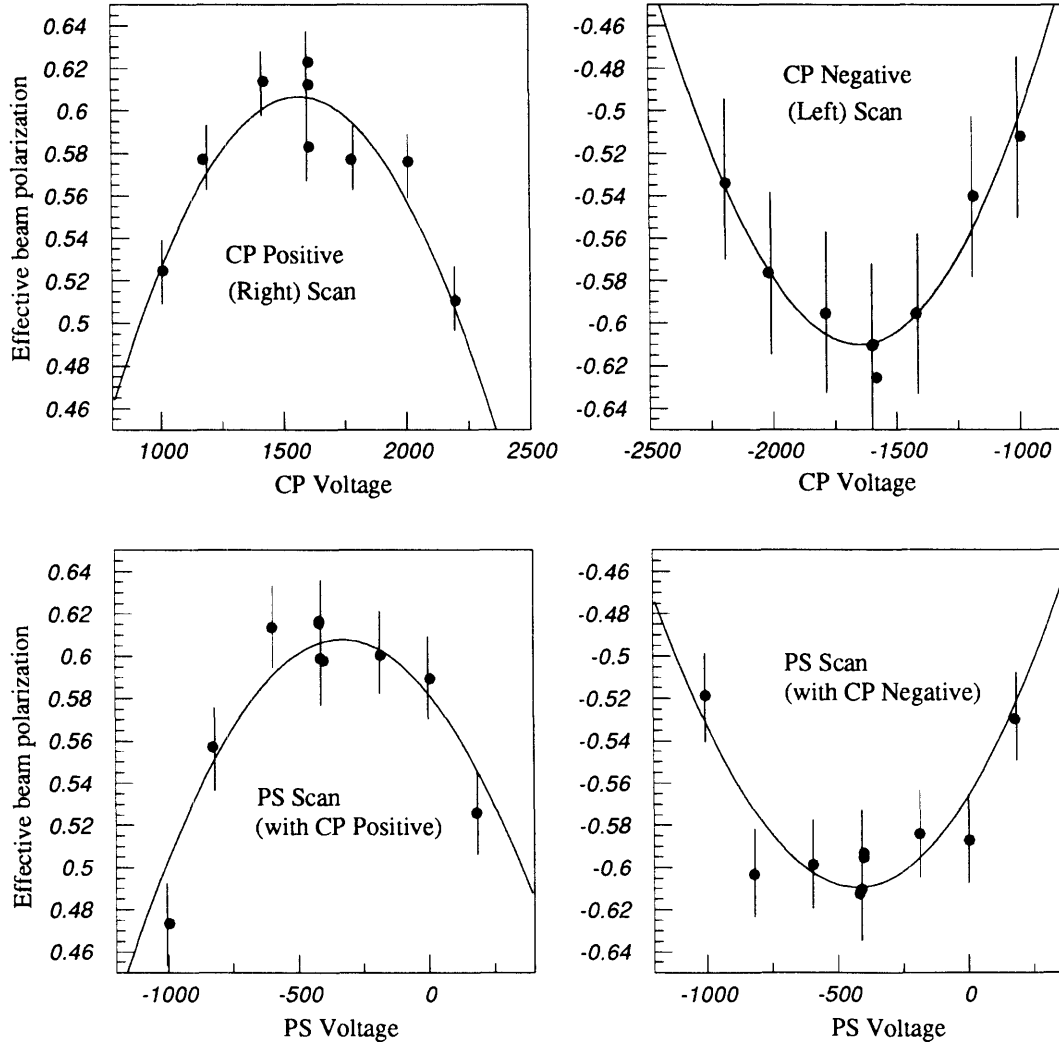
Figure 5-4:   Compton Asymmetry data from Pockels cell scan (EPOL scan) with the fit (line) showing a CP scan (top) and PS scans (bottom).

electron polarization determination. We had the following sources of systematic error:

- Unpolarized fraction :0.5%

- CP Pockels cell phase shift: 0.2%

- PS Pockels cell phase shift: 0.2%

- Uncertainty in the laser transport modelling: 0.1%

- Possible photodiode non-linearities and noise pickup: 0.1%

Light Polarization in the Analysis Box in the Pre-AutoPockscan Era
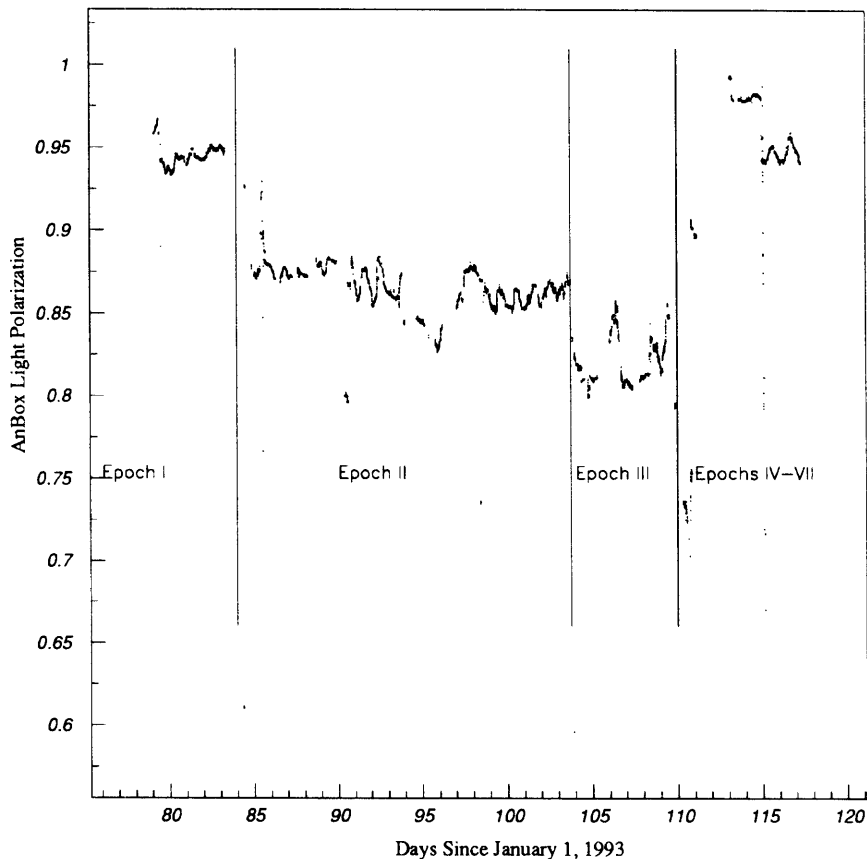
Figure 5-5: $\mathcal{P}_\gamma^{\text{Anal-Box}}$ in the Analysis Box for the pre-AutoPockscan era.

Adding the systematic errors in quadrature, we quote a systematic error of 0.6% on the laser polarization determination during the AutoPockscan era.

5.3   Pre-AutoPockscan $\mathcal{P}_\gamma$ determination

Fig. 5-5 shows the laser polarization as measured by the Analysis Box photodiodes, for the pre-scan era. We identified seven distinct time periods which we analyzed separately. The pre-scan era was plagued with laser-power fluctuations and burnt optics, necessitating many changes of optical components and recalibration of the light transport system, leading to the large number of separate laser-polarization calibration periods. We refer to these periods as pre-scan *epochs*.

We summarize the $\mathcal{P}_\gamma$ determination for the Pre-AutoPockscan era in table 5.1, along with the methods used. Reference [40] presents the data and techniques used in significantly more detail. We

$\mathcal{P}_\gamma$		Method
Epoch I	0.98	From Compton IP measurements
Epoch II	0.96	Manual scan of CP phase
Epoch III	0.96	Manual scan of PS phase
Epoch IV	0.93	Manual scan of both cells
Epoch V	0.99	Same as Epoch IV
Epoch VI	0.97	Manual scan of both cells
Epoch VII	0.99	Automatic scanning begun

Table 5.1: **The light polarization in the Pre-Scan era.**

ascribed a systematic uncertainty of $\delta\mathcal{P}_\gamma/\mathcal{P}_\gamma = 2.1\%$ on the Pre-AutoPockscan data, of which 0.5% is due to the unpolarized fraction and is correlated with the scan era systematic uncertainty. We weighted for luminosity and combined the 0.6% systematic uncertainty from the AutoPockscan era and obtained $\delta\mathcal{P}_\gamma/\mathcal{P}_\gamma = 1.0\%$ for the entire 1993 run.

Chapter 6

Systematic Checks of the Compton Čerenkov Detector

The Compton scattered electrons were detected by the Compton Čerenkov detector. Fig. 3-6 shows a schematic drawing of the Čerenkov system, a nine channel Čerenkov threshold counter arrayed downstream of a dipole magnet.

As described in chapter 4, the electron beam polarization was extracted from the measured Compton asymmetry, once the light polarization was determined and the theoretical analyzing powers were calculated. The calculation of analyzing powers has been discussed in section 4.2. This chapter describes the measurement of the Compton scattering asymmetry in greater detail, along with the associated systematic uncertainties.

An asymmetry measurement does not require knowledge of the absolute gains of the detecting apparatus, but does require that the apparatus respond in a linear manner in the signal region. The linearity of the photomultiplier tubes used in the Čerenkov detector was an issue of some concern. The linear-response regime of the photomultiplier tubes was determined by dedicated tests, and data used in the beam polarization determination were shown to lie in this regime.

A spectrometer like the Čerenkov detector is sensitive to its relative position with respect to the positions and directions of the electrons to be detected, and features in the spectrum can be used to calibrate the position. In polarized Compton scattering, two features in the scattered electron spectrum are obvious: The kinematic edge — there can be no Compton scattered electrons beyond a certain point in the spectrometer, and the zero-asymmetry point — a point on the spectrum where the measured Compton asymmetry goes to zero. Both the kinematic edge and the zero-asymmetry

point have been discussed in section 4.1. The Čerenkov detector was calibrated to satisfactory precision by locating and monitoring these two features of the Compton scattering spectrum.

There was a systematic uncertainty due to the firing of the Compton laser and associated Q-switch mechanism, which induced a small signal on the ADCs used for the Čerenkov detectors. The ADC signals were corrected for this spurious pickup. The amplitude of channel-to-channel cross-talk in the detector was studied and shown to be small.

6.1 Compton Čerenkov Detector Linearity Checks

The main source of instantaneous non-linearity in a detection system based on photomultiplier tubes is due to space-charge saturation in the latter stages of the photomultiplier amplification chain. The linearity of the detector channels was investigated using an *in-situ* system. The photomultiplier tubes used in the detector were mounted in specially designed bases that allowed two separate high voltage supplies to power the photomultiplier tubes. The cathode and the first six dynodes in the amplification chain were powered by the front-end supply (E1), while the remaining dynodes were powered the back-end supply (E2). The dual high voltage supply scheme and the large experimental asymmetry — as high as $\approx 40\%$ at the kinematic edge — allowed us to study the variation of gain with signal size, and investigate possible non-linearities in the system. We changed the E1 voltage, thus changing the number of electrons injected into the amplification chain, without affecting the latter stages where the saturation occurred, since they were controlled by E2. Fig. 6-1 shows the data from one such linearity check. The measured Compton asymmetry is shown as a function of the $e^- - \gamma$ spins-aligned signal on channel 6 of the Čerenkov (PH_6^+), which was increased by increasing the E1 voltage. The asymmetry shown was normalized to the asymmetry measured by channel 7 (for which the voltage was held constant), in order to remove effects of electron beam polarization fluctuations. The onset of non-linearity due to saturation is clearly visible at a signal size of ≈ 200 ADC counts. For $PH_6^+ < 145$, no correction was deemed necessary. The following empirical equation was used to correct the signal.

$$ADC_{\text{Ch.6}}^{\text{corrected}} = \begin{cases} ADC_{\text{Ch.6}}^{\text{raw}} & \text{if } PH_6^+ \leq 145 \\ ADC_{\text{Ch.6}}^{\text{raw}} \cdot \left[1 - 2.94 \times 10^{-7} \cdot \left(PH_6^+ - 145 \right) \right] & \text{if } PH_6^+ > 145 \end{cases} \tag{6.1}$$

We required $40 < PH_6^+ < 440$ for the data used to determine beam polarization. Fig. 6-1 also shows the distribution of the PH^+ signal for channel 6, weighted by the SLC luminosity. Very little data lay in the non-linear regime.

The uncertainty on the points in shown Fig. 6-1 was dominated by statistics. With more data at
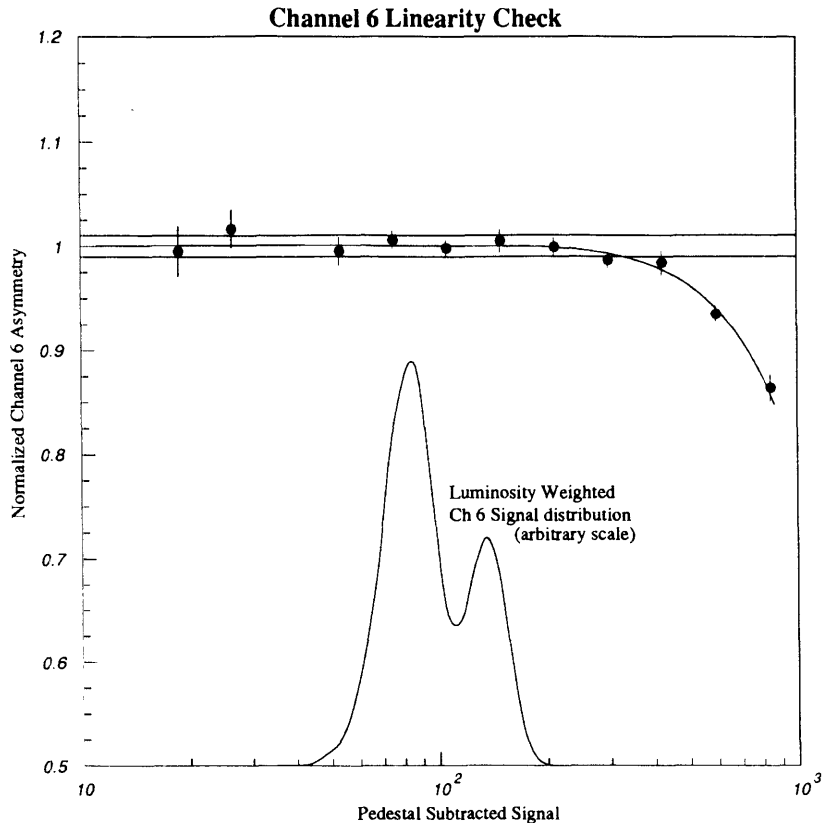
Figure 6-1: Linearity curve for Čerenkov channel 6. The horizontal lines indicate ±1% systematic error. The luminosity weighted distribution of the PH_6^+ signal is also shown. The double-peaked structure was due to Compton luminosity fluctuations (laser and e^-) over the 1993 run.

various pulse heights, the linearity response curve could have been determined with higher accuracy. We ascribed an 0.7% uncertainty to the linearity measurement of channel 6.

Once the linearity characteristics of Čerenkov channel 6 had been determined. we determined the linearity of the channel 7 response to approximately equal accuracy by comparing the asymmetries from the two channels over the entire Compton data sample. The signal size varied considerably over the entire run, due to fluctuations in Compton laser power and electron beam current. The pedestal-subtracted Compton signal in channel 7 ranged from a low of about 30 ADC counts to over 440 ADC counts.

Fig. 6-2 shows the plot for channel 7 of the Čerenkov. There is significant bow in the response of channel 7, contained within a band of ± 1%. We ascribe an uncertainty of 0.7% to the measurement of channel 7 linearity response. The signal in channel 7 was corrected with the following empirical

Channel 7 Linearity Check
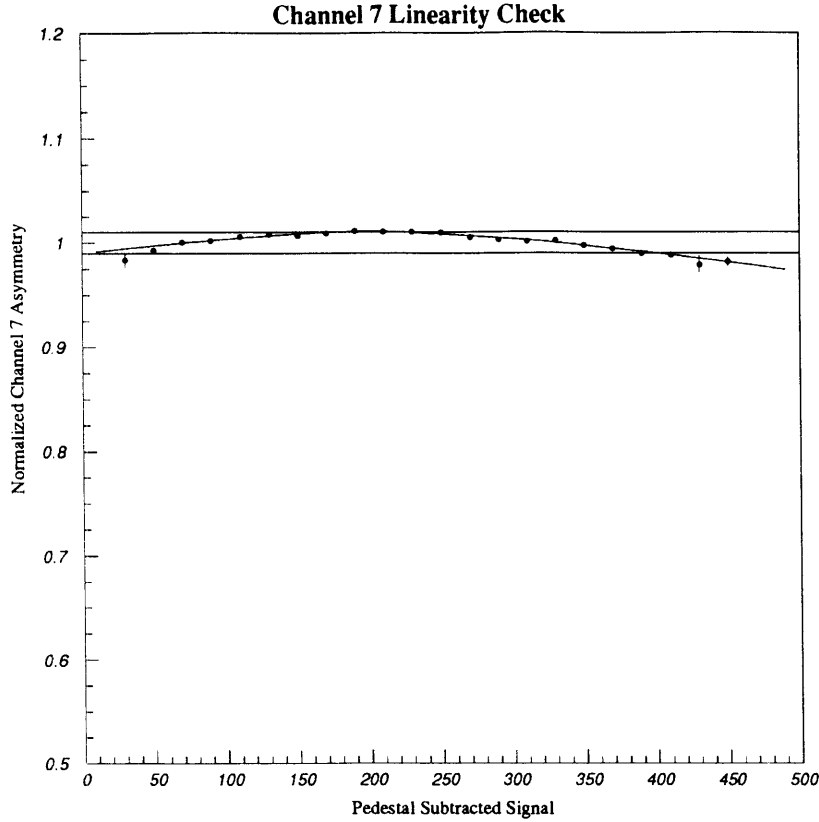
Figure 6-2: Linearity curve for Čerenkov channel 7. The horizontal lines indicate ±1% systematic error.

function:

$$ADC'^{\text{corrected}}_{\text{Ch.}7} = ADC'^{\text{raw}}_{\text{Ch.}7} \cdot \left[1.005 - 0.21 \cdot \left| (\frac{PH_7^+}{200} - 1) \right|^{\frac{3}{2}} \right] . \tag{6.2}$$

We required $40 < PH_7^+ < 440$ for data used in the polarization determination.

6.2 Čerenkov Detector Position Calibration

6.2.1 Kinematic Edge Calibration

The kinematic edge was located by sweeping the Čerenkov detector transversally across the Compton spectrum. The ADC signal from the Čerenkov channel being swept out beyond the kinematic edge showed the following behavior: The signal remained roughly constant as the channel moved toward the kinematic edge, then dropped of linearly as the channel was moved out beyond the edge, followed by a constant, zero signal as the channel lay entirely beyond the kinematic edge. The beginning of

100

the linear drop-off was the point at which the kinematic edge moved across the outer edge of the channel.

The effect of the lead preradiator was to smear out the signal, such that the sharp edges in the figure became rounded, due to broadening of the response functions. However, the EGS4 Monte-Carlo was used to simulate the effect of the lead preradiator to satisfactory precision, as described in section 4.3.

Resolution of edge position

A calibrated linear potentiometer on the detector table provided the horizontal scale for the edge scans. The signal from channel 6, normalized to the signal from channel 3 (adjusted for the change in the Compton cross-section with detector motion) to account for Compton luminosity fluctuations, provided the vertical scale. The misalignment of the projective geometry of the Čerenkov channels as a scan progressed was considered a small effect, and was included in the Monte Carlo simulation. A cubic spline fit was performed on the channel 6 edge scan data, and this spline was then fit to the Monte Carlo data points to extract the edge positions from the scans. The horizontal offset of the Monte Carlo points, the signal scale and offset were allowed to float in the fit [37].

Fig. 6-3 shows an edge scan. This particular scan was taken for the 1992 run, and had no lead preradiator in front of the detector. The kinematic edge is clearly discernible as a sharp edge at the beginning of the downturn in the signal. Fig. 6-4 shows an edge scan done with a 0.3 cm thick lead preradiator in front of the detector, taken on May 2, 1993. Both the data points and the EGS4 Monte Carlo simulation are shown. The agreement is quite good. Three edge scans were performed during the 1993 Compton run. The results are summarized in table 6.1.

Scans of the Compton kinematic edge located the channel walls, but provided no information about possible detector misalignment. As noted earlier, the channel walls in the front section were projective, pointing back to the effective dipole bend point. Detector misalignment could have induced electron showers in the channel walls, changing the response functions. Simulations of edge scans with the detector misaligned showed that edge scans could not be used to diagnose misalignment. The edge scans obtained with a misaligned detector would be nearly identical in shape to one obtained with an aligned detector. We expected ≈ 0.05 cm shift in transverse position for a 5 mr misalignment, given the 10 cm half-length of the channel. Studies performed [37] bear this out, and allowed us to assign an error of 0.08% and 0.03% per milliradian in the analyzing powers of channels 6 and 7 respectively. Since the detector was surveyed to better than a few milliradians, we neglected the error due to misalignment.
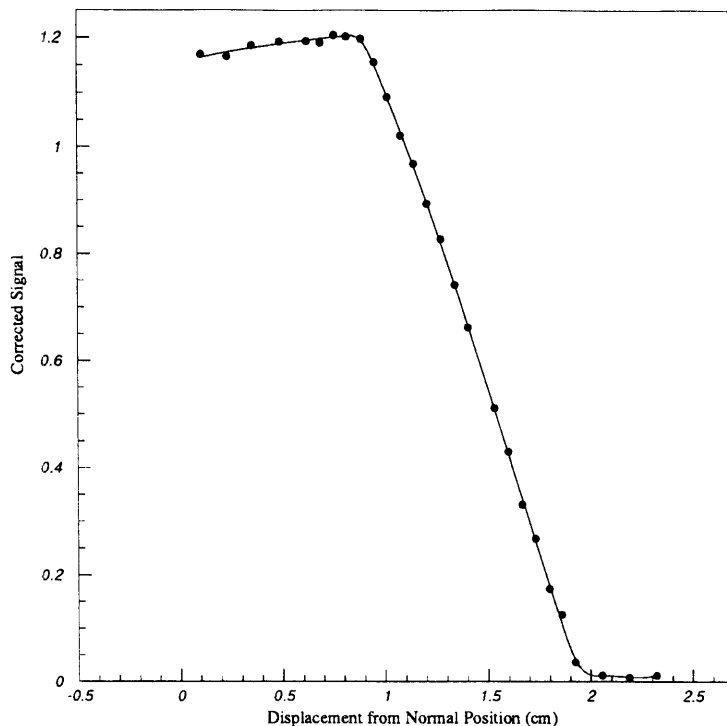
Figure 6-3: An kinematic edge scan with no lead preradiator (taken during the 1992 SLC run). Data (dots) and EGS fit (line) are shown. The sloped region in the center is due to the kinematic edge being swept across the 1 cm width of the channel.

Date	Edge Position (cm)
4/26/93	0.86 ± 0.04
5/02/93	0.84 ± 0.02
7/15/93	0.87 ± 0.02

Table 6.1: Kinematic edge positions as determined from edge scans. Positions are quoted as cm from the edge to the inner wall surface of channel 7.

Monitoring of edge position

The edge scans were a fairly intrusive way to locate the kinematic edge and thereby calibrate the position of the Čerenkov. The location of the zero-asymmetry point also determined the position of the Compton spectrum relative to the Čerenkov without disturbing normal Compton data acquisition.

The zero-asymmetry point fell between channels 2 and 3 of the Čerenkov. The quantity

$$A_0 = \left| \frac{A_2}{A_3 - A_2} \right| \tag{6.3}$$
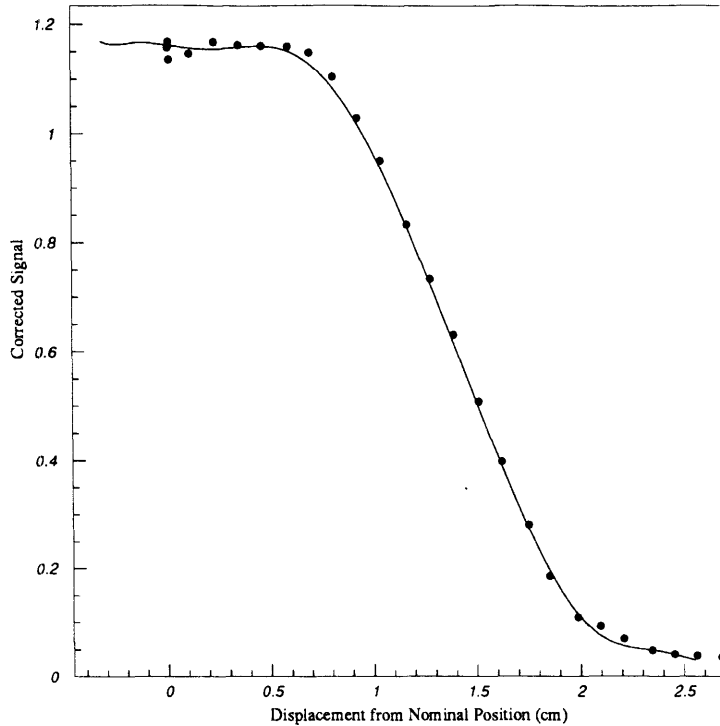
Figure 6-4: An edge scan with 0.8 cm thick lead preradiator in front of the Čerenkov detector. Data (dots) and EGS fit (line) are shown.

where A_2, A_3 are the experimental raw asymmetries as measured by channels 2 and 3 respectively, was monitored to determine the position of the Compton spectrum over the run. In the limit of ideal channel response and negligible cross section and asymmetry function variation, the value of A_0 is the distance of the zero asymmetry point from the center of channel 2 as a fraction of a channel width. Therefore, any change in A_0 corresponded to a change in the position of the electron beam relative to the detector.

Fig. 6-5 shows the behavior of A_0 over the course of the run. We identified three periods of time with different values of A_0, separated by vertical lines in the figure. The edge scans are indicated by arrows. Period I extended from the beginning of the run to July 10. Period II started on July 10 and ended on August 4. Period III started on August 4 and continued to the end of the run.

The shift between periods I and II corresponded to $\approx 300\mu m$ motion in the electron beam position. This was confirmed by the difference in the edge positions as determined by the edge scans taken on May 2 and July 15. The boundary between periods II and III corresponded to the removal of the Pb shield outside channel 1, which changed the asymmetry as measured by the inner channels. Therefore, for period III, the quantity A_0 did not reflect the relative position of the electron beam. For period III, the change in signal height for channel 7 (which contained the

Zero-Asymmetry Point Determination
Detector Position Calibration Stability
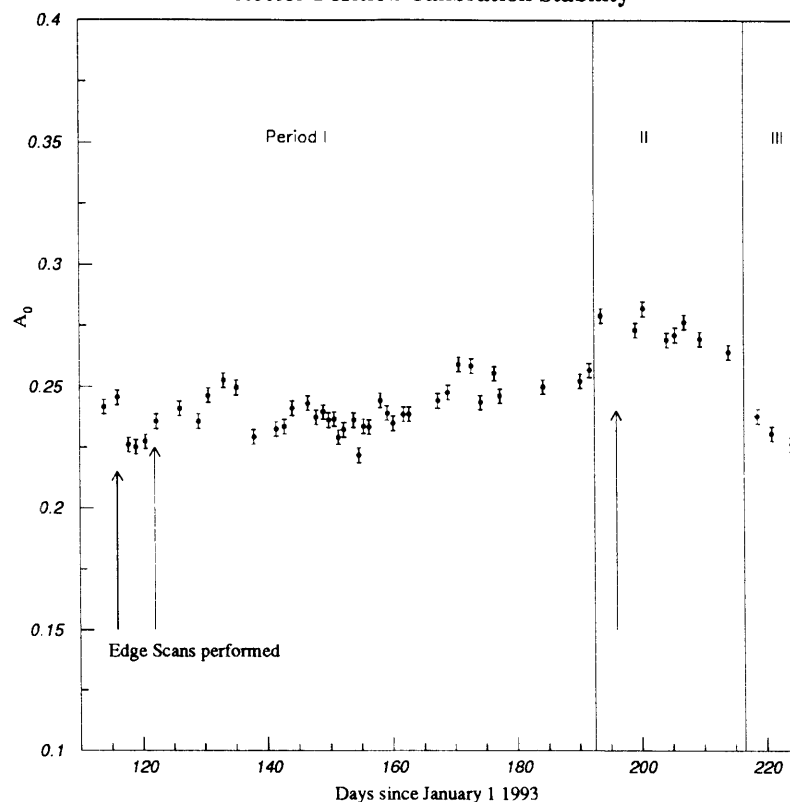
Figure 6-5: The zero-asymmetry-point in Compton scattering, as monitored by the quantity A_0 over the course of the run. Calibration periods I - III, are separated by vertical lines. Arrows indicate edge scans.

kinematic edge) indicated a small ($\approx 100\mu m$) shift in the position of the electron beam.

Fig. 6-6 shows the ratio of Compton signals (laser-on minus laser-off) in channel 6 to channel 7. Since the Compton kinematic edge lay within the acceptance of channel 7, the total signal in channel 7 increased if the beam position (and hence the entire Compton spectrum) shifted towards the Compton detectors. The arrows indicate motion of the electron beam relative to the Compton detector. The first arrow points to the $300\mu m$ shift between periods I and II. The second arrow points to the $100\mu m$ shift between periods II and III. The figure also illustrates the dangers of using the absolute signal, rather than edge scans, as indicators of detector position relative to the beam position. The ratio shows a clear jump at day 192 corresponding to the $300\mu m$ shift, but it also shows a slow rise after that (in period II), until there is another shift corresponding to the $100\mu m$ shift. The slow overall rise of the ratio was due to a known decreasing signal size in channel 7 [23].

The total error in the position calibration, including the uncertainties in the edge scans and tracking the beam position through the measurement of the zero asymmetry point, was estimated

Ratio of Ch 6 : Ch 7
Beam Position Drift Determination

Days since January 1 1993
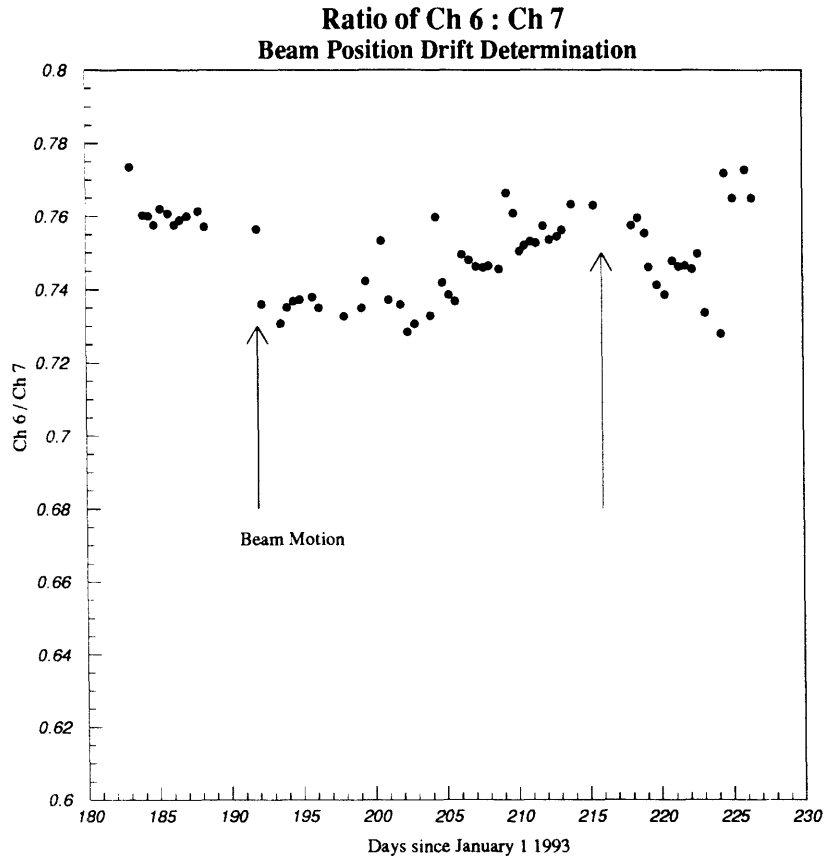
Figure 6-6: The ratio of total signal, Čerenkov channel 6/channel 7. Sharp jumps (arrows) are beam position changes.

at $\pm 250\mu m$, which corresponded to an uncertainty in the polarization determination of $\frac{\delta P}{P} = 0.45\%$ for channel 6 and 0.14% for channel 7. Table 6.2 lists the kinematic edge positions for the three different calibration periods, along with the analyzing powers for Čerenkov channels 6 and 7.

6.3   Bend Strength Fit and Inter-channel Consistency

The Čerenkov detector had nine channels, seven of which were situated within the acceptance required to measure the Compton scattering asymmetry. We used channels 6 and 7 to determine the electron beam polarization, since during most of the run, the inner channels were contaminated by negative asymmetry electrons scattering from the Pb shield.

The Pb shield was removed on 8/4/93. We used data from period III (as defined in Table 6.2) and fit the entire Compton scattered asymmetry for the bend strength of the analyzing magnet, B1. This was compared to the measured bend strength, and provided a valuable cross-check of the

Calibration Period	Position (cm)	a_6	a_7	Notes
I: 4/24 - 7/10	0.84 ± 0.025	0.6151	0.7020	
II: 7/10 - 8/4	0.87 ± 0.025	0.6118	0.7007	Beam position shifts by $300\mu m$
III: 8/4 - 9/1	0.88 ± 0.025	0.6107	0.7003	Pb shield removed

Table 6.2: Edge positions for the three calibration periods, as determined by the edge scans, and monitored by the zero asymmetry point and ratio of signals in Ch. 6 and Ch. 7. The channel analyzing powers (a_6 and a_7) are listed.

B1 bend strength (Mev/c)	Edge Position (cm)	χ^2_{min}	$\frac{\delta P}{P}$	
825.2	0.88 (fixed)	329.7	–	Best fit B1
833.2 (fixed)	0.88 (fixed)	844.1	-0.29%	B1 fixed at nominal
820.2	0.85 (fixed)	334.6	-0.32%	edge moved out 1σ

Table 6.3: Summary of the bend strength fitting.

polarization measurement.

The data set from period III was averaged and compared to the expected asymmetry from the EGS Monte Carlo. The electron-photon polarization product, $P_e P_\gamma$ was allowed to float in the fit, as was the bend strength. The kinematic edge position was fixed at 0.88 cm. Minimizing the χ^2 yielded a bend strength of 825.2 Mev/c, and a χ^2_{min} =329.7. The nominal bend strength was 833.2 Mev/c, and fixing the bend strength at nominal increased the χ^2 to 844.1, but produced only an 0.3% change in the $P_e P_\gamma$ fit. Moving the edge by $300\mu m$ to 0.85 cm also changed the polarization fit by only 0.3%. Table 6.3 tabulates information on the bend strengths.

The bend strength, and thus the beam polarization, was well understood at the level of a few tenths of a percent. In order to determine a systematic uncertainty, we used the best-fit B1 bend strength, and calculated the asymmetry expected in each of the seven Čerenkov channels that see

Channel	Data Asymmetry	Expected Asymmetry	Residual
1	-0.1061 ± 0.0004	-0.1075	-0.0014
2	-0.0227 ± 0.0004	-0.0246	-0.0019
3	0.0801 ± 0.0004	0.0832	0.0031
4	0.1899 ± 0.0004	0.1935	0.0036
5	0.2923 ± 0.0003	0.2887	-0.0036
6	0.3641 ± 0.0003	0.3647	0.0006
7	0.4155 ± 0.0003	0.4158	0.0003

Table 6.4: Čerenkov detector inter-channel consistency.

106

Inter-Channel Consistency Check
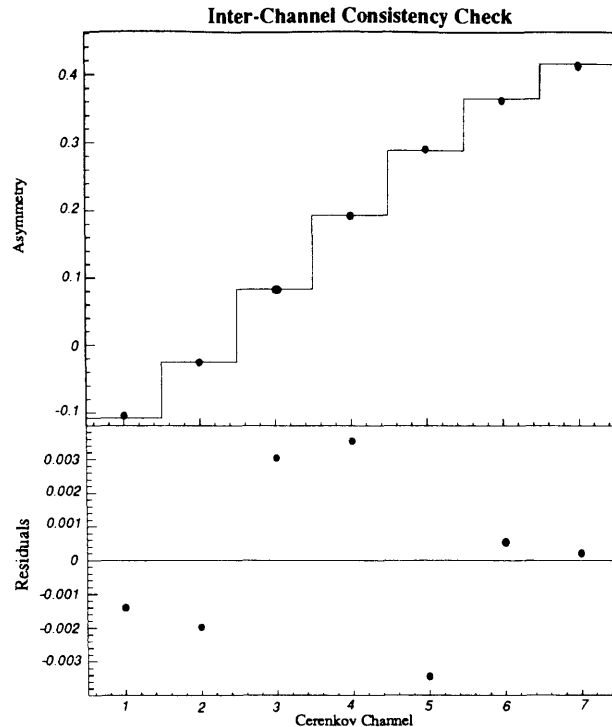
Figure 6-7: The Inter-channel consistency for the Čerenkov detector. Top plot shows the expected asymmetry (line) and data (dots). Bottom plot shows the residuals. The statistical uncertainty on the points is negligible; the scatter is due to small systematic uncertainties, especially in the inner channels.

Compton scattering. We compared this to data (from period III, after the Pb shield was removed), and determined an overall systematic uncertainty (the *Inter-channel consistency*) from the residuals. Table 6.4 and Fig. 6-7 present the data.

The residuals for the inner channels were much larger than the statistical uncertainty, indicating small systematic effects that were not understood. Such effects could include displaced walls and misaligned channels among other such matters. Obviously, if the channel walls were not located exactly where the Monte Carlo simulation assumed they were, the measured asymmetries would have been much different than the expected asymmetries. The acceptance and position of channel 7 was well understood, since the edge scans precisely determined the location of the wall between channels 6 and 7. The wall between channels 7 and 8 was not all that crucial, since the Compton signal kinematic edge fell within the channel 7 acceptance. Channel 6 was similarly well understood. Studies have shown that adjusting the wall locations and dimensions suitably can account for only a third of the scatter in the residuals. Other effects of concern were optical cross-talk, detector misalignment, and photomultiplier tube non-linearities. The inner channels, where most of the scatter lay, were not as well understood as channels 6 and 7, where the kinematic edge provided

Channel	$EA_{0.3}/EA_{0.9}$ DATA	$EA_{0.3}/EA_{0.9}$ SIMULATION
6	1.008± 0.0047	1.007
7	1.008± 0.0045	1.009

Table 6.5: **Ratio of measured asymmetry due to different lead preradiator configurations for data and EGS simulation.**

a powerful calibration tool. The high asymmetry in the Compton scattering signal rendered these outer channels relatively insensitive to various systematic effects.

The root-mean-square of all the residuals was ±0.0026. We assumed this was a reasonable estimate of the systematic uncertainty from detector modelling (although this estimate was overly conservative in the case of channels 6 and 7, the channels of interest in the polarization measurement). We obtained a systematic error of 0.071% and 0.062% from inter-channel consistency for channels 6 and 7 respectively.

6.4 Systematic Uncertainties in Čerenkov Detector Simulation

The EGS4 modelling of the Čerenkov detector and the calculation of the analyzing powers for the channels has already been presented. We performed a few cross-checks to ensure that the detector was well modelled. The lead preradiator produced an amplification in the observed signal in the detector. Different thickness of preradiator yielded different amounts of smearing and amplification. These differences lead to changes in the measured asymmetry, which were studied in a dedicated test, and compared to the changes predicted by the simulation. The difference in the asymmetry measured with 0.3 cm and 0.9 cm of lead preradiator was determined and compared to the prediction. Table 6.5 presents the data as a ratio of the two measured asymmetries. We note that the predicted and measured ratios of asymmetries agree, lending further confidence to the EGS simulations.

6.4.1 Effects of Pb shield

We estimated the effect of the shield on channels 6 and 7 using the EGS4 detector simulation, and adding the Pb shield as region in the simulation. This augmented simulation predicted small relative changes in the analyzing power of the outer channels: −0.2% and < −0.1% for channels 6 and 7 respectively. These corrections were applied to the analyzing powers used for the periods when the

Pb shield was in place. We used the channels outside the Compton kinematic edge to confirm that the Pb shield had a very small effect. If, indeed, there were a large effect on channel 7 from the shield, then the contamination — in the form of a low-asymmetry signal — would have extended out to channel 8. Since channel 8 was beyond the Compton edge, we expected to see a very small signal in this channel, (mostly due to smearing from channel 7). With the Pb shield in place, the ratio of asymmetries in channels 7 and 8 was: $EA_{8/7} = 0.979 \pm 0.010$, while with it removed the ratio was $EA_{8/7} = 0.984 \pm 0.017$. The difference in the asymmetry in channel 8 was less than 1.0%. Since channel the 8 acceptance subtended less than 10% of the high-asymmetry Compton signal that the channel 7 acceptance did, the total low asymmetry signal in channel 8 was less than 0.1% of the high-asymmetry signal in channel 7. The effect of the low-asymmetry contamination from the Pb shield was therefore less than 0.1%, confirming the conclusion of the EGS simulation that the Pb shield had no appreciable effect on channels 6 and 7.

6.5 Electronic Cross-talk and Laser Pickup

Channel-to-channel cross-talk was studied by applying high voltage to only one phototube (energized channel), and looking for any signal in the other eight phototubes that had no high voltage applied (un-energized channels). No un-energized channel was observed to have more than 0.1% of the signal in the energized channel. The complementary study, in which all the channels but one were energized and the lone un-energized channel studied, showed no signal in the un-energized channel greater than 0.5% of the signal present when the channel was energized.

The asymmetry ratio, $EA_{8/7}$, presented in the previous section, was also used to put a limit on the channel-to-channel cross-talk. The observed ratio was $EA_{8/7} = 0.984$, while the expected ratio was $EA_{8/7}^{EGS} = 1.004$. The observed and expected values are within 2% of each other. The overall signal size in channel 8 was $\approx \times 10$ smaller than that in channels 6 or 7, since channel 8 was beyond the Compton kinematic edge. Therefore, if the observed 2% difference in channel 8 asymmetry were entirely due to channel-to-channel cross-talk, it would have corresponded to an 0.2% effect in channels 6 or 7. We took 0.2% as an estimate of systematic uncertainty introduced by channel-to-channel electronic cross-talk.

The Nd:Yag laser used as the light source for the Compton polarimeter was Q-switched — the lasing cavity quality factor was changed by a fast high voltage pulse on a Pockels cell, thereby initiating short pulses of high peak power from the laser. The Q-switch mechanism was seen to have some effect on the Čerenkov electronics, causing a small pickup on the ADC of a few counts. Efforts to eliminate this pick-up were unsuccessful. Since this signal was only present when the laser fired,

it had to be measured and corrected for, since it was not present in the background determined with laser-off pulses.

The electron beam toroids provided a reliable way to identify pulses for which the electron beam was not present, and these toroids were used as vetoes in the Compton summation. We identified $\approx$ 0.1% – 1.0% of the data as empty beam crossings, with no electrons. Typically, this correction was 1 – 2 ADC counts for a signal of around 50 ADC counts. We were able to estimate the laser pickup correction by comparing the laser-on to laser-off signal in the Čerenkov when the electron beam was absent to $\approx \pm$ 0.2 ADC counts for $\approx$ 1 hour intervals, leading to a fractional uncertainty of a few tents of a percent in each one hour period. Since the pickup correction was uncorrelated from period to period, and was measured approximately 3000 times over the entire run, the uncertainty on the pickup correction for the entire 1993 Compton run was much less than 0.01% and was ignored, once correction had been made.

6.6 Summary of Čerenkov detector Systematic Uncertainties

We summarize the major systematic uncertainties for the Čerenkov detector ($\delta \mathcal{P}/\mathcal{P}$):

- Laser Polarization: 1.0%

- Photomultiplier Linearity: 0.6%

- Detector Position Calibration (and EGS simulation): 0.4%

- Electronic Noise and crosstalk: 0.2%

- Inter-channel consistency: 0.5%

For a total of $\delta \mathcal{P}/\mathcal{P} = \delta A_{LR}/A_{LR} = 1.3\%$.

Chapter 7

Chromatic Correction

A small correction had to be made to the polarization as measured by the Compton polarimeter, $\mathcal{P}_e$, to obtain the luminosity-weighted polarization used in the A_{LR} analysis, $\mathcal{P}_e^{lum}$. The main contribution to the difference between $\mathcal{P}_e$ and $\mathcal{P}_e^{lum}$ arose from a low energy tail in the energy distribution of the electron beam. This effect was labelled the *chromatic effect* [42]. The electron beam was not monochromatic, but had an energy distribution, $\mathcal{N}(E)$, characterized by a narrow core ($\Delta E/E < 0.2\%$) and a low-energy tail extending to $\Delta E/E \simeq -1\%$ defined by collimators at the end of the Linac.

The luminosity and beam polarization at the IP also had a dependence on energy given by $\mathcal{L}(E)$ and $\mathcal{P}(E)$. For the 1993 running, the energy dependence of $\mathcal{L}(E)$ resulted from the small vertical spot at the SLC IP which was sensitive to third order chromatic aberrations at the Final Focus. $\mathcal{P}(E)$ had a cosine shape (see Eq. 2.3), determined from the effective number of spin rotations in the North Arc, which depended on the energy of the beam, as discussed in section 2.3.1. Each spin-rotation caused a small loss of polarization, due to the finite energy width of the beam. The effective number of spin-rotations for the on-energy electrons was measured to be 17.9. Off-energy electrons underwent more or fewer spin-rotations than electrons at nominal energy, and thereby had lower polarization. The three distributions, $\mathcal{N}(E)$, and $\mathcal{P}(E)$ are shown in Fig. 7-1, along with the vertical spot size, $\sigma_y(E)$, which determined the luminosity distribution, $\mathcal{L}(E)$.

The Compton polarimeter measured the polarization weighted by the number density,
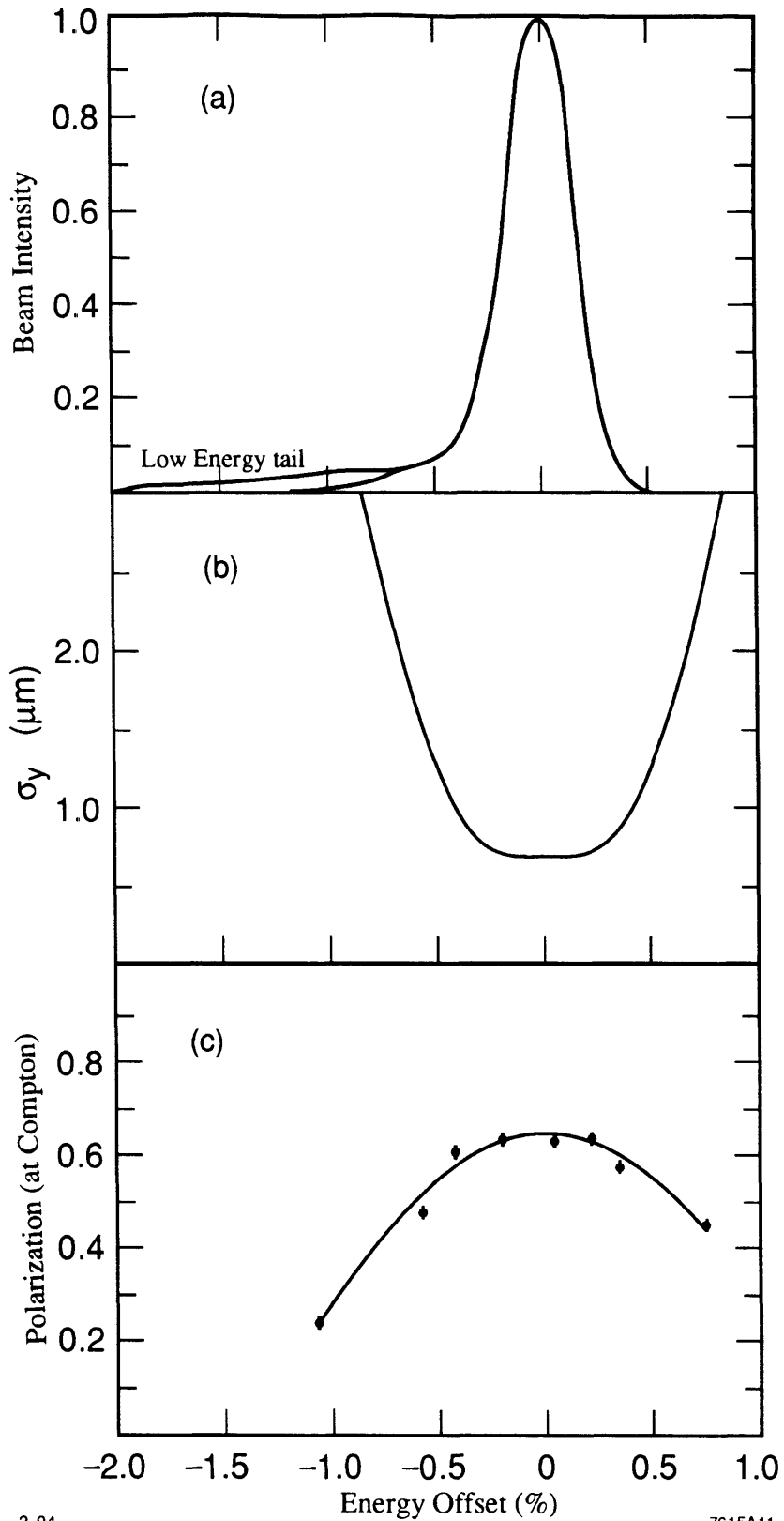
$$\mathcal{P}_e = \frac{\int \mathcal{P}(E) \cdot \mathcal{N}(E)dE}{\int \mathcal{N}(E)dE}, \tag{7.1}$$

Figure 7-1: The distributions for beam energy distribution, $\mathcal{N}(E)$, vertical spot size $\sigma_y(E)$ which determined the luminosity distribution, $\mathcal{L}(E)$, and the polarization distribution, $\mathcal{P}(E)$ as determined from the narrow energy spread beam tests. $\sigma_y(E)$ (and thus $\mathcal{L}(E)$) were determined from calculations, the rest from data.

while the A_{LR} analysis required the polarization weighted by the number density and luminosity,

$$\mathcal{P}_e^{lum} = \frac{\int \mathcal{P}(E) \cdot \mathcal{N}(E) \cdot \mathcal{L}(E)dE}{\int \mathcal{N}(E) \cdot \mathcal{L}(E)dE}. \tag{7.2}$$

These two quantities were related by,

$$\mathcal{P}_e^{lum} \equiv \mathcal{P}_e(1 + \xi), \tag{7.3}$$

which defined the parameter ξ, the chromatic correction.

Off-energy electrons reduce longitudinal polarization at the SLC IP due to spin precession in the arc. They also contributed less to the luminosity than on-energy electrons because they did not focus to a small spot at the SLC IP, while contributing the same as on-energy electrons to the Compton measurement of the beam polarization. Thus, $\mathcal{P}_e^{lum}$ was greater than $\mathcal{P}_e$. However, $\mathcal{P}_e^{lum}$ was constrained to be less than the polarization in the Linac, $\mathcal{P}_e^{linac}$, since no spin precession occurred before the North Arc. Hence,

$$\mathcal{P}_e < \mathcal{P}_e^{lum} < \mathcal{P}_e^{linac}. \tag{7.4}$$

7.1 Measurements and upper limits

We used two separate methods to estimate the effect of the chromatic correction and the associated systematic uncertainty. The first used the measured distributions for $\mathcal{P}(E)$ and $\mathcal{N}(E)$, as well as machine simulation models for $\mathcal{L}(E)$. However, this estimate of the correction was considered too dependent on models of the SLC and was not used.

The second method to estimate the effect depended on data. The upper limit of the chromatic effect was constrained, in a model-independent way, to be $\leq 3.3\%$. The mean of the spread was taken as the magnitude of the effect, and the width as the systematic uncertainty, yielding $\xi = (1.7 \pm 1.1)\%$. The data-driven estimate resulted in significantly larger systematic uncertainty in the chromatic correction than the model-dependent calculation. The mean values of the corrections estimated by the two methods agree quite well. We now present the detail of the data-driven estimate of the chromatic correction.
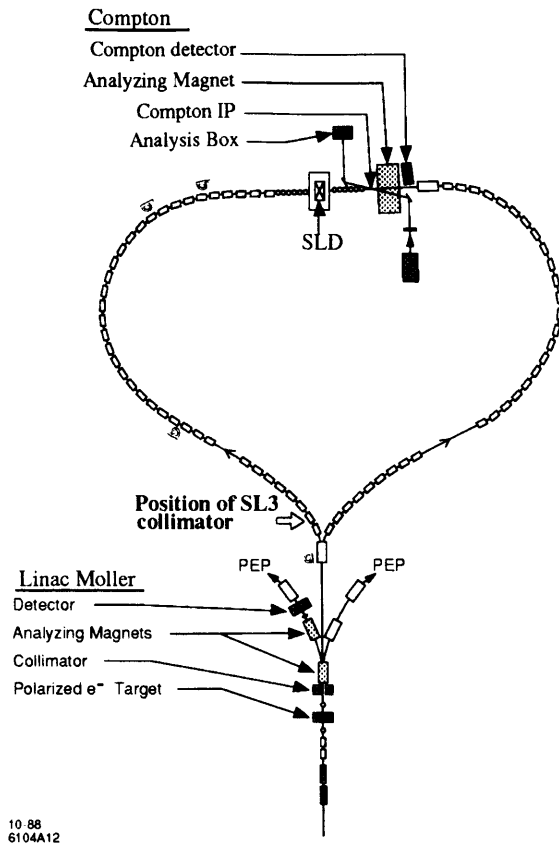
Figure 7-2: The beam switchyard area (BSY), showing the location of the SL3 collimator.

7.1.1 Bound from energy collimator data

Fig. 7-2 shows the location of the SL3 collimator in the SLC. During the 1993 run this collimator had the largest effect of any collimator on the low-energy tail. Fig. 7-3 shows the energy distribution of the electrons, $\mathcal{N}(E)$, as measured by a wire scan at the SLC IP. Part of the low-energy tail, clipped by the low energy jaw of SL3, is visible. At collimator SL3, a -1.5 mm translation of the low energy jaw corresponded to a 1% change in the energy cut.

Moving the SL3 low-energy jaw closer to the beam centroid removed more low energy electrons from the beam, and thereby increased the polarization as measured by the Compton polarimeter. Fig. 7-4 shows the correlation between the distance of the SL3 low-energy jaw from the beam centroid, Δx_{CB}, and the Compton measurement of the beam polarization, $\mathcal{P}_e$. All the 1993 polarimeter data (taken after the source laser wavelength change) are displayed in bins of SL3 jaw position, showing a clear correlation between the position of the collimator jaw and the measured beam polarization. Since the SL3 jaws were continually adjusted throughout the 1993 run, we concluded that the low-energy tail was present during the entire run, and the position of the SL3 low-energy jaw determined the magnitude of this tail and hence the size of the chromatic effect. We performed a linear fit to

111
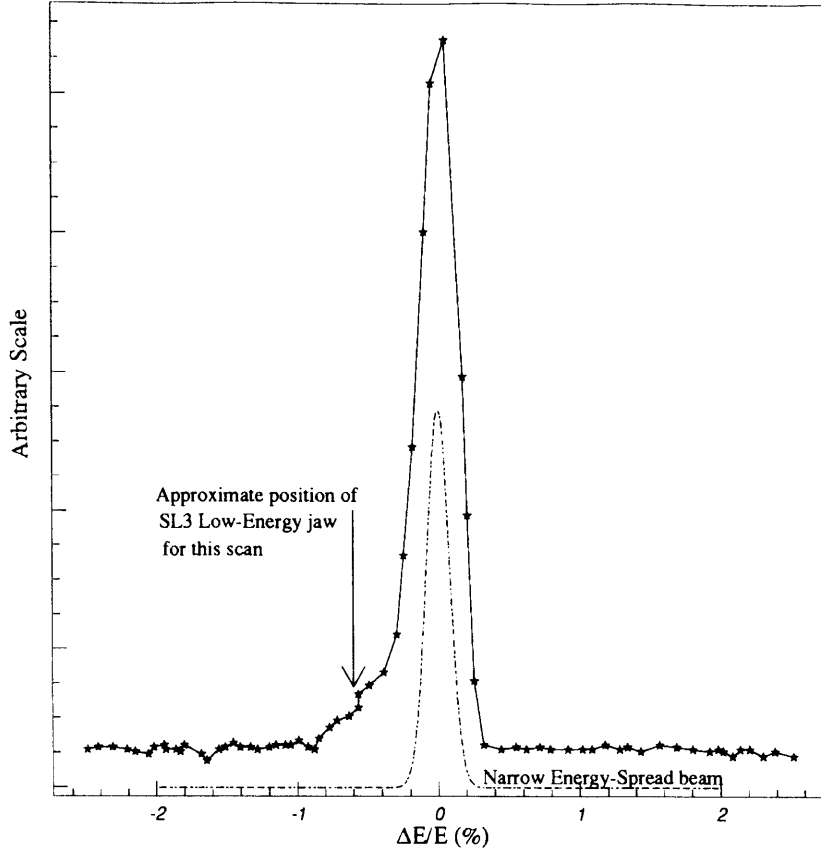
Figure 7-3: Final Focus wirescan data, showing $\mathcal{N}(E)$ (stars), and the position of the SL3 Low-Energy collimator jaw for this scan (arrow); as well as the narrow-energy spread test beam ($< 0.1\%$) distribution, (dashes).

the points in Fig. 7-4, and to be conservative we assumed a slope 1σ steeper than the best-fit slope. This slope is shown in the Fig. 7-4 as a dashed line. Since the polarization at the Linac, $\mathcal{P}_e^{linac}$, did not depend on beam energy, this slope was an upper limit for the dependence of the Linac–Compton polarization difference on the SL3 jaw position.

$$\frac{d(\Delta\mathcal{P}_{\text{LIN.}-\text{Comp}})}{d(\Delta x_{CB})} < 2.7\frac{\%}{\text{mm}} \tag{7.5}$$

Where $\Delta\mathcal{P}_{\text{LIN.}-\text{Comp}}$ was the fractional difference,

$$\Delta\mathcal{P}_{\text{LIN.}-\text{Comp}} \equiv \frac{\mathcal{P}_e^{linac} - \mathcal{P}_e}{\mathcal{P}_e^{linac}} \tag{7.6}$$

To translate the slope into a limit on the difference, $\mathcal{P}_e^{linac} - \mathcal{P}_e$, we obtained the value of this difference at two separate values of Δx_{CB} from the narrow energy-spread beam tests, the results of which are shown in table 7.1. These tests yielded an estimate of $\mathcal{P}_e^{linac}$, since without the low-

SL3 Low Energy Collimator Data

(y-axis: Beam Polarization at Compton; values 0.6, 0.605, 0.61, 0.615, 0.62, 0.625, 0.63)
(x-axis: ΔX_{CB} (mm) + arbitrary offset; values -1, -0.8, -0.6, -0.4, -0.2, 0, 0.2, 0.4, 0.6, 0.8, 1)
$<X_{CB}>_{1993}$
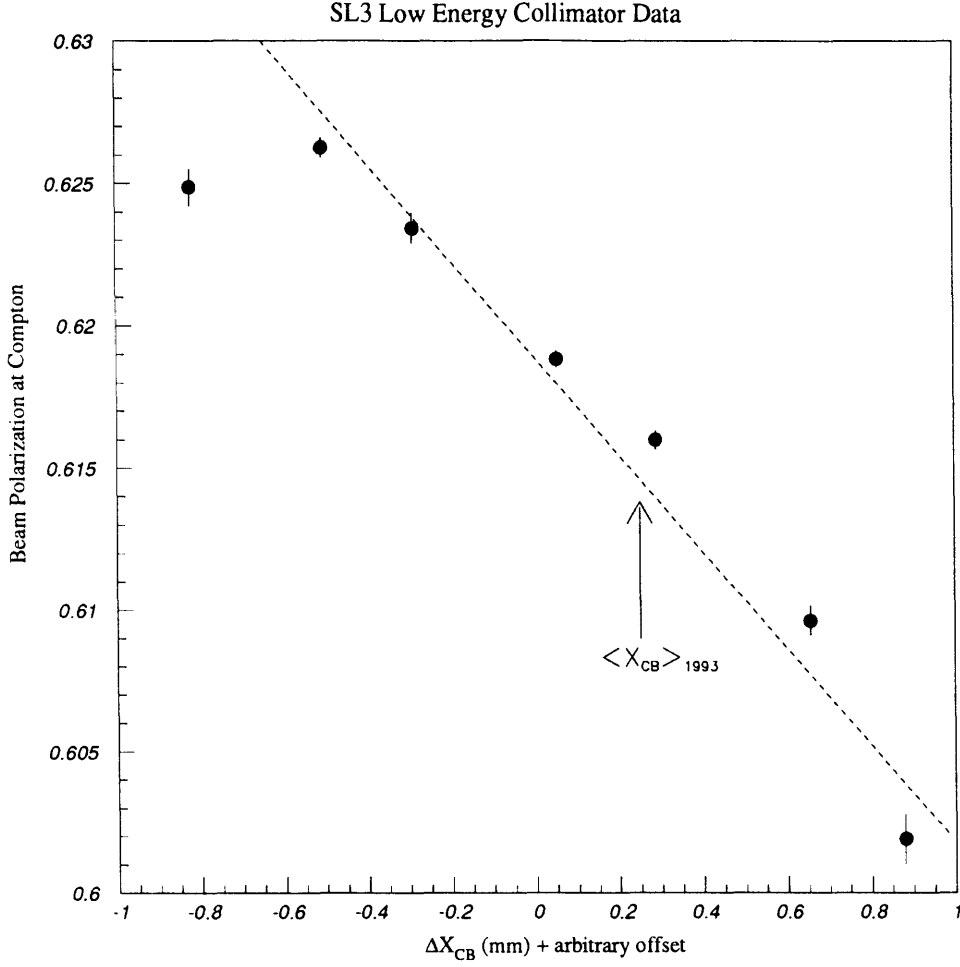
Figure 7-4: Beam polarization measured by the Compton Polarimeter, vs. the SL3L (low energy) jaw position. The arrow indicates the average luminosity weighted position for this collimator for the 1993 SLC run. The dashed line indicates the conservatively steep slope fit to the data.

energy tail, the Linac and Compton polarization were essentially the same, except for a small (0.5%) correction due to spin diffusion and synchrotron radiation. We compared this estimate of $\mathcal{P}_e^{linac}$ with measurements of the Compton polarization $\mathcal{P}_e$, taken just before the narrow energy-spread beams were established. There were two narrow energy-spread beam tests, performed at two different SL3 jaw positions. We used the more accurately measured point at $\Delta x_{CB} = -0.4$ mm and the slope from Eq. 7.5 to obtain the equation for the polarization difference,

$$\Delta \mathcal{P}_{\mathrm{LIN.-Comp.}}(\Delta x_{CB}) < 4.0\% + 2.7 \frac{\%}{\mathrm{mm}} \cdot \Delta x_{CB}. \qquad (7.7)$$

We assumed the (conservative) 1σ upper limit of 2.9% for the polarization difference estimate at $\Delta x_{CB} = -0.4$ mm.

	Δx_{CB} (mm)	$\Delta \mathcal{P}_{\text{LIN.}-\text{Comp.}}$ (%)
July 2,4	-0.4	2.0±0.9
July 15	0.5	5.1 ±2.5

Table 7.1: Narrow energy-spread beam tests and the the fractional difference between the Linac and Compton polarization.

We used Eq. 7.7 and the mean luminosity-weighted value of Δx_{CB} during the 1993 run ($\langle \Delta x_{CB} \rangle = 0.25$ mm) and found the Linac-to-Compton polarization difference to be

$$\Delta \mathcal{P}_{\text{LIN.}-\text{Comp.}}(0.25 \text{ mm}) < 4.7\%. \tag{7.8}$$

7.1.2 Bound from beam energy spread and chromaticity

After having obtained a conservative upper limit on the polarization difference between the Linac and the Compton polarimeter, we estimated the polarization difference between the SLC IP and the Compton, by first estimating a lower limit for the difference between the Linac and the SLC IP. The fractional Linac - IP difference was defined as

$$\Delta \mathcal{P}_{\text{LIN}-\text{IP}} \equiv \frac{\mathcal{P}_{\text{LIN}} - \mathcal{P}_e^{lum}}{\mathcal{P}_{\text{LIN}}}, \tag{7.9}$$

where $\mathcal{P}_e^{lum}$ is the luminosity-weighted polarization at the SLC IP.

Calculation of a lower limit for $\Delta \mathcal{P}_{\text{LIN}-\text{IP}}$ was almost entirely free of modelling uncertainties. since the spatial beam parameters (emittance, divergence) as well as chromaticity, energy profile, and dependence of polarization on beam energy were known. The energy profile, $\mathcal{N}(E)$, was measured using wire scans as mentioned above. The dependence of polarization on energy, $\mathcal{P}(E)$ was measured using the narrow energy-spread test beams.

We determined the dependence of luminosity on energy, $\mathcal{L}(E)$. by using data from that constrained the beam spot size at the SLC IP. As described in section 2.3.2, the 1993 run of the SLD was successful partly due to the use of flat beams. The IP spot size in vertical direction was $0.8\mu m$, while in the horizontal it was $2.6\mu m$. The chromatic aberration was dictated by the dependence of the vertical spot size on energy. Dedicated studies of the beam chromaticity profile were performed by IP wire scans at various electron beam energies. The beam spot size measurements were obtained with round beams, while the calculations were done using the TURTLE beam simulation package [43] assuming flat beams.
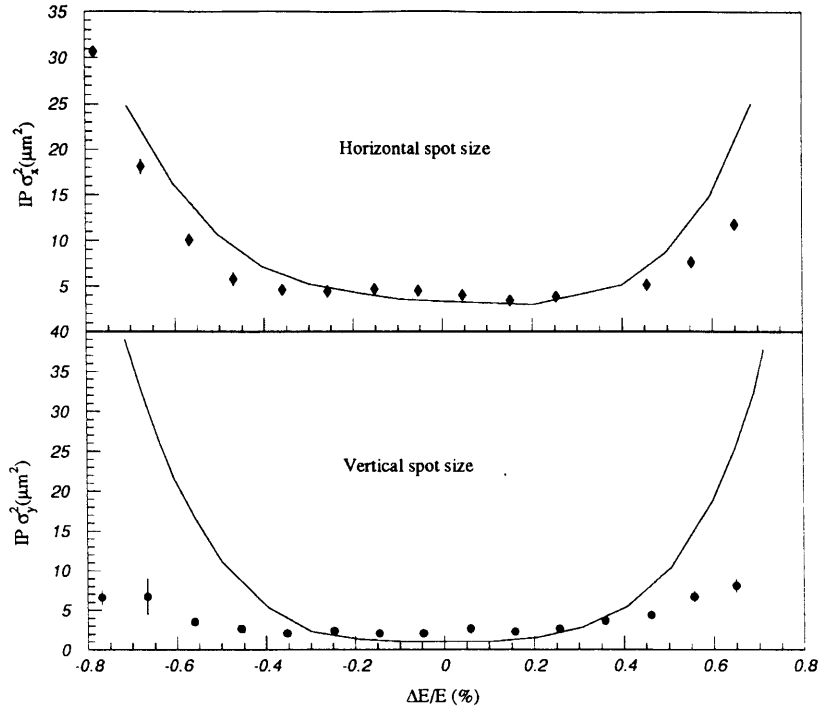
Figure 7-5: Horizontal and vertical beam spot size from data (dots) and calculation (line). The vertical spot size data were taken with round beams, and the calculations indicate the spot size dependence for flat beams.

The vertical and horizontal spot size measurements are shown in Fig. 7-5. The data shown were taken with a diagnostic round beam, the line is from a calculation of the spot size for flat beams. As the figures show, the horizontal spot size (σ_x^2) for flat beams was not significantly different from that for round beams. However, the vertical spot size (σ_y^2) for flat beams was quite different. The spot size at nominal energy for flat beams was $\sigma_x^2 \approx 6.5 \mu m^2, \sigma_y^2 \approx 0.6 \mu m^2$. At a 0.6% deviation from nominal, the spot size was $\sigma_x^2 \approx 10 \mu m^2, \sigma_y^2 \approx 20 \mu m^2$. We observed that σ_y, the vertical spot size, increased rapidly for electrons of off-nominal energy. This tight focusing in the vertical direction created a narrow band-pass in energy, and electrons outside this band did not contribute to the luminosity, since they were not focused to a tight spot at the IP. As Fig. 2-7 shows, these electrons also had lower polarization.

In order to find a lower bound on $\Delta \mathcal{P}_{\text{LIN−IP}}$, and thereby an upper bound on $\Delta \mathcal{P}_{\text{IP−Comp}}$, we chose a conservatively narrow gaussian beam energy profile suggested by the 1993 running experience at the SLC: $\sigma_E > 0.15\%$. We also chose a conservative maximum for the beam chromaticity from the spot size calculations, which yielded the narrowest possible band-pass in energy. Fig. 7-6 shows the vertical spot size, which governed the energy band-pass, overlayed on the beam energy gaussian estimate. It is clear that if either the band-pass or the beam energy spread were made any smaller,
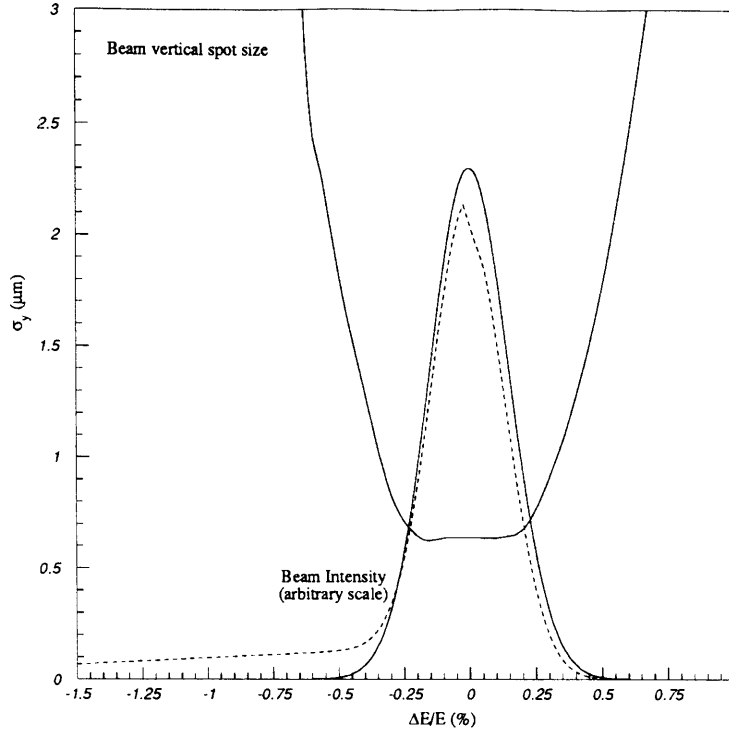
Figure 7-6: Overlay of the vertical spot size dependence on energy (which dictates the energy band-pass for high luminosity), and the beam energy profile for the $\sigma = 0.15\%$ distribution used for the $\Delta\mathcal{P}_{\text{LIN-IP}}$ calculation (line), and nominal beams with tails (dashes).

the value of $\Delta\mathcal{P}_{\text{LIN-IP}}$ would also become smaller, and in the limit that either were made a delta function, $\Delta\mathcal{P}_{\text{LIN-IP}}$ would go to zero. Not including a low-energy tail in the beam energy profile estimate reduced the value of $\Delta\mathcal{P}_{\text{LIN-IP}}$ which was proper for an estimate of the lower bound. Using the conservatively narrow beam energy profile and the conservatively large chromaticity (narrow energy band-pass), and weighting by the measured $\mathcal{P}(E)$ distribution, we obtained

$$\Delta\mathcal{P}_{\text{LIN-IP}} > 1.4\% \tag{7.10}$$

This estimate was largely free of machine and model assumptions.

We used the values in Eq. 7.8 and 7.10, to arrive at the difference between the luminosity weighted beam polarization SLC IP and the Compton polarimeter measurement.

$$\Delta\mathcal{P}_{\text{IP-Comp}} < 3.3\% \tag{7.11}$$

We took the mean of the spread, 0.0% - 3.3%, in Eq. 7.11 as the correction to be applied. We assumed a constant probability distribution in that range, and assigned a systematic uncertainty as

the 1σ value, i.e. $\sigma = 0.34 \cdot 3.3\% = 1.1\%$. The correction to be applied was,

$$\Delta \mathcal{P}_{\text{IP-Comp.}} = (1.7 \pm 1.1)\% = \xi. \tag{7.12}$$

where ξ is the correction parameter introduced in Eq. 7.3.

7.2   Estimate from machine model

We quote the result from a machine-model based calculation of $\Delta \mathcal{P}_{\text{IP-Comp}}$ [44]. This calculation relies on detailed simulation of many components of the SLC, including the Damping Ring beam parameters (the putative cause of the low-energy tail), acceleration and transport, energy collimation, North Arc spin dynamics and Final Focus effects. Data exist to confirm some of the assumptions of the model, but not all. The model predicts a value of $\xi_{model} = (1.9 \pm 0.5)\%$, which is a confirmation of the model-independent calculation presented in the previous section.

7.3   Summary of chromatic correction

To summarize, we present the steps taken to arrive at ξ.

- Polarization loss relation between Linac, SLC IP, and Compton described as $\Delta \mathcal{P}_{\text{IP-Comp.}} < \Delta \mathcal{P}_{\text{LIN-Comp}} - \Delta \mathcal{P}_{\text{LIN-IP}}$.

- SL3 low energy jaw studies and narrow energy spread beam studies put conservative *upper limit*, $\Delta \mathcal{P}_{\text{LIN-Comp.}} < 4.7\%$.

- Beam energy profile, polarization energy dependence, and chromaticity used to put conservative *lower limit*, $\Delta \mathcal{P}_{\text{LIN-IP}} > 1.4\%$

  1. Wire scans at IP suggest conservative gaussian beam profile.

  2. Narrow energy spread beam studies of chromaticity yield conservative estimate of luminosity dependence on energy.

  3. Narrow energy spread test also yields $\mathcal{P}(E)$, polarization dependence on energy.

- Subtracting: $\Delta \mathcal{P}_{\text{LIN-Comp}} - \Delta \mathcal{P}_{\text{LIN-IP}} \rightsquigarrow \Delta \mathcal{P}_{\text{IP-Comp}} < 3.3\%$. Conservative *upper limit* on the chromatic correction.

- Mean and range yield $\xi = (1.7 \pm 1.1)\%$.

Thus, we found $\xi = (1.7 \pm 1.1)\%$. We corrected the Compton measurement of $\mathcal{P}_e$ for this effect, and we found the luminosity-weighted polarization for the 1993 run to be $\mathcal{P}_e^{lum} = (63.0 \pm 1.1)\%$.

Chapter 8

Event Selection for the A_{LR} Data Sample

This chapter presents the Z event selection for the 1993 A_{LR} analysis at the SLD. The event selection used the Liquid Argon Calorimeter (LAC) described in section 3.1.4. The backgrounds in the data sample are identified and estimated.

The main contribution to the backgrounds in the Z event sample was the contamination from final state e^+e^- events, also known as wide-angle Bhabha events (WABs). As discussed in section 1.4, the e^+e^- final state can proceed through either a predominantly Z mediated s channel or a γ mediated t channel. The t channel contribution dilutes the value of A_{LR} for the e^+e^- sample, therefore these events had to be discarded. Other backgrounds for the A_{LR} event sample included the beam-gas, two-photon and cosmic-ray backgrounds. The effects of backgrounds in the A_{LR} data sample was to dilute the asymmetry, since the most backgrounds manifest no left-right asymmetry (e^+e^- backgrounds manifest a small left-right asymmetry).

8.1 The Calibration of the LAC

The response of the Liquid Argon Calorimeter to incident particles has been discussed in references [31] and [45]. In this section we present the various scale factors used to convert raw LAC ADC counts into an estimate of the particle energy.

8.1.1 The minimum-ionizing scale

The minimum-ionizing scale (Min-I or μ scale) was based on the assumption that the incident particle was minimum ionizing, as, for instance, a cosmic ray muon that traversed the entire LAC. The Min-I scale is one of the easiest scales to determine. One accumulates a large data sample of fully traversing cosmic rays using an external cosmic ray trigger, and normalizes the pulse height distribution to that expected for the given materials and geometry [46]. The Min-I scale factors were: 2.28×10^{-3} GeV/ADC-count in the EM sections of the LAC, and 5.99×10^{-3} Gev/ADC-count in the HAD sections. The event selection cuts described in the proceeding section are formulated in the Min-I scale.

8.1.2 The e/π ratio

The Min-I scale is not adequate for an absolute measurement of the energy deposited in the LAC. As described in previous sections, the LAC sampled showers induced in lead plates by collecting the deposited charge. Only a fraction of the total energy was sampled, and this fraction was dependent on the shower type. Electromagnetic showers, induced by incident electrons and photons, are small in both the radial and transverse coordinates. Therefore, the first two radial layers of the LAC (EM) were sufficient to contain electromagnetic showers. There was a slight loss of energy from low momentum particles not sampled by the LAC. Therefore the ratio of the LAC electromagnetic scale to the Min-I scale, e/μ, was less than one.

Hadronic showers, induced by incident protons and pions, are more penetrating and more spread out than electromagnetic ones. The latter two layers of the LAC (HAD) sampled primarily hadronic showers. Hadronic showers tend to lose some fraction of their energy into neutral particles, such as neutrons and neutrinos from pion decay. Some energy is also lost to nuclear binding forces in hadron production. In addition, hadronic showers were not fully contained by the LAC. The energy from hadronic showers that escaped the LAC was measured by the Warm Iron Calorimeter (WIC). However, the WIC response to hadronic showers was not properly understood and data from the WIC was not used in the analysis. The hadronic energy lost to the various effects lead to the ratio of the LAC hadronic scale to the Min-I scale, π/μ to be less than one, and less even than e/μ.

The unequal efficiencies for measuring hadronic and electromagnetic energy meant that the true LAC energy scale depended on e/π, the ratio of the electromagnetic and hadronic energy scales. An extensive analysis of 1992 SLD data [31] established that this ratio was $e/\pi \approx 1.7$. The large difference in the electromagnetic and hadronic response of the LAC means that leaving calorimeter energies in the Min-I scale incorrectly weights the two classes of events. However, for the A_{LR}

analysis, we are not interested in an absolute energy determination. In fact, the main concern in the analysis is the separation of e^+e^- events from the hadronic sample, which is made easier in the Min-I scale.

8.2 Event Selection

The event selection proceeded in three distinct stages. The trigger level, Pass 1, and Pass 2. The events that survived were then associated with polarization measurements made by the Compton polarimeter.

8.2.1 Trigger level cuts

The SLC produced e^+e^- collisions at a rate of 120 Hz. The SLD detector trigger was designed to make a decision and write data to tape from a specific beam-crossing, and did so at an approximate rate of 0.2 Hz.

The trigger decision was the OR of various detector quantities. Of primary concern in the A_{LR} analysis is the ENERGY trigger. This trigger was set by calorimeter information. Other triggers included the TRACK trigger, which used a look-up table to recognize a two-track pattern in the Drift Chamber; the LUM trigger, which was set by the small angle luminosity monitors; and the HADRON trigger, which used a combination of the calorimeter and tracking information. In addition, there were other triggers, including a muon trigger, and a random trigger.

We examine the ENERGY trigger in more detail, since the next level of event selection, Pass 1, tightened the cuts from this trigger. The ENERGY trigger examined several sums of raw ADC data from LAC towers to make the trigger decision. Separate sums were kept of towers that passed *low* thresholds of 8 ADC counts for the EM and 12 ADC counts for the HAD, and *high* thresholds of 60 ADC counts for the EM and 120 ADC counts for the HAD. The sums were labelled as follows:

- **EHI**. The sum of all the energy in the LAC, for towers that passed the high threshold: Had to be > 8 GeV (Min-I) for the ENERGY trigger.

- **ELO**. The sum of all the energy in the LAC, for towers that passed the low threshold.

- **NLO**. The number of towers above the low threshold: Had to be < 1000 towers for the ENERGY trigger.

- **NEMHI**. The number of towers in the LAC EM section above the high threshold.

```
11341,    EVENT    714
MAY-1992 05:01
rce: Run Data    Pol: L
gger: Bhabha
m Crossing           341212
```
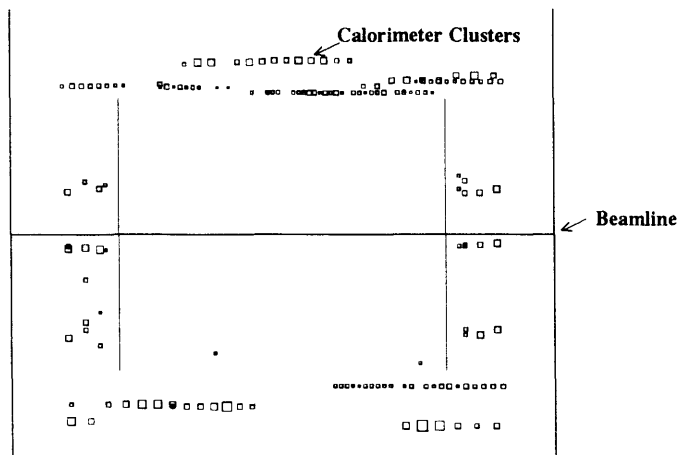
Figure 8-1: SLD Event-display showing beam-parallel muons incident on the LAC. The horizontal line in the middle of the figure is the beam axis. The lines of small squares indicate adjacent groups of LAC towers (calorimeter clusters) traversed by the muons.

SLC induced muons

The ENERGY trigger required the EHI be greater than 8 GeV, with a veto that required that NLO be less than 1000 towers. This veto was intended to reduce the effects of the SLC-muon background. The SLC-muons were beam-parallel muons, created in the accelerator sections upstream of the SLD. Toroids in the SLC final-focus area steered these muons out of the SLD Drift Chamber region. However, these muons still plagued the LAC. Fig. 8-1 shows an event display of the SLD with several beam parallel muons going through the LAC. The small squares indicate groups of calorimeter towers traversed by the beam-parallel muons. These SLC-muons deposited very little energy in any one LAC tower. However, since they tended to penetrate the calorimeter parallel to the beam axis, they deposited energy in several LAC towers. The high threshold of 60 ADC counts in the EM and 120 ADC counts in the HAD section was partly chosen so that towers that would have contributed to the sum due to these SLC-muons would be eliminated. In addition, the requirement that NLO be less than 1000 reduced the trigger-rate due to SLC-muons.

If the ENERGY trigger requirements were satisfied, the entire calorimeter system of the SLD (the LUM, LAC and WIC) were read out, provided they were ready to be read out. During the

1993 run, the SLD recorded approximately three million ENERGY triggers on tape.

8.2.2 Pass 1 cuts

The trigger level cuts described above were designed to reduce the data acquisition rate to a manageable level in a way that would not introduce geometrical biases in the data. The thresholds were kept as low as possible, and the ENERGY trigger decision was made using scalar sums only. Therefore, the trigger accepted many events that were not Z events. The bulk of these were beam-gas or beam-wall events. Such events were caused by one of the beams interacting with either residual gas in the beampipe or some accelerator section and creating a shower of particles in the SLD.

The Pass 1 cuts were designed to eliminate a large fraction of these background events, while maintaining the unbiased nature of the ENERGY trigger. For that reason, only ADC sums were used in making the Pass 1 cuts. The quantities used in the trigger were tightened. The Pass 1 cuts were as follows:

- EHI > 15 GeV (Min-I scale)

- NEMHI $\geq$ 10 towers

- ELO < 140 GeV

- ELO < $\frac{2}{3}$ EHI + 70 GeV

The first and second cuts were similar to the trigger requirements. The EHI requirement was for 15 GeV, rather than 8 GeV for the trigger. The second cut, on the number of EM towers over the high threshold, also helped eliminate beam parallel muons that deposited energy predominantly in the HAD sections of the LAC.

The third and fourth cuts, on the ELO variable, insured that the event had not satisfied the previous two requirements by depositing a large amount of background energy. Background events scattered energy in many towers, most of which were below the high threshold. Even for those background events that passed the EHI cut, the majority of the energy was in several low energy towers. After the Pass 1 cuts were applied, 63552 events remained in the sample. Both the trigger and Pass 1 cuts operated on "raw" calorimeter data — the ADC counts from the various LAC towers.

8.2.3 Reconstruction and Pass 2 cuts

Before the Pass 2 cuts could be applied, the raw calorimeter data underwent *reconstruction*: grouping the calorimeter towers, and calculating several quantities of interest such as the thrust, the thrust axis, the total energy, and the energy imbalance of the event.

All LAC towers were subject to a reconstruction threshold of 7 ADC counts for the EM and 9 ADC counts for the HAD sections. Towers closest to the beampipe (the so called *wall of fire*) were ignored. The SLD calorimeter reconstruction constructed groups of contiguous calorimeter towers that passed the reconstruction thresholds. These groups were called *clusters*.

The reconstruction proceeded in two stages. During the first stage, spatially contiguous towers were combined into clusters. These clusters were called coarse clusters. During the second stage, the course clusters were refined by routines that looked for minima in the spatial distribution of energy deposition in the cluster, and separated the cluster into two or more clusters if it appeared the profile was due to more than one incident particle. These separated cluster were called refined clusters. The Pass 2 cuts operated on quantities based on refined clusters.

Good clusters were defined as follows:

- Total energy in the cluster > 100 MeV

- Total electromagnetic energy $\neq$ 0 MeV

- The cluster was not identified as an SLC induced beam parallel muon.

The third item, the identification of clusters as SLC induced muons, was performed by a pattern-recognition method [47]. Clusters of LAC tower hits induced by SLC induced muons were characterized by low energy deposition in any individual tower and extremely small spread in the azimuthal and large spread in the polar angle. These characteristics were used to recognize and reject SLC muon induced clusters with great efficiency.

The Pass 2 cuts operated on the following quantities:

- **Total Energy.** The sum of the energy in all good clusters (min-I scale).

- **Energy Imbalance.** The vector sum normalized by the scalar sum of the energy deposited.

- **Number of Clusters.** The number of good clusters found by the reconstruction.
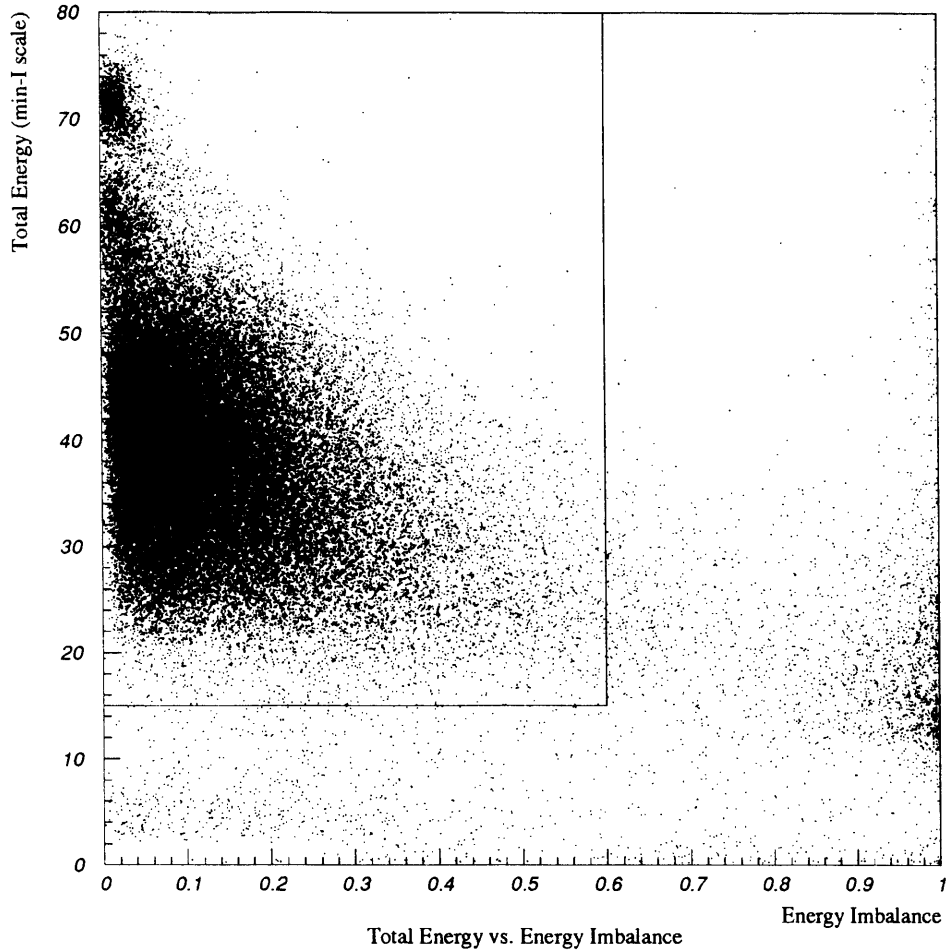
Figure 8-2: Total Energy in the LAC (Min-I scale) vs. energy imbalance. The lines indicate the Pass 2 cuts for energy and imbalance.

The energy imbalance was defined as

$$\text{Imbal} = \frac{|\sum E_i \vec{r}_i|}{\sum E_i} \tag{8.1}$$

where the sums are over all good clusters, and $\vec{r}_i$ is the unit radial vector with origin at the IP, in the direction of the cluster. Events with large energy deposition in one section of the detector (such as beam-wall events) tended to have large values of imbalance, while Z decays, which were symmetric about the interaction point, tended to have small values of imbalance.

The first part of the Pass 2 cuts operated on the total energy and energy imbalance variables. The total energy was required to be greater that 15 GeV (in the Min-I scale) and the imbalance was
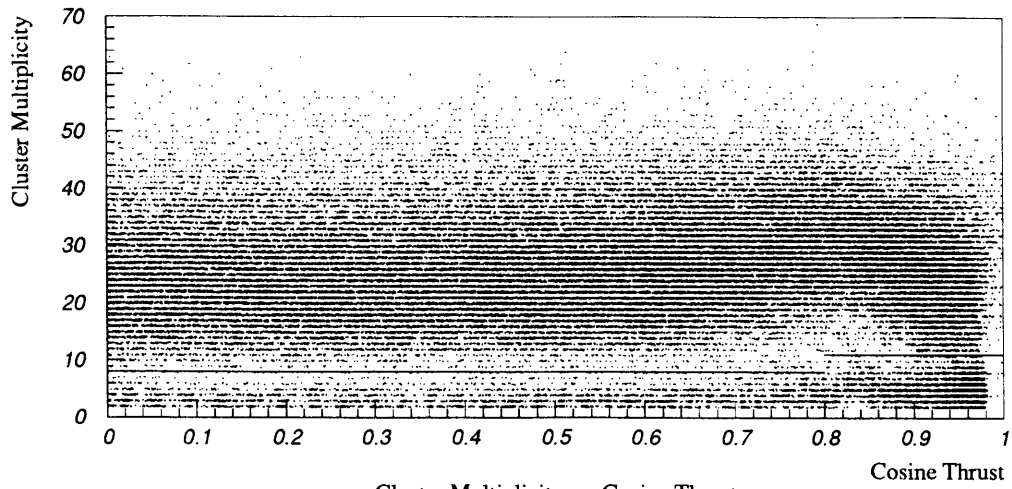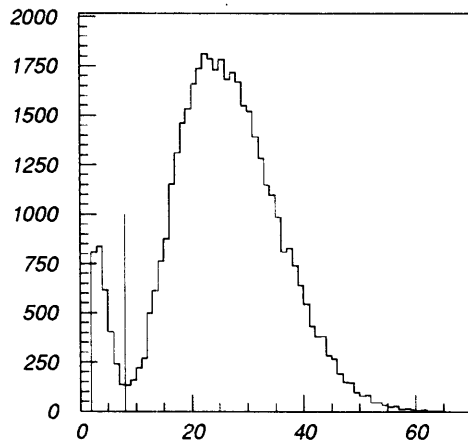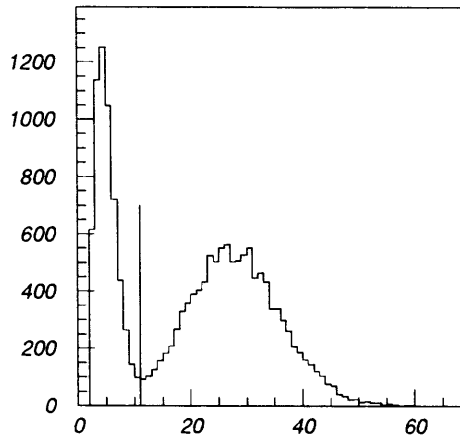
Figure 8-3: Cluster Multiplicity distribution for data that passed the total energy and energy imbalance Pass 2 cuts, versus $\cos\theta$ (top), and separately for the central and forward parts of SLD (bottom). The lines indicate the Pass 2 cluster multiplicity cuts.

required to be less than or equal to 0.6. Fig. 8-2 shows a scatter plot of the total energy and energy imbalance for all the reconstructed events. The lines indicate the cuts. A large class of background events with low energy is eliminated, as is an even larger class of background events with large imbalance.

The second part of the Pass 2 cuts operated on the number of clusters. This cut was designed to eliminate the e^+e^- final state. The e^+e^- events produced a smaller number of clusters than the hadronic events since electromagnetic showers produced by e^+e^- events are less spread out than the

hadronic showers produced by $q\bar{q}$ final states.

Fig. 8-3 (upper plot) shows the number of clusters for the events that passed the total energy and energy imbalance cuts already described. The number of clusters are plotted versus $\cos\theta$, the polar angle of the thrust axis of the event. The thrust and thrust axis are defined as follows [48]:

$$T = \max\left[\frac{\sum_i |\vec{p_i} \cdot \vec{n}|}{\sum_i |\vec{p_i}|}\right] \qquad (8.2)$$

where T is the thrust, $\vec{p_i}$ are the momentum vectors of the particles in the event, and $\vec{n}$, the thrust axis, is a unit vector chosen to maximize the numerator. The sum is over all particles in the event. In the calorimeter-only analysis, the sum is taken over all clusters and $\vec{p_i}$ is derived from the observed energy in a given cluster and its position relative to the IP. There were small uncertainties in the calculations of the thrust and the thrust axis due to the coarse spatial resolution of the LAC and the difficulties inherent in assigning momentum based on a calorimetric measurement. Analyses that required precise knowledge of the thrust used the Drift Chamber for a precise measurement of $\vec{p_i}$. The uncertainty incurred in calculating the thrust axis by not requiring Drift Chamber information has been shown to be small for this analysis [31].

The SLD Barrel LAC had significantly better resolution than did the endcap LAC. The poorer resolution in the endcaps was due to extra material in the path to the endcaps, which caused multiple scattering and broadening of shower widths. Some of this difference was accounted for in detector simulations [49], but some of it remains to be understood. Due to this difference in the endcaps, we defined two separate parts of the detector, based on polar angle θ. The *central* part was defined as $|\cos\theta| < 0.8$, and the *forward* part as $|\cos\theta| \geq 0.8$. The forward part suffered due to poorer energy resolution in the endcaps.

In the central part, we required ≥ 9 clusters in the reconstructed calorimeter. In the forward part, we required ≥ 12 clusters. Fig. 8-3 (lower plots) show the cluster multiplicity (NCLUS) distribution for the central and forward parts. There is a peak at small cluster multiplicity in both parts corresponding to e^+e^- final state events. In both cases, the cuts, indicated by the lines, clearly separate the hadronic events from the e^+e^- events.

A total of 50707 events survive the entire process including the Pass 2 cuts. These events are almost entirely hadronic Z decay events. There are a few $\tau^+\tau^-$ events in the sample. Since the event selection is based entirely on calorimeter data, it contains no $\mu^+\mu^-$ events, since muons deposit very little energy in the calorimeter. However, since $\tau^+\tau^-$ and $\mu^+\mu^-$ lepton events are expected to manifest the same value of A_{LR} as hadronic events, we do not consider them backgrounds for this analysis.

The e^+e^- events are the main source of background events. We now estimate this and other backgrounds in our sample.

8.3 e^+e^- Background Estimates

The effect of background on the A_{LR} analysis seems obvious enough. Most background events have no left-right asymmetry, so they tend to dilute the asymmetry for the Z events. The correction for this *zero asymmetry* background is straightforward. However, as mentioned in the previous sections, the largest contribution to the background was from e^+e^- events. These events manifested a left-right asymmetry different from A_{LR}. This asymmetry depended on polar angle, and a measurement of this dependence constituted a test of the Standard Electroweak Model independent of A_{LR}. [50]. Therefore, the correction to A_{LR} due to backgrounds depended on what fraction of these background events had zero asymmetry, and what fraction had finite asymmetry. This correction is developed in detail in the section 8.7.

The background determination for an event sample isolated by the various cuts described above is usually performed using a detector simulation Monte Carlo. All expected types of events, including background events, are generated and the detector response simulated. The various cuts are then applied, and their efficiency for eliminating the unwanted events while retaining the desired events estimated.

8.3.1 The SLD detector simulation

The SLD detector was simulated using the GEANT [51] simulation package. The various detector elements were grouped into geometrical subsections and the properties of their material tabulated. The GEANT simulation package then tracked simulated events through the various detector elements and produced the appropriate response signals.

The LAC simulation included elements such as the liquid argon cryostat and the washers used in the construction and assembly. However, proper simulation of the LAC response required including in the simulation all the material in front of the LAC, since this material caused broadening of shower widths due to premature scattering. However, incomplete knowledge of intervening material caused shortcomings in the simulated response, especially in the endcap sections of the LAC.

The main problem with GEANT was its inability to simulate the cluster multiplicity distribution. Fig. 8-4 compares the cluster multiplicity distributions from hadronic and e^+e^- event simulation to
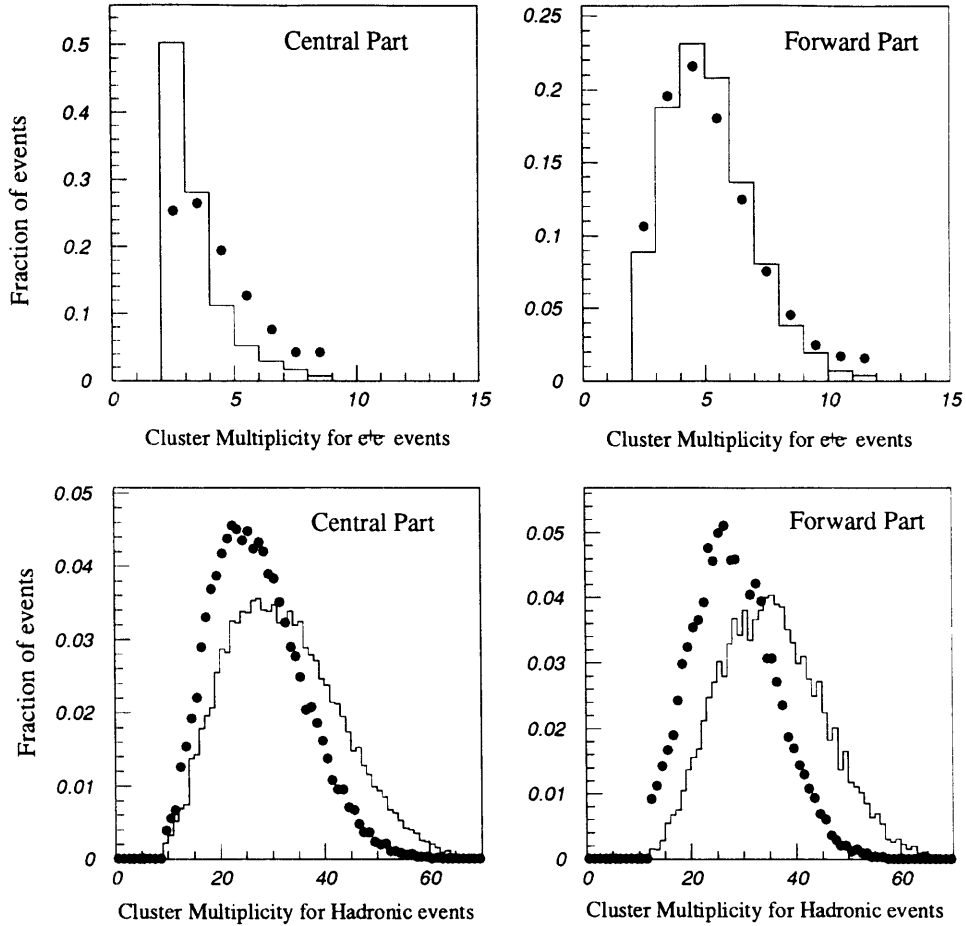
Figure 8-4: Cluster multiplicity distributions for simulated events (line) and data (dots). Data is shown separately for e^+e^- (top) and hadronic events (bottom), for the central (left) and forward (right) SLD. The agreement in all cases is poor.

hadronic and e^+e^- data. The agreement is poor. As described above, the LAC signals were subject to a reconstruction threshold, after which surviving towers were grouped into coarse clusters. These clusters were then refined — a given coarse cluster broken up into multiple clusters if the energy distribution in the cluster had minima that indicated multiple incident particles. However, the GEANT did not reproduce the refined cluster multiplicity well . Therefore, to estimate backgrounds, we constructed some event variables that could be better modelled by the simulation. We carried out two separate analysis, labelled Method I and II. These two methods concentrated on determining the e^+e^- background. The other backgrounds, to be discussed later, were more easily estimated from the data itself.

Cluster Multiplicity Fit for CENTRAL SLD

χ^2/ndf	156.5	/	55	
P1		826.9 ±		19.70
P2		3.026 ±		0.1174
P3		1.909 ±		0.8210E-01
P4		1115. ±		55.37
P5		30.07 ±		0.4255
P6		8.926 ±		0.1231
P7		1069. ±		70.79
P8		21.60 ±		0.1971
P9		5.594 ±		0.1768
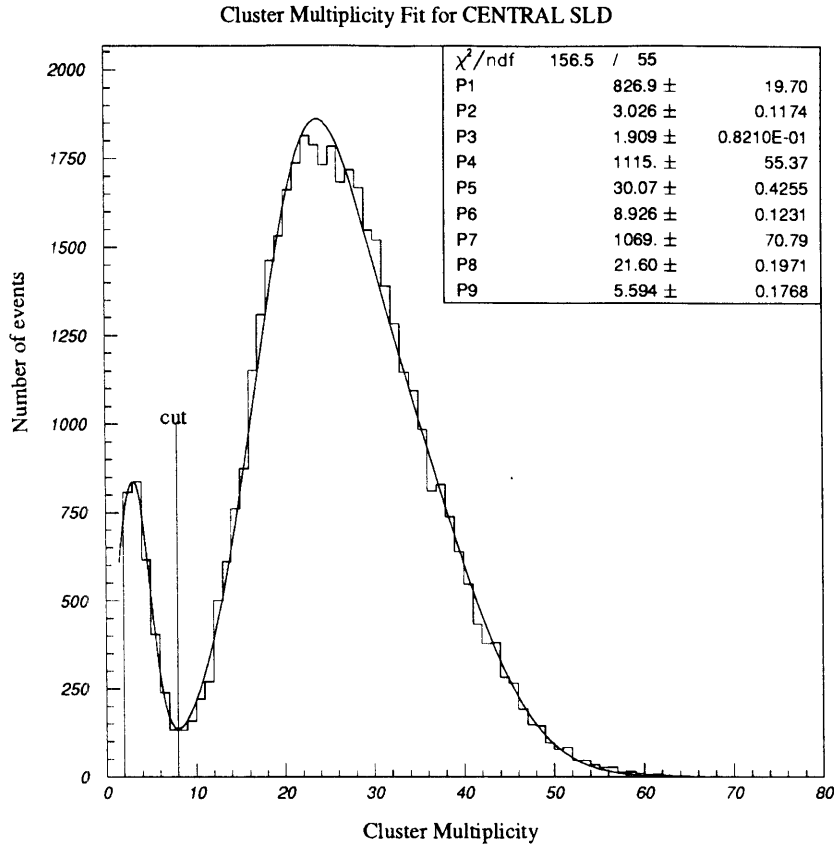
Figure 8-5: Cluster multiplicity distribution for the central part of SLD, with a three gaussian fit. The leftmost gaussian is due to e^+e^- events. The line indicates the cluster multiplicity cut.

8.3.2 e^+e^- Background estimate from data

The final limits on the e^+e^- background were estimated by methods that made extensive use of the SLD detector simulation. However, a purely data driven estimate of the e^+e^- background was also performed. We fit the data in the cluster multiplicity histograms shown in Fig. 8-3 to gaussian distributions, with the assumption that the peak at low cluster multiplicity was due to e^+e^- events. Fig. 8-5 shows the fit of the cluster multiplicity distribution to three gaussians for the data from the central part of the SLD, while Fig. 8-6 show the fit to two gaussians for the data from the forward part of the SLD. The fit parameters listed translate as follows [P1-P3] are amplitude, mean and σ for the first gaussian (at low multiplicity), [P4-P6] for the second and [P7-P9] for the third (in the case of the three gaussian fit for the central part of SLD). The line at cluster multiplicity = 8 (11) is the Pass 2 cut for the central (forward) part of the detector.

For each of the fits, we took the first gaussian at low cluster multiplicity, and extrapolated its tail into the region beyond the cluster multiplicity cut, taking the 1σ upper limits for all fit quantities. We

Cluster Multiplicity for FORWARD SLD

χ^2/ndf	97.85	/	53	
P1		1173. ±		21.68
P2		4.604 ±		0.3889E-01
P3		2.022 ±		0.4027E-01
P4		531.3 ±		6.513
P5		27.51 ±		0.8764E-01
P6		8.530 ±		0.7463E-01
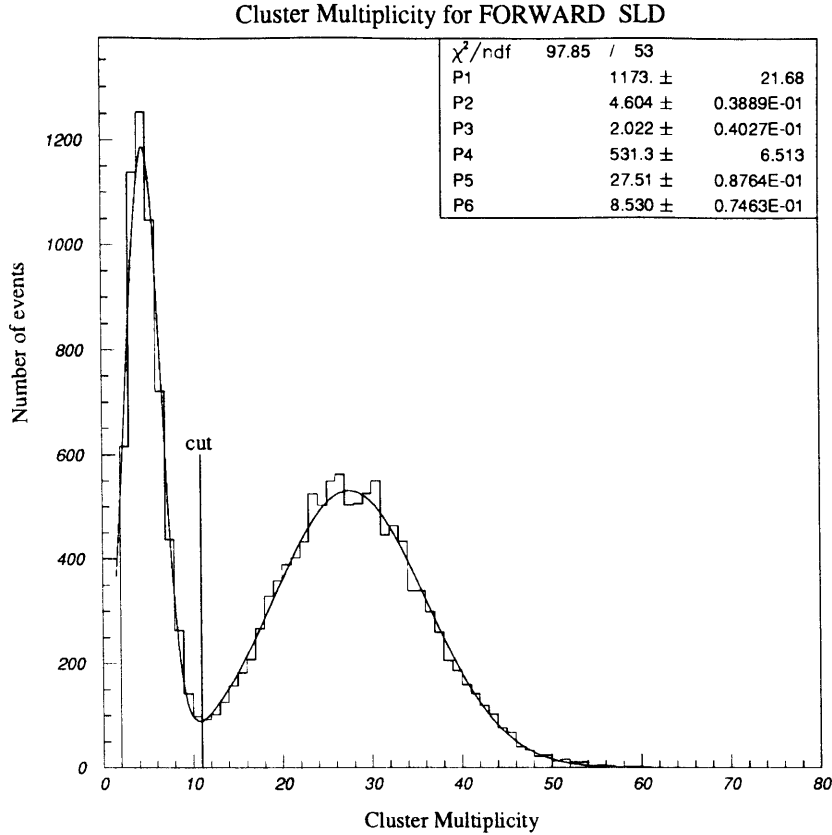
Figure 8-6: Cluster multiplicity for the forward part of SLD, with a two gaussian fit. The leftmost gaussian is due to e^+e^- events. The line indicates the cluster multiplicity cut.

estimated $N^{cent}_{e^+e^-} = 32$ e^+e^- events in the central part of the detector, and $N^{forw}_{e^+e^-} = 6.5$ e^+e^- events in the forward part. The data-based estimate of the e^+e^- background was thus $f^{data-only}_{e^+e^-} \approx 0.08\%$.

There were too many unknown factors in this data-based analysis for us to use this estimate as anything other than a guide for the numbers obtained from the Monte Carlo estimates. The cluster multiplicity distribution for e^+e^- data was almost certainly not a gaussian. As noted in the previous section, extraneous material in front of the LAC could have caused a large non-gaussian tail extending out to large cluster multiplicities for e^+e^- events.

8.3.3 e^+e^- Background analysis Method I

This method used the known energy deposition characteristics of e^+e^- events to construct quantities that can select these events over hadronic decays. Final state e^+e^- events tended to deposit almost all their energy in a small number of towers in the EM section of the LAC. Hadronic decays, in contrast, deposited energy over a larger number of towers, significant numbers of which were in the

HAD section of the LAC.

Due to the large e/π ratio of the LAC ($\approx$ 1.7), events depositing mainly electromagnetic energy, such as e^+e^- events, seemed to be separated from events depositing mainly hadronic energy. Fig 8-2, a scatter plot total energy vs. energy imbalance of all the Pass 1 data, illustrates this separation. The events with energy imbalance below 0.6 and total (Min-I) energy above 15 Gev formed two clusters in energy. The cluster around 70 Gev consisted of e^+e^- events (subsequently removed by the cluster multiplicity cuts), while the broader cluster around 40 GeV consisted of hadronic events. On a properly calibrated energy scale, the two clusters would have lain on top of each other and been indistinguishable. We used this ability of the Min-I energy scale to separate electromagnetic from hadronic events to create e^+e^- selection criteria that did not depend on the cluster multiplicity distributions.

We created two variables to isolate e^+e^- events:

- **EHTOT**. The sum of the energy in the HAD section of the LAC.

- **EEMHI1 + EEMHI2**. The sum of the energy in the two highest energy clusters in the EM section of the LAC.

Fig. 8-7 shows the scatter-plot of the two variables. The data plotted has passed the Pass 2 cuts for energy and imbalance, but not the cluster multiplicity cuts. The data is a combination of hadronic and e^+e^- decays of the Z.

The plots show two distinct groupings of data, both in the central and forward parts of the detector. The data in region A had little or no hadronic energy (EHTOT was small), and significant amount of energy concentrated in the two largest EM clusters. (EEMHI1 + EEMHI2 was large). These events were predominantly e^+e^- events. The data in region B had significant hadronic energy. These events were predominantly hadronic decays.

For the plot containing data from the central part of SLD, regions A and B were defined as follows:

$$A_{\text{central}} = (\text{EEMHI1} + \text{EEMHI2}) > (40 + 8 \cdot \text{EHTOT})$$
$$B_{\text{central}} = (\text{EEMHI1} + \text{EEMHI2}) < (40 + 8 \cdot \text{EHTOT})$$

(8.3)

while for plot containing data from the forward part, regions A and B were

$$A_{\text{forward}} = (\text{EEMHI1} + \text{EEMHI2}) > (20 + 13.33 \cdot \text{EHTOT})$$
$$B_{\text{forward}} = (\text{EEMHI1} + \text{EEMHI2}) < (20 + 13.33 \cdot \text{EHTOT})$$

(8.4)
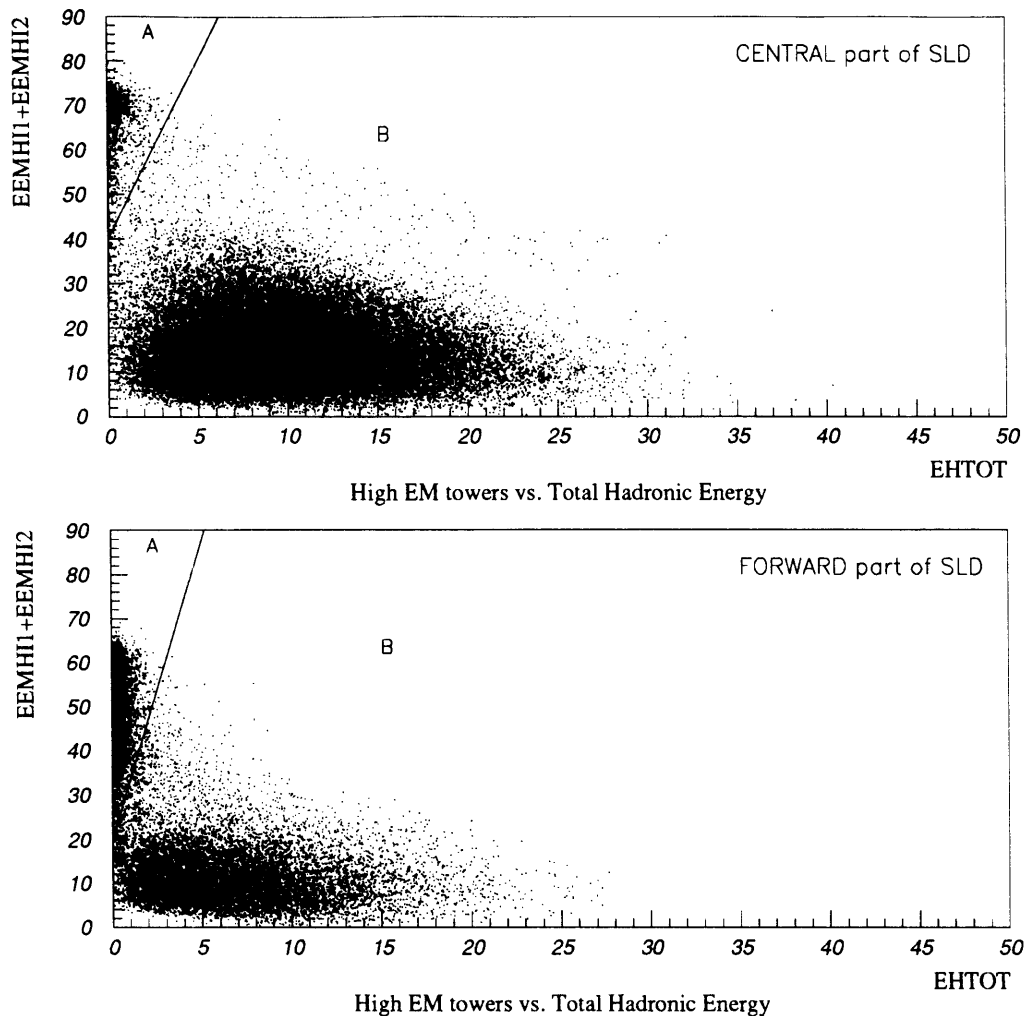
Figure 8-7: Scatter plots of the Method I variables, EEMHI1+EEMHI2, and EHTOT. Region A is e^+e^- rich data, region B is hadronic data.

Event simulation

Both final state e^+e^- and hadronic events were simulated [52]. The simulations produced "raw" detector data. For the LAC, this data was in the form of simulated ADC counts for various LAC towers. The simulated data was then reconstructed in the same manner as the real data. These simulated and reconstructed events were then passed through the Pass 2 energy and imbalance cuts described above. The cluster multiplicity distributions were significantly different from the data, as illustrated in fig. 8-4. However, the energy depositions in both the EM and HAD sections of the LAC were well simulated. If we believe that the reason for the cluster multiplicity mismatch between

Data and Monte Carlo simulations of e^+e^- events for Method I.

Two higest EM Clusters (EEMHI1+EEMHI1)

Total Hadronic Energy (EHTOT)
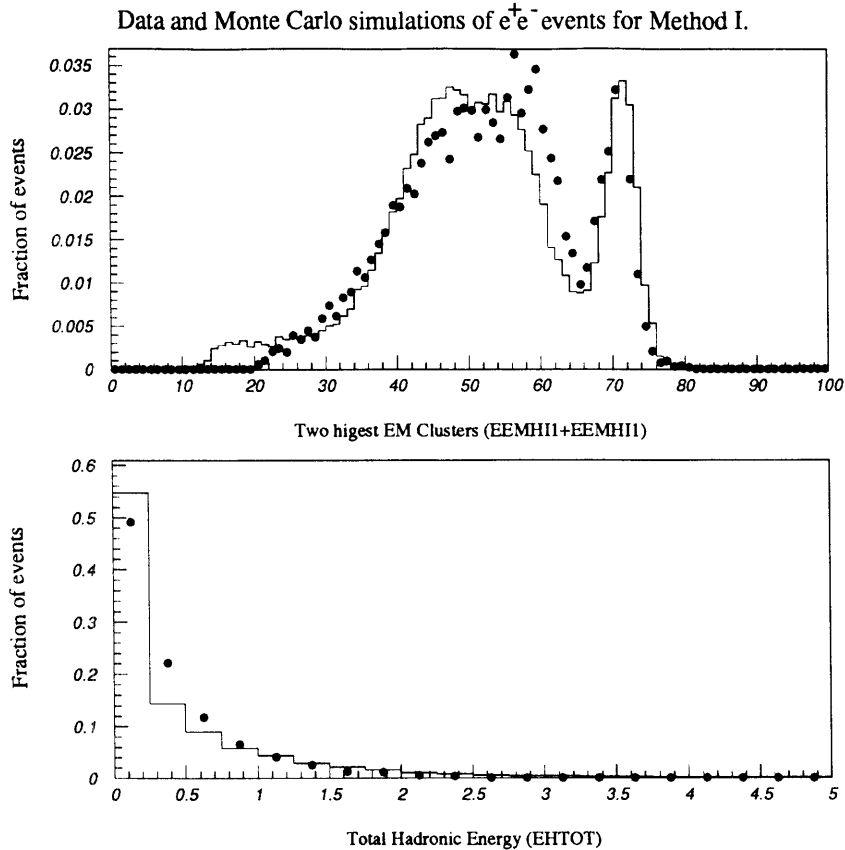
Figure 8-8: Comparison of the Method I variables EEMHI1+EEMHI2 and EHTOT for e^+e^- rich data (dots) and e^+e^- simulation (line).

simulations and data was the inability to properly model energy shower characteristics at very lowest energies, then we expect that the simulations should match the total energy deposition reasonably well, since total energy deposition did not depend heavily on low-energy shower characteristics.

The distributions for the two Method I variables constructed above, EHTOT and EEMHI1+EEMHI2, were well matched between data and the two Monte Carlo data sets. Fig. 8-8 shows the qualitative agreement between data and the e^+e^- Monte Carlo for the two variables, in both the forward and central parts of the detector. The hadronic Monte Carlo distribution, shown in Fig. 8-9 had to be scaled by a small amount to match the data.

The cluster multiplicity cuts described in the previous section were then applied to the simulated events. Fig. 8-7 shows the scatter plots for data that survived the energy and imbalance cuts for Pass 2 (the cluster multiplicity cuts have not been applied to the data shown). The central and forward parts of the detector are plotted separately and the regions A and B shown.

The results for both the e^+e^- and hadronic final states, in regions A and B for the forward and

Data and Monte Carlo simulations of hadronic events for Method I.
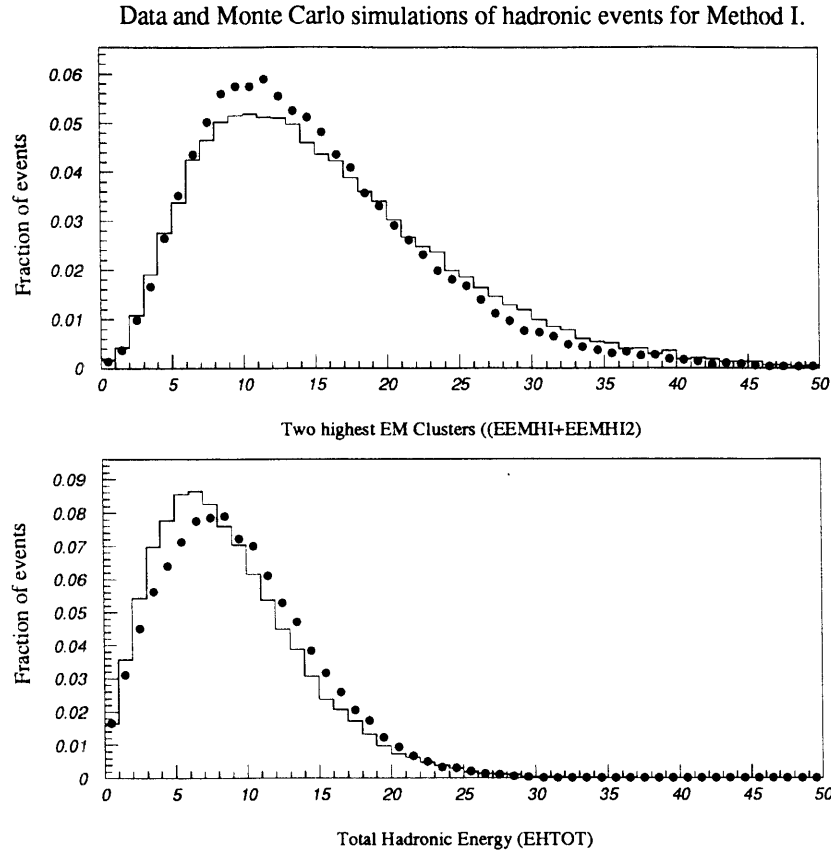
Figure 8-9: Comparison of the Method I variables EEMHI1+EEMHI2 and EHTOT for the Pass 2 hadronic sample data (dots) and hadronic event simulation (line).

central parts of the detector as defined above, are tabulated:

We can draw the following conclusions from the Method I analysis using Poisson estimates for observed events with backgrounds.

- For the central part of the detector:

  Data — 8 e^+e^- events observed in region A after cluster multiplicity cut.

  Simulated e^+e^- — 6.1 e^+e^- events expected in region A from simulations; 1.8 "hidden" e^+e^- events expected in region B.

  Simulated Hadronic — 9.6 hadronic events expected in region A.

- For the forward part of the detector:

  Data — 41 e^+e^- events observed in region A after cluster multiplicity cut.

  Simulated e^+e^- — 5.5 e^+e^- events expected in region A from simulations; 2.0 "hidden" e^+e^- events expected in region B.

Cut region	Data	e^+e^- simulation.	Hadronic simulation.
$A_{\text{pre-NCLUS}}$	2005	2005	9.6
$B_{\text{pre-NCLUS}}$	40861	60.2	39794
$A_{\text{post-NCLUS}}$	8	6.1	9.6
$B_{\text{post-NCLUS}}$	39689	1.8	39689

Cut region	Data	e^+e^- simulation.	Hadronic simulation.
$A_{\text{pre-NCLUS}}$	4619	4619	19.6
$B_{\text{pre-NCLUS}}$	12195	560.2	10998
$A_{\text{post-NCLUS}}$	41	5.5	19.6
$B_{\text{post-NCLUS}}$	10969	2.0	10969

Table 8.1: Estimate of Pass 2 cut efficiency with Method I. Pass 2 data and simulated events that pass Method I cuts, shown before and after the cluster multiplicity (NCLUS) cut of Pass 2, for the central (top) and forward (bottom) parts of the detector.

Simulated Hadronic — 19.6 hadronic events expected in region A.

Since we are trying to estimate the number of e^+e^- events, the hadronic events in region A are considered "background". In the central part of the detector, we observed 8 and estimated 1.8 "hidden" e^+e^- events, while expecting 9.6 hadronic events in region A, which yielded 7.45 events at 95% confidence level. For the forward part of the detector, we observed 41 and estimated 2.0 "hidden" e^+e^- events, while expecting 19.6 expected hadronic events in region A, which yielded 35.85 events at 95% confidence level.

We estimated the fraction of e^+e^- events in the data sample with Method I as: $f_b^{e^+e^-} \leq$ $(7.45+35.85)/50707 = 0.00085$, at 95% confidence level. We can also quote this value as a mean with 1σ uncertainty: $f_{e^+e^-}^{\text{Method I}} = (0.055 \pm 0.018)\%$ We note that the Method I probably underestimated the number of e^+e^- events in the hadronic region that survived the Pass 2 cuts, since it relied on cluster multiplicity distributions from detector simulations.

8.3.4 e^+e^- Background analysis Method II

Since Method I might have underestimated the contribution from e^+e^- events, a second attempt was made to estimate the e^+e^- background in the data. The Method II variables used to isolate the e^+e^- from the hadronic events were chosen such that the problem of "hidden" backgrounds, namely e^+e^- events misidentified as hadronic events, was negligible.
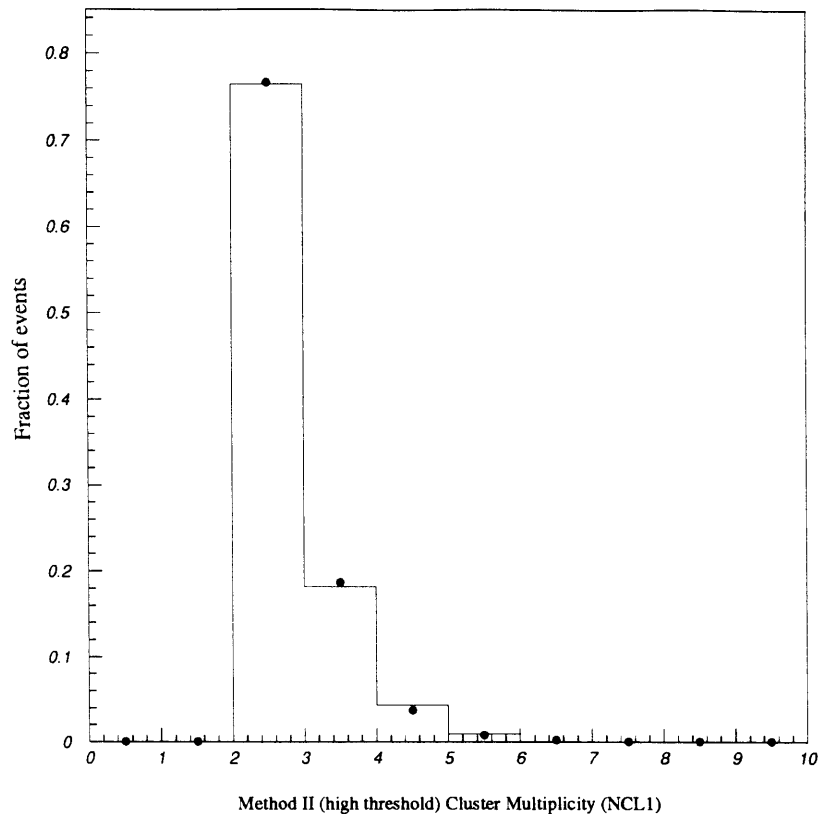
Figure 8-10: Comparison of Method II (high threshold) cluster multiplicity variable, NCL1 for simulated e^+e^- events (line) with e^+e^- rich data (dots), showing good agreement.

- **EEM1/ETOT**. The total energy in the EM section for clusters *above 1 GeV* (in the Min-I scale), over the total energy of the event.

- **NCL1**. The multiplicity of clusters over 1 GeV in the event.

Similar to Method I, we isolated large depositions of electromagnetic energy. Instead of looking at the highest energy towers, in Method II we examined the energy deposited in high energy clusters.

Fig. 8-10 shows a histogram comparing the high threshold cluster multiplicity (NCL1) for simulated e^+e^- events with the data that survived the Pass 2 energy and imbalance cuts but failed the cluster multiplicity cuts, and were therefore predominantly e^+e^- events (e^+e^--rich data). The agreement between data and simulation is quite good, which leads us to speculate that the problems with simulating the cluster multiplicity distributions lay predominantly in the low energy fragmentation simulation

We determined the selection criteria for the e^+e^- events as NCL1$\leq$5 and EEM1/ETOT$>$0.86. Fig. 8-11 (left) shows a scatter plot of the two variables for simulated e^+e^- events, while Fig. 8-11

Method II Variables for Simulated Bhabha Events
EEM1/ETOT

Method II Variables for Pass 2 Data
EEM1/ETOT

NCL1

NCL1

Figure 8-11: Scatter plot of the two Method II variables, NCL1 and EEM1/ETOT, for simulated e^+e^- events (left), and Pass 2 data. The lines represent the Method II cuts. The cut on NCL1 was chosen to contain most the e^+e^- events.

(right) shows the same scatter plot for all the Pass 2 data. The Method II cuts are represented as lines. 172 events, or 0.34%, of the Pass 2 selected data fall below the Method II cuts.

We note that the "hidden" backgrounds, e^+e^- events misidentified as hadronic ones, are negligible mainly due to the rather conservative cut on NCL1. However, 0.34% was considered a rather high estimate for the level of background, since there were hadronic and $\tau^+\tau^-$ events within those 172 events. We estimated the number of the $\tau^+\tau^-$ events in the entire 1993 SLD run to be ≈ 2550. We expected 61 of these events (0.12%) to be misidentified as e^+e^- events in the Method II analysis. We also attempted to remove hadronic decays misidentified as e^+e^- events. Of the 172 events, 58% had Central Drift Chamber information, of which 63% had six or more good tracks, consistent with the signature for a hadronic event. Therefore, over a third of the 172 events were identified as

hadronic decays. We removed only those events positively identified as hadronic events using Drift Chamber tracking information. Since the tracking information was only available for a little more than half the events in the barrel, and completely absent in the endcaps, this subtraction obviously left some hadronic events misidentified as e^+e^- events, especially in the forward part. Therefore Method II yielded an overestimate of the e^+e^- background. After subtracting the estimated $\tau^+\tau^-$ and known hadronic contribution, we were left with $f^{e^+e^-}_{Method\ II} = (0.14 \pm 0.05)\%$ as the Method II estimate of the e^+e^- contamination of the A_{LR} data set.

8.3.5 Final e^+e^- background estimate

From Method I we had an e^+e^- background estimate of $(0.055 \pm 0.018)\%$. From Method II we obtained an estimate of $(0.14 \pm 0.05)\%$. The large discrepancy between the two methods was due to an *underestimate* of the e^+e^- background by Method I (since it relied on cluster multiplicity simulations to predict e^+e^- events misidentified as hadronic events), and an *overestimate* in Method II (since counting only high energy clusters to obtain better agreement between cluster multiplicity simulation and data caused hadronic events to be misidentified as e^+e^- events). We averaged the two estimates and obtained a value of $f_{e^+e^-} = (0.10 \pm 0.06)\%$ as an estimate of e^+e^- contamination of the A_{LR} data set, consistent with the data-based estimate of $\approx 0.08\%$. The error was computed to account for the discrepancy between the two methods.

8.4 Beam Related Background

The beams at the SLC caused a lot of noise in the SLD detectors, primarily from electromagnetic and hadronic shower debris, initiated by off-beam particles intercepted by accelerator elements.

Simulations of beam-induced backgrounds were difficult. We used the data itself to place conservative limits on the amount of beam background in the data sample. The Pass 1 data, as plotted in Fig. 8-2 shows the total energy of the data versus the energy imbalance. The beam related background is seen clearly as the collection of data at high imbalance values. This is understandable, since beam related backgrounds were not correlated between the electron and positron beams. The beam related backgrounds were significantly higher in the forward part of the detector, therefore we investigated the data in the forward part exclusively to place limits on this background.

Fig. 8-12 shows a plot of the energy imbalance versus the cluster multiplicity for events that have passed the Pass 2 total energy cut only. The background events form a group at high energy imbalance, and are limited to less than 20 clusters. Therefore, we divided the data into two sets,
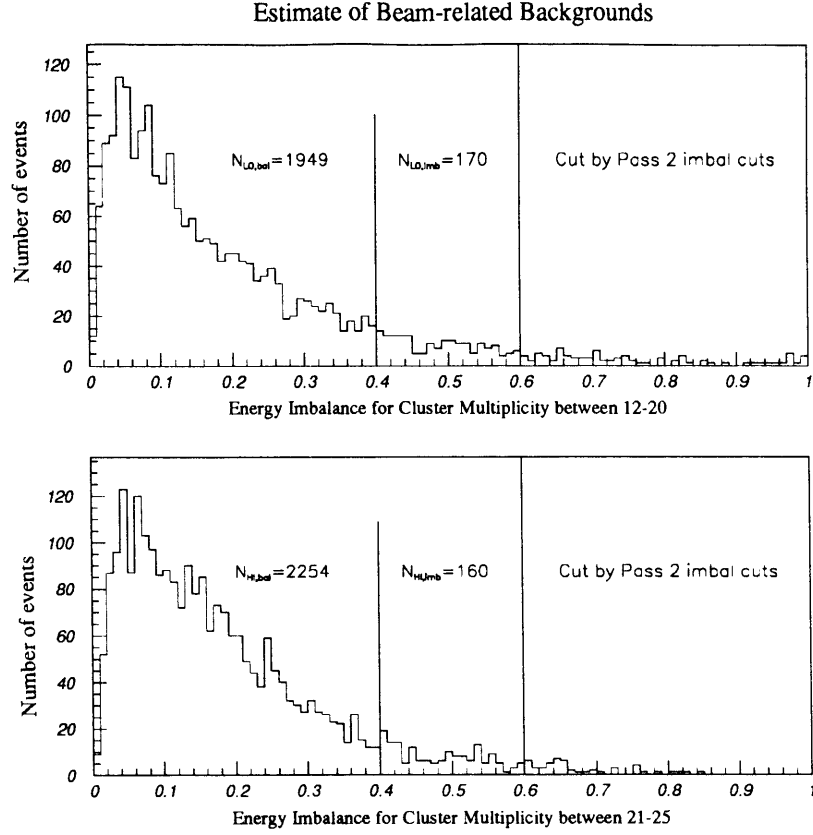
Energy Imbalance vs. Cluster Multiplicity

Figure 8-12: Cluster multiplicity vs. energy imbalance for data that passed the energy cut, but not the imbalance or cluster multiplicity cut in Pass 2 of the event selection. Beam backgrounds are isolated at high imbalance and low cluster multiplicity.

a *high* set, with cluster multiplicity between 21 and 25, and a *low* set with cluster multiplicity between 12 and 20. Fig. 8-13 shows the energy imbalance distribution for the data collected in the forward part of the detector, in the two different sets. Fig. 8-14 is a plot of the imbalance for simulated hadronic events, for the same two sets. The energy imbalance distribution for the simulated hadronic events was similar for high and low cluster multiplicity, but the beam backgrounds were highly imbalanced and at low cluster multiplicity. We used the high cluster multiplicity set to estimate the distribution of energy imbalance for good hadronic events.

Pass 2 of the event selection cuts rejected events with energy imbalance greater than or equal to 0.6. We assumed that the beam related background in the Pass 2 data lay predominantly in the imbalance region from 0.4 to 0.6, and predominantly in the low cluster multiplicity set. We defined the variables $N_{HI,imb}$, $N_{HI,bal}$, $N_{LO,imb}$, $N_{LO,bal}$ as the number of events in in a given cluster multiplicity and imbalance set, where first index denotes the cluster multiplicity, either the high

Estimate of Beam-related Backgrounds

Figure 8-13:   Histograms of energy imbalance for the low and high cluster multiplicity data
sets.

(HI), or low (LO) data set and the second index denotes the imbalance, either imbalance less than
0.4 (bal), or imbalance between 0.4 and 0.6 (imb). We found the following number of events in the
different cluster multiplicity – imbalance sets:

$$N_{\mathrm{LO,imb}} = 170$$
$$N_{\mathrm{LO,bal}} = 1949$$
$$N_{\mathrm{HI,imb}} = 160$$
$$N_{\mathrm{HI,bal}} = 2254$$

and the estimated background was

$$N_{background} = N_{\mathrm{LO,imb}} - N_{\mathrm{LO,bal}} \cdot \frac{N_{\mathrm{HI,imb}}}{N_{\mathrm{HI,bal}}} = 31.7 \tag{8.5}$$

We estimated the beam related background at $f_{beam} = (0.06 \pm 0.03)\%$.
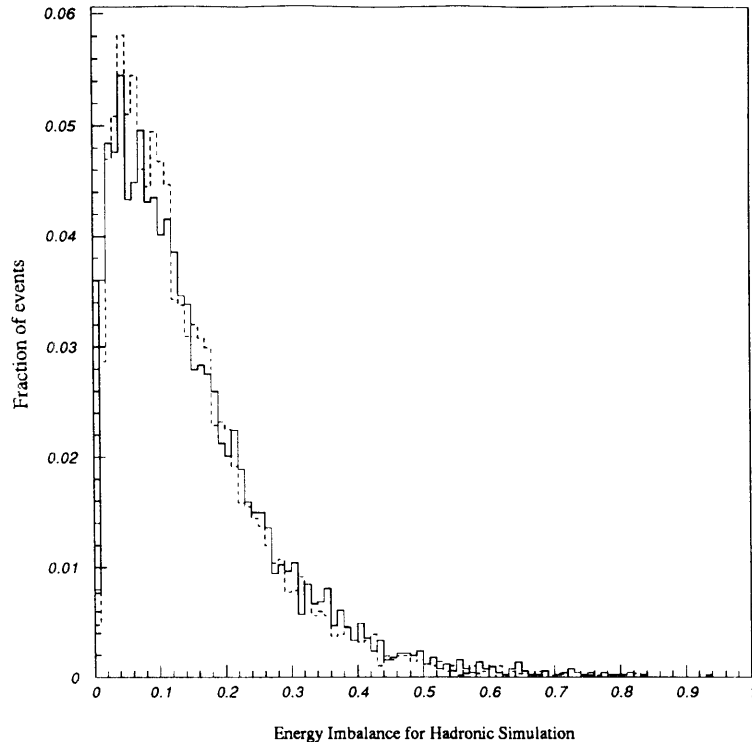
Figure 8-14: Energy imbalance for simulated hadronic events for the high NCLUS set (line) and low NCLUS set (dashes), used to estimate beam backgrounds. Hadronic events show no preference for low NCLUS and high imbalance, unlike the beam associated backgrounds.

8.5 Two Photon Backgrounds

There were two sources of backgrounds involving two photons. The first was the 2γ process, in which the incoming electron and positron each radiated a photon which coupled to a loop and radiated soft hadrons. A Feynman diagram is shown in Fig. 8-15. In 2γ events, the beam particles remained unobserved in the beampipe. The photon-fusion products deposited small amounts of highly unbalanced energy in the detector.

Simulated 2γ events were generated using a Monte Carlo generator based on known physical properties of the process [53]. The events were passed through the SLD detector simulation and event selection. No events passed the filter. Normalizing the Monte-Carlo statistics to the luminosity obtained in the 1993 run, we expected no more than 1.5 events at the 95an estimate of the 2γ background at $f_{2\gamma} < 0.003\%$ at 95% confidence level.

The second source of background involving two photons was the QED $\gamma\gamma$ radiative process — radiative photons produced by the exchange of a virtual electron. A Feynman diagram is shown in Fig. 8-15. $\gamma\gamma$ events could be a source of background for the A_{LR} measurement since they proceed
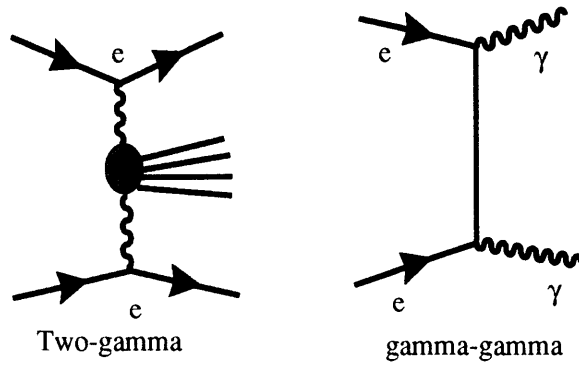
Figure 8-15: Feynman diagrams for 2-γ and $\gamma\gamma$ backgrounds.

through a QED interaction. However, the cross-section for such events is quite small compared to the Z production cross-section at the SLC energy of $\sqrt{s} = 91.26$ GeV [54]. The total cross section for $\gamma\gamma$ events was calculated to be 0.1% of Bhabha cross section within the LAC acceptance. Since $\gamma\gamma$ events deposit electromagnetic energy in two highly balanced groups, they would have been indistinguishable from e^+e^- events for the calorimeter-only analysis. Therefore, they would have been rejected by the Pass 2 cluster multiplicity cuts with the same efficiency as the final state e^+e^- events, and contributed a negligible amount to the background.

8.6 Cosmic Ray Background

The background from high energy muons from cosmic rays was negligible in the 1993 data set. The A_{LR} data were selected using a number of calorimeter based cuts, and high energy muons did not deposit enough energy in the LAC to trigger the detector or to pass any of the subsequent cuts, since they were minimum ionizing particles.

We estimated the number of cosmic rays in the data sample using a Monte-Carlo. We relaxed the criteria for energy from 22 GeV to 20 Gev, and the energy imbalance from 0.6 to 0.9. In this way, we obtained an overestimate on the number of cosmic rays events in the data. Normalizing the Monte Carlo to the known flux of cosmic rays, we were able to limit the background to be $f_{\text{cosmic}} < 0.005\%$ at 95% confidence.

8.7 Background Asymmetry

Since the background contained events that can manifest a left-right asymmetry different than that of the data, we had to estimate this asymmetry and correct the data for it. In previous

Background Type	Fraction of data set	Associated asymmetry
e^+e^- events	$f_{e^+e^-} = (0.10 \pm 0.06)\%$	0.052 ± 0.010
Beam related	$f_{\text{beam}} = (0.06 \pm 0.03)\%$	0
2γ	$f_{2\gamma} < 0.003\%$ at 95% confidence	0
$\gamma\gamma$	negligible	0
Cosmic ray	$f_{\text{cosmic}} < 0.005\%$ at 95% confidence	0
Total	$f_b = (0.17 \pm 0.07)\%$	0.031 ± 0.019

Table 8.2: **Summary of background fractions and associated asymmetry.**

such analyses [55], the asymmetry of the background was assumed to be zero. However, since the background contained e^+e^- events, this assumption was not necessarily true. We estimated the background asymmetry by obtaining the theoretical angular distribution of the asymmetry in e^+e^- events from the ALIBABA program [56]. We then weighted this asymmetry by an estimate of the angular distribution of the e^+e^- part of the background, and obtained $A_{e^+e^-} = 0.052 \pm 0.010$. To obtain the asymmetry of the total background, we multiplied $A_{e^+e^-}$ by the fraction of e^+e^- events in the background and obtained

$$A_b = A_{e^+e^-} \cdot \frac{f_{e^+e^-}}{f_b} = 0.031 \pm 0.019. \qquad (8.6)$$

8.8 Background Estimate Summary

We summarize the background in the A_{LR} data set in table 8.2 below:

We note that final state e^+e^- events contributed the largest fraction of the estimated background, and the total background estimate was small (0.17%) We also note that the background manifested a left-right asymmetry of 0.031. The backgrounds and their associated asymmetry had a small ($\approx 0.1\%$) relative effect on the value of A_{LR}.

Chapter 9

Measurement of A_{LR}

In this chapter, we combine the luminosity weighted beam polarization, $\mathcal{P}_e^{lum}$, as determined by the Compton polarimeter (after the chromatic correction has been applied) with the Z data sample collected by the SLD detector, and arrive at an estimate of A_{LR}.

We determine the measured value of the asymmetry, A_m, as defined in Eq. 1.31. In order to do this, we simply counted the number of Z events in our sample that were created with a left-handed electron beam, subtracted the number that were created with a right-handed beam, and divided this difference by the total number of events. We collected a total of 49,392 hadronic Z events after all cuts, of which 27,225 were created with left-handed electron beam and 22,167 with right-handed beam, listed in table 9.1. Using this data, we formed the measured asymmetry,

$$A_m = \frac{N_L - N_R}{N_L + N_R} = 0.1024 \pm 0.0045, \tag{9.1}$$

where $N_L, (N_R)$ are the number of Z events created by the left- (right-) handed beam. The error quoted is purely statistical. However, as mentioned earlier, we cannot use Eq. 1.31 to determine A_{LR}. We use instead,

$$A_{LR} = \frac{A_m}{\mathcal{P}_e^{lum}} + \frac{1}{\mathcal{P}_e^{lum}} \left[f_b(A_m - A_b) - A_{\mathcal{L}} - A_m^2 A_{\mathcal{P}} - \frac{E_{c.m.}}{\sigma_{c.m.}} \left. \frac{d\sigma}{dE} \right|_{c.m.} A_E - A_\varepsilon + \mathcal{P}_e \mathcal{P}_p \right], \tag{9.2}$$

where $\mathcal{P}_e^{lum} = 63.0\%$ is the luminosity weighted beam polarization after the chromatic correction; f_b and A_b are the backgrounds in the Z data sample and the left-right asymmetry in this background, respectively; $A_{\mathcal{L}}$ is the left-right asymmetry in the luminosity; $A_{\mathcal{P}}$ is the left-right asymmetry in the magnitude of beam polarization; A_E is the asymmetry in the beam energy; A_ε is the asymmetry in the detector efficiency, and $\mathcal{P}_p$ is possible positron beam polarization. Effects corresponding to terms

Type of Z	Number of events
Left-handed	27225
Right-handed	22167
Total	49,392
$\mathcal{P}_e^{lum}$	63.0%

Table 9.1:   Hadronic Z totals for 1993.

Correction	Value (10^{-4})	δA_{LR} (10^{-4})	$\delta A_{LR}/A_{LR}(\%)$
Background fraction, f_b.	17 ± 7		
Background Asymmetry, A_b.	310 ± 190	$+1.9 \pm 1.5$	$+0.12 \pm 0.09$
Luminosity Asymmetry, $A_{\mathcal{L}}$.	0.38 ± 0.50	-0.6 ± 0.7	-0.037 ± 0.049
Polarization Asymmetry, $A_{\mathcal{P}}$.	-33 ± 1	-0.5 ± 0.02	-0.034 ± 0.001
Energy Asymmetry, A_E.	0.0044	0.015 ± 0.0003	0.00090 ± 0.00002
Efficiency Asymmetry, A_ϵ.	0	0	0
Positron Polarization, $\mathcal{P}_p$.	≤ 0.17	≤ 0.17	≤ 0.010
Total		0.99 ± 1.7	0.06 ± 0.10

Table 9.2:   Background and machine bias corrections to A_{LR}.

in the square brackets are labelled background biases and machine biases, and are discussed below. The data were investigated for correlations with several event-specific quantities, and the measured asymmetry was found not to vary in a statistically significant way. These studies are presented in section B.2 of the Appendix.

9.1   Background and Machine Biases

In general, a machine bias can change the number of left- and right- handed Z events recorded. These biases have to be measured and corrected for. The background fraction f_b and the asymmetry in the background A_b have already been presented in the chapter on event selection, (chapter 8). The correction to A_{LR} due to background and associated asymmetry is

$$\delta A_{LR}(f_b, A_b) = (1.9 \pm 1.5) \times 10^{-4}.$$

The luminosity asymmetry, $A_{\mathcal{L}}$

The beam luminosity for right and left handed beams was not exactly equal for the 1993 run of the SLC, due to an asymmetry in the electron current extracted from the photocathode. The most probable cause of this current asymmetry is the lack of perfect circular polarization for the source laser. Fortunately, the beam current asymmetry and thereby the luminosity asymmetry was reduced by a one-time reversal of the sign of the field in the LTR solenoid, which determined the sign of vertical polarization in the North Damping ring. With the solenoid field sign such that the spins were stored spin-up in the Damping Ring, left-handed light on the cathode led to left-handed electrons at the IP. With the solenoid field sign reversed, the same left-handed light on the cathode now led to right-handed electrons at the IP. Therefore any biases traceable to the source laser were reduced by having their sign reversed once during the run.

We determined the value of the luminosity asymmetry by determining the asymmetry in the beam current, as measured by toroids located in the Final Focus region. In addition, a further estimate of the luminosity asymmetry was made by the radiative Bhabha luminosity monitor in the North Arc of the SLC. A third, cruder measurement of the luminosity asymmetry was made by the SLD luminosity monitor which measured final state e^+e^- events at low angle. These were almost entirely Bhabha events, which proceed through t-channel photon exchange and had a very small left-right asymmetry, $\approx -1.5 \times 10^{-4}$. Therefore any asymmetry measured in these events was almost certainly due to a machine induced luminosity asymmetry. However, the determination of $A_{\mathcal{L}}$ using Bhabha events recorded by the SLD luminosity monitor was limited by statistics.

Using the beam current toroids and the North Arc radiative Bhabha monitor, we arrived at a value for the luminosity asymmetry $A_{\mathcal{L}} = (3.8 \pm 5.0) \times 10^{-5}$, which lead to a correction to A_{LR} of

$$\delta A_{LR}(A_{\mathcal{L}}) = (-0.6 \pm 0.7) \times 10^{-4}.$$

The crude cross-check of $A_{\mathcal{L}}$ using 125375 small-angle Bhabha events recorded by the SLD luminosity monitor yielded $A_{\mathcal{L}}^{\mathrm{SLD-LUM}} = (-32 \pm 28) \times 10^{-4}$, which was consistent with the more precisely determined value.

Beam Polarization Asymmetry, A_P

A difference in the magnitude of the polarization between the left-handed and right handed beam would have caused the measured value of A_{LR} to be biased. The Compton Polarimeter, described in section 3.2, measured the polarization for the left- and right-handed beam independently. The measured value for the beam polarization asymmetry was $A_P = (-33 \pm 1) \times 10^{-4}$, which caused a

correction to A_{LR} of

$$\delta A_{LR}(A_{\mathcal{P}}) = (0.5 \pm 0.02) \times 10^{-4}.$$

Energy Asymmetry, A_E

An energy difference between the left and right handed beams would have manifested itself as a bias in the left-right asymmetry, because the cross section at the Z pole varies with energy. The term in Eq. 9.2 corresponding to the bias in A_{LR} due the energy asymmetry, A_E, depends on $E_{c.m}, \sigma_{c.m.}$, and $\frac{d\sigma}{dE}\big|_{c.m.}$. The energy asymmetry was measured directly by the WISRD energy spectrometer (section 3.1.5), and found to be $A_E = (4.4 \pm 0.1) \times 10^{-7}$. The energy asymmetry was also thought to be a by-product of the beam current asymmetry (as was the luminosity asymmetry) due to beam-loading effects in the accelerator. However, the asymmetry was small compared to the derivative of the Z cross section at the measured energy of $E_{c.m} = 91.26$ GeV. We calculated a value of $\frac{d\sigma}{dE}\big|_{c.m} = 0.023$ GeV^{-1}, which yielded a correction to A_{LR} of

$$\delta A_{LR}(A_E) = (0.015 \pm 0.0003) \times 10^{-4}.$$

Efficiency Asymmetry, A_ε

If the Z detection hardware or analysis somehow preferred events created with left or right handed beam, there would have been an obvious left-right bias. Since the polar angle distribution for fermions from a Z produced by right-handed beams is the same as that for anti-fermions from a Z produced by left-handed beams, a difference in detector acceptance for fermions versus anti-fermions, coupled with a polar-angle asymmetry in detector acceptance, could lead to a non-zero A_ε.

However, we note that the process of calorimetry is symmetric with respect to matter and anti-matter. Electromagnetic and hadronic showers induced in the LAC, on which the Z selection criteria were based, were similar for fermions and anti-fermions. In addition, the acceptance of the detector was symmetric in polar angle. Any of these criteria by itself guaranteed that $A_\varepsilon = 0$. Therefore, the correction to A_{LR} was

$$\delta A_{LR}(A_\varepsilon) = 0.$$

Possible Positron Polarization, $\mathcal{P}_p$

Any residual polarization of the positron beam would have biased the A_{LR} result. There was no known source of positron polarization, and the South Damping Ring and the South Arc, used to cool the positrons and transport them to the IP, were not optimized for spin transport in the way

Systematic Uncertainty	$\delta A_{LR}/A_{LR}$
Polarimeter	1.3%
Chromaticity	1.1%
Machine biases and backgrounds	0.1 %
Total	**1.7%**

Table 9.3: Systematic Errors for the A_{LR} measurement.

that the North Damping Ring and North Arc were. However, we had to consider possible accidental polarization of the positrons.

We have shown in section 2.2.1 that any effect due to possible polarization of the positrons due to "scavenger" electron polarization vanished because the source laser helicity was selected pseudo-randomly. The only other possibility for accidental positron polarization was fixed-sign polarization, due to the Sokolov-Turnov effect in the South Damping Ring. The Sokolov-Turnov effect [57] predicts buildup of polarization in storage rings as a function of the storage time. The polarization buildup proceeds with a characteristic time constant which varies as R^3/γ^5 where R is the radius of the storage ring and γ is the Lorentz factor. For the Damping Rings at the SLC, the polarization buildup time is computed to be 960 s. The actual storage time for an SLC pulse in the Damping Rings was 16 ms. Therefore any fixed-sign positron polarization due to the Sokolov-Turnov effect in the South Damping Ring was $\mathcal{P}_p \leq \frac{16 \times 10^{-3} \, s}{960 \, s} = 1.7 \times 10^{-5}$. This lead to a correction to A_{LR} of

$$\delta A_{LR}(\mathcal{P}_p) \leq 0.17 \times 10^{-4}.$$

We summarize the various corrections to A_{LR} from Eq. 9.2 in table 9.2, and the total systematic uncertainty in table 9.3. We note that the total correction to A_{LR} is negligible compared to the statistical uncertainty of $\sim 4\%$.

9.2 The A_{LR} Result.

We combined the measured asymmetry, given in Eq. 9.1, and the luminosity weighted polarization as determined by the Compton Polarimeter, given in Eq. 4.15, and corrected for the chromatic effect, given in Eq. 7.12. We used Eq. 9.2 to calculate A_{LR}:

$$A_{LR}(91.26 \text{ GeV}) = 0.1626 \pm 0.0071 \pm 0.0030, \tag{9.3}$$

where the first error is statistical and the second systematic.

We can use the program ZFITTER, introduced in section 1.5, to determine the value of the effective Weak mixing angle, $\sin^2 \theta_W^{\text{eff}}$. The corrections made in ZFITTER include initial state radiation and virtual QED and electroweak corrections due to Standard Model phenomena. We cross-check the result obtained from ZFITTER with another such program, EXPOSTAR, and obtain similar results. The effective Weak mixing angle is

$$\sin^2 \theta_W^{\text{eff}} = 0.2292 \pm 0.0009 \pm 0.0004, \tag{9.4}$$

where the first error is statistical and the second systematic. We combined our result with the 1992 SLD result and obtained

$$\sin^2 \theta_W^{\text{eff}} = 0.2294 \pm 0.0009 \pm 0.0004, \tag{9.5}$$

We can present the result as an effective value for the left-right asymmetry,

$$A_{LR}^0 = 0.1656 \pm 0.0071 \pm 0.0030.$$

9.3 Comparisons with other electroweak measurements

The result presented in Eq. 9.5 is the single most precise measurement of $\sin^2 \theta_W^{\text{eff}}$ available to date. There are several other measurements of this parameter. Of note are the four detectors at the LEP storage ring at CERN. These have resulted in published measurements of electroweak parameters at the Z pole [58]. Since longitudinal beam polarization is difficult to achieve in a storage ring, the LEP collaborations have so far chosen not to pursue the A_{LR} measurement. They have, however, far greater number of Z events than does SLD to date. Using measurements of forward-backward asymmetry, A_{FB} for various final states and tau-polarization, $\mathcal{P}_\tau$, the four LEP detector collaborations have determined the Weak mixing angle to be $\sin^2 \theta_W^{\text{eff}} = 0.2322 \pm 0.0005$ [59]. This determination was derived from an average of thirty separate measurements from the four detectors, with correlations taken into account in the averaging process. We note that the measurement of $\sin^2 \theta_W^{\text{eff}}$ from Eq. 9.5 differs from the LEP average by ≈ 2.5 standard deviations. Fig. 9-1 compares the SLD A_{LR} determination of $\sin^2 \theta_W^{\text{eff}}$ with various LEP measurements.
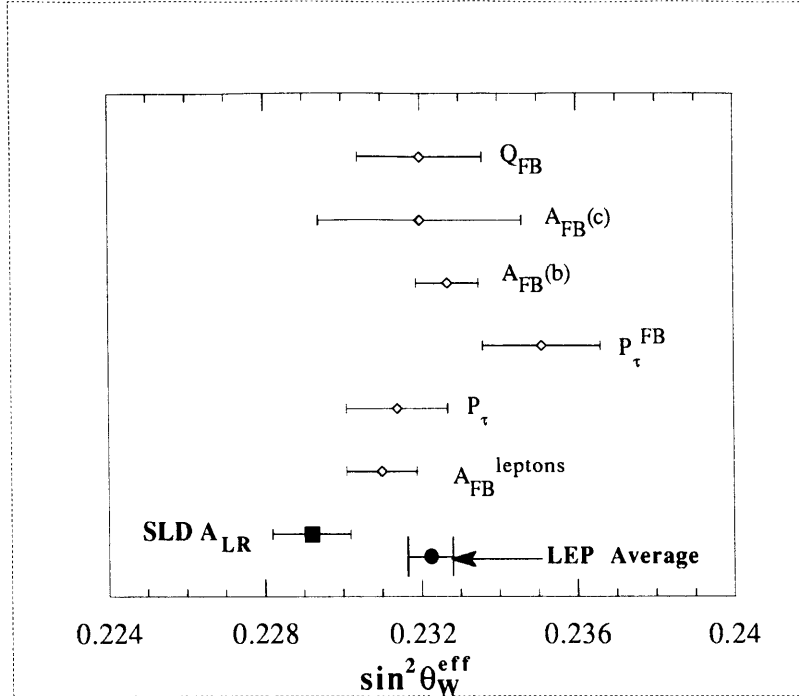
Figure 9-1: Comparison of SLD and LEP determinations of $\sin^2\theta_W^{\text{eff}}$. The value from A_{LR} is $\sin^2\theta_W^{\text{eff}} = 0.2292 \pm 0.001$, while the LEP average is $\sin^2\theta_W^{\text{eff}} = 0.2322 \pm 0.0005$.

9.4 Comparison with the Standard Model

We here compare the A_{LR} measurement from the value predicted by the Standard Model of Particles and Fields. As noted in section 1.1, the tree-level Standard Model is described by the three well determined quantities, α, G_F, and M_Z. The first and second order corrections to the Standard Model predictions were incorporated in the program ZFITTER. The mass of the top quark, m_t and the Higgs Boson. m_H, had to be specified in the ZFITTER calculation. Suitable ranges were chosen for m_t and m_H, thereby determining a range for the Standard Model prediction of A_{LR}. In addition, the running of α to $\sqrt{s} = M_Z$ added a theoretical uncertainty of $\delta\sin^2\theta_W^{\text{eff}} = 0.0003$ to the Standard Model prediction. Table 9.4 lists some Standard Model predictions for $\sin^2\theta_W^{\text{eff}}$, where m_H ranges from 60 Gev to 1 TeV, and the m_t range (for the first three rows of the table) is taken from the recently published paper setting out evidence for the top quark by the CDF collaboration [13]. We note that the Standard Model prediction is approximately 2.5 standard deviations away from the determination of $\sin^2\theta_W^{\text{eff}}$ in Eq. 9.5, in the direction of a small value of m_H, and a large value of m_t.

151

m_t GeV	$\sin^2 \theta_W^{\text{eff}}$ Prediction ($m_H = 60$ GeV)	$\sin^2 \theta_W^{\text{eff}}$ Prediction ($m_H = 1$ TeV)
158	0.2319	0.2334
174	0.2313	0.2329
190	0.2307	0.2323
240	0.2285	0.2303

Table 9.4: Standard Model predictions of $\sin^2 \theta_W^{\text{eff}}$ for certain m_H, m_t assumptions. The first three rows correspond to accepted values for m_t, while the fourth row is a fit for m_t using the SLD determination of $\sin^2 \theta_W^{\text{eff}}$.

Chapter 10

Summary and Future Plans

10.1 Summary of Results

The A_{LR} measurement presented in this thesis,

$$A_{LR} = 0.1626 \pm 0.0071 \pm 0.0030,$$

leads to the single most precise determination of the effective Weak mixing angle to date,

$$\sin^2 \theta_W^{\text{eff}} = 0.2292 \pm 0.0009 \pm 0.0004.$$

The value presented in this thesis differs by approximately 2.5 standard deviations from the determination of $\sin^2 \theta_W^{\text{eff}}$ made by the four LEP collaborations, as well as predictions of $\sin^2 \theta_W^{\text{eff}}$ by the Standard Model. However, the discrepancy is not yet compelling.

10.2 Future Plans

Further data collected by both the SLD collaboration and the four LEP collaborations will reduce the mainly statistical errors on the determination of $\sin^2 \theta_W^{\text{eff}}$ in the near future. The SLC has achieved a beam polarization of $\approx 80\%$, and the SLD plans to collect 100,000 Z events with this polarization by 1995. Eventually, the SLD plans to collect over 500,000 Z events with high polarization, in an extended three year run.
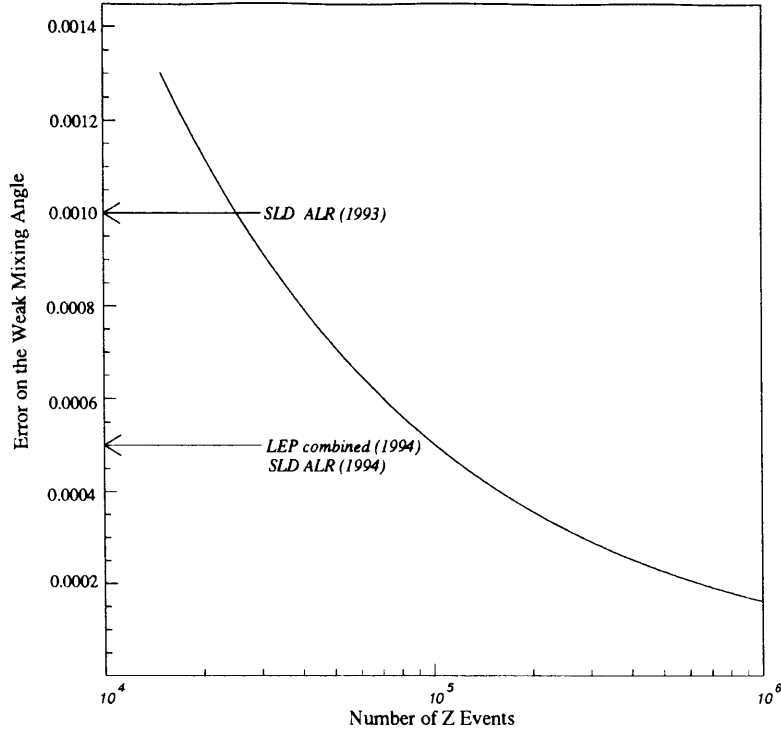
Figure 10-1: Error on $\sin^2 \theta_W^{\text{eff}}$ versus number of Z events at 80% e^- beam polarization, and $\delta \mathcal{P}/\mathcal{P} = 1\%$.

Fig. 10-1 shows a plot of the error on the effective Weak mixing angle, $\delta \sin^2 \theta_W^{\text{eff}}$ determined by A_{LR}, as a function of the number of Z events recorded. The beam polarization is assumed to be $\mathcal{P}_e = 80\%$, and the error on the polarization determination is assumed to be $\delta \mathcal{P}_e/\mathcal{P}_e = 1\%$. We note that in 1994, the measurement of A_{LR} will yield a determination of $\sin^2 \theta_W^{\text{eff}}$ to an error of $\delta \sin^2 \theta_W^{\text{eff}} = 0.0005$, while the extended run promises further precision in the determination, perhaps reducing the error to $\delta \sin^2 \theta_W^{\text{eff}} = 0.0002$.

The theoretical error on the Standard Model Determination of the weak mixing angle is $\delta \sin^2 \theta_W^{\text{eff}} \approx 0.0003$. The SLD measurement of A_{LR} will determine $\sin^2 \theta_W^{\text{eff}}$ to this precision by the end of 1996. Hopefully by then, the purely *experimental* discrepancy with the LEP determination of $\sin^2 \theta_W^{\text{eff}}$ will have been resolved (certain LEP experiments have recently made public results that differ less than earlier ones from A_{LR}) and the *theoretical* discrepancy with the Standard Model, if any, can be investigated. A precise determination of the top quark mass by the CDF and D0 collaborations will eliminate one free parameter from the determination of $\sin^2 \theta_W^{\text{eff}}$, leaving its value more sensitive to the Higgs mass and possible phenomena beyond the Standard Model. Appendix A discusses one possible way the effects of such phenomena on the weak mixing angle and other electroweak observables can be understood; several other methods have been proposed and more are expected. Even

if such new phenomena do not exist, ever more precise measurements of A_{LR} will be of primary importance in confining the Standard Model. If such phenomena do exist, the A_{LR} measurement will be of supreme importance in determining the nature of the phenomena, and in guiding the next generation of experiments to make a direct observation.

Appendix A

Physics Beyond the Standard Model: S, T, U Parameters

Propagator corrections to the tree level process $e^+e^- \to f\bar{f}$ have been introduced in section 1.5.2. These corrections are known as oblique corrections since they effectively change the constants that regulate the coupling of the fermion current to the boson propagator. Oblique corrections are the most important of the corrections beyond tree level that need to be applied to A_{LR}. There have been many calculations of the effects of physics phenomena beyond the Standard Model on electroweak observables [60]. In this appendix, we discuss a generalized parameterization of oblique corrections, due to Peskin and Takeuchi [61], which yields indicators sensitive to possible physics beyond the Standard Model.

A.1 Oblique corrections

Oblique corrections consist of changes to the tree level propagator. The first-order correction is a vacuum fluctuation loop correction. Higher orders can bring in more loops, as well as corrections significantly more complex than simple loops. We consider only first order loop corrections.

A first-order loop correction to a propagator divides the propagator into two sections, which may not correspond to the same boson. The magnitude of the correction depends on the mass of the vacuum fluctuations current, making electroweak observables such as A_{LR} sensitive to the mass of the top quark and Higgs boson.

The corrections previously discussed incorporated vacuum fluctuations to Standard Model particles only, since the goal of this work is to test the Standard Model. However, a more generalized approach, in which the correction parameters are allowed to vary, permits us visualize the general agreement with the Standard Model and some of its extensions.

A.2 S, T, U Parameters

The S, T, and U parameters of Peskin and Takeuchi parameterize all oblique corrections due to new physical phenomena, circumscribed by and commensurate with the following constraints:

1. The $SU(2) \times U(1)$ symmetry for electroweak interactions must hold. This requirement precludes the addition of new physics due to an additional symmetry group leading to, for example, a new vector boson (Z').

2. The $SU(2)$ (*custodial*) symmetry must be valid for the Higgs sector. This symmetry leads to the Higgs doublet. The requirement of custodial symmetry precludes the addition of the more exotic models of spontaneous symmetry breaking, for example those with Higgs triplets.

3. The new physical phenomena must be manifest primarily in the oblique (vacuum polarization) corrections. Direct (vertex and box diagram) corrections due to a large class of gauge-model extensions to the Standard Models have be shown to be small for weak-interaction processes involving only light fermions as external particles, which are the only processes accessible to present experiments.

4. The corrected propagators can be expressed as Taylor expansions expressed in q^2 about the tree-level propagator. This requirement essentially restricts the mass scale of any new physics phenomenon to be large, $M_Z/M_{new} \ll 1$.

A.2.1 The Π functions

Fig. A-1 presents the first order corrections to the tree-level propagator. The functional dependence of these corrections are contained in constructs labelled Π-*functions*. The Π functions have two subscripts that identify the propagator before and after the vacuum fluctuation loop. These subscripts run over the range $Q, 1, 2, 3$, for the γ and the three components of weak isospin.

Approximations to the Π functions are made assuming that corrections beyond the tree-level ($\Pi(0)$) are small enough for a Taylor expansion in q^2 to be valid. Since we are making our observations
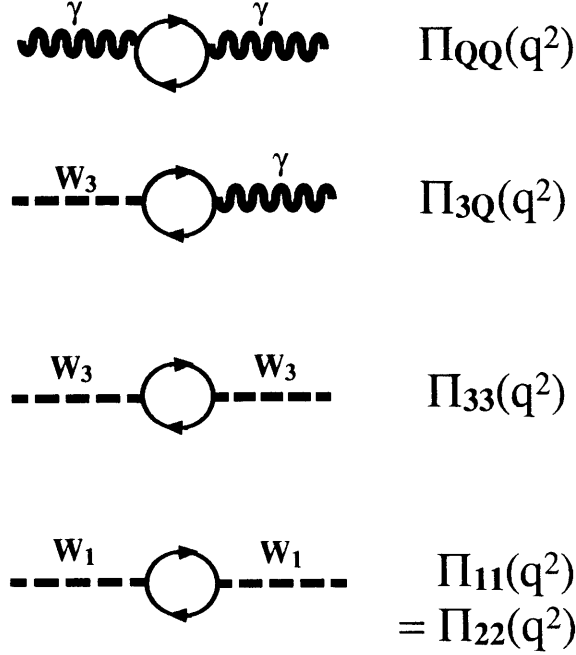
$\Pi_{QQ}(q^2)$

$\Pi_{3Q}(q^2)$

$\Pi_{33}(q^2)$

$\Pi_{11}(q^2)$
$= \Pi_{22}(q^2)$

Figure A-1: Oblique corrections and their dependence on the Π functions.

at $q^2 = M_z^2$, the assumption is equivalent to the requirement that $q^2/M_{new}^2 \approx M_Z^2/M_{new}^2 \ll 1$. The Π functions are approximated as follows:

$$
\begin{aligned}
\Pi_{QQ}(q^2) &\approx q^2\Pi'_{QQ}(0), \\
\Pi_{3Q}(q^2) &\approx q^2\Pi'_{3Q}(0), \\
\Pi_{33}(q^2) &\approx \Pi_{33}(0) + q^2\Pi'_{33}(0), \\
\Pi_{11}(q^2) &\approx \Pi_{11}(0) + q^2\Pi'_{11}(0),
\end{aligned}
\tag{A.1}
$$

where $\Pi' \equiv d\Pi/dq^2$. The functional form of Π_{22} is equivalent to that for Π_{11} and is not listed. The tree-level expressions $\Pi_{QQ}(0)$, and $\Pi_{3Q}(0)$ vanish due to the QED Ward identity. We are left with six independent parameters that parameterize the oblique corrections. The three precision measurements of α, G_F, and M_Z satisfy three of those degrees of freedom. the remaining three degrees of freedom are essentially loop corrections. They are parameterized by the three variables S,T, and U.

A.2.2   The S,T, and U variables

The Π functions listed in Eq. A.1 contain ultraviolet divergencies. However, since the differences of these functions correspond to physical parameters, and therefore the divergencies cancel in the

differences. The following variables are defined as difference combinations of the Π functions:

$$S \equiv \frac{4e^2}{\alpha} \left[\Pi'_{33}(0) - \Pi'_{3Q}(0) \right]$$

$$T \equiv \frac{e^2}{\alpha \sin^2 \theta_W \cos^2 \theta_W M_Z^2} \left[\Pi_{11}(0) - \Pi_{33}(0) \right]$$

$$U \equiv \frac{4e^2}{\alpha} \left[\Pi'_{11}(0) - \Pi'_{33}(0) \right] \tag{A.2}$$

A full discussion of the choice of combinations for the S, T, and U variables, and their resultant dependence on various parameters such as the top quark mass, Higgs boson mass, and parameters from theories beyond the Standard Model is beyond the scope of this discussion. However, we note a few facts about S, T, and U.

The parameters S and T partition the contribution of electroweak corrections into pieces with distinct physical significance. This separation is most clear when U≈0. In fact, all three variables, S, T, and U are close to zero if only those oblique corrections allowed by the Standard Model are applied. The freedom to choose the top quark mass, m_t, and the Higgs mass, m_H, allows some leeway within the confines of the Standard Model. U is expected to remain close to zero even for a large class of extensions to the Standard Model. The S variable is sensitive to new physical phenomena that conserve weak isospin symmetry, while the T variable is sensitive to phenomena that violate weak isospin symmetry. We note the functional dependence of the variables for different types of oblique corrections to electroweak observables. Any significant deviation of S and T from zero would signal the effect of physical phenomena not accounted for in the Standard Model.

We first consider effect of a new heavy fermion doublet of mass m_N and m_E for the weak isospin doublet partners. The S, T, and U variables take on the following values:

$$S \approx \frac{1}{6\pi},$$

$$T \approx \frac{1}{12\pi \sin^2 \theta_W \cos^2 \theta_W} \left(\frac{(\Delta m)^2}{M_Z^2} \right),$$

$$U \approx \frac{2}{15\pi} \left(\frac{(\Delta m)^2}{m_N^2} \right), \tag{A.3}$$

where $\Delta m = |m_N - m_E|$. Each additional generation of fermions will contribute additively to S and T. The dependence of T on Δm^2 measures the amount of weak isospin breaking in the new generation.

The contribution to S, T, and U due to a Higgs boson is as follows:

$$S \approx \frac{1}{12\pi} \ln\left(\frac{m_H^2}{m_{H,ref}^2}\right),$$

$$T \approx -\frac{3}{16\pi \cos^2 \theta_W} \ln\left(\frac{m_H^2}{m_{H,ref}^2}\right),$$

$$U \approx 0, \tag{A.4}$$

where m_H is the mass of the Higgs boson, and $m_{H,ref}$ is the reference value for the Higgs boson mass at which S, T, and U are defined. Both S and T are only logarithmically dependent on m_H.

Finally, we consider the effect on S, T, and U due to the top quark by evaluating Eq. A.3, limiting m_E to be zero, and and accounting for the additional factor of 3 due to color.

$$S \approx -\frac{1}{6\pi} \ln\left(\frac{m_t^2}{m_{t,ref}^2}\right),$$

$$T \approx \frac{1}{16\pi \sin^2 \theta_W \cos^2 \theta_W} \ln\left(\frac{m_t^2 - m_{t,ref}^2}{M_Z^2}\right),$$

$$U \approx \frac{1}{2\pi} \ln\left(\frac{m_t^2}{m_{t,ref}^2}\right), \tag{A.5}$$

where m_t is the mass of the top quark and $m_{t,ref}$ is the reference value of the top quark mass. The S variable is only logarithmically dependent on m_t, but the T variable is quadratically dependent on m_t. T is sensitive to weak isospin breaking effects, and a large m_t (with the bottom quark mass $m_b \sim 4.2$ GeV) constitutes a significant violation of weak isospin.

A.3 The S, T Dependence of Electroweak Observables

Oblique correction effect every electroweak observable in a different way, leading to different dependencies on S and T. With several precisely determined observables, we should be able to determine S and T and observe any possible deviation from values predicted by the Standard Model. We list the S and T dependence of several electroweak variables:

$$A_{LR} = A_e = 0.1297 - (2.82 \times 10^{-2})S + (2.00 \times 10^{-2})T,$$

$$\Gamma_Z = 2.484 - (9.58 \times 10^{-3})S + (2.615 \times 10^{-2})T,$$

$$\frac{M_W}{M_Z} = 0.8787 - (3.15 \times 10^{-3})S + (4.86 \times 10^{-2})T + (3.70 \times 10^{-3})U,$$

$$R_\nu = 0.3126 - (2.32 \times 10^{-3})S + (6.46 \times 10^{-3})T,$$

$$Q_W(^{133}_{55}Cs) \quad = \quad -73.31 - 0.790S - 0.011T,$$

where A_{LR} is the left-right asymmetry, Γ_Z is the width of the Z resonance, M_W/M_Z is the ratio of the W and Z masses [62], R_ν is the ratio of charged to neutral current branching fraction for neutrino scattering [63], and $Q_W(^{133}_{55}C's)$ is the atomic parity violation effect in Cesium [64].

We now take the current measurements of the electroweak observables listed and plot the accepted regions in S and T in Fig. A-2. We have chosen to plot the S-T region for the A_{LR} measurement presented in this thesis separately from the S-T region for the average A_e quoted by the four LEP collaborations. The region favored by the Standard Model, around S,T~ 0 is represented as a black quadrilateral.

We note that there are two regions of convergence for the data in S and T. The first is near S~ 0 and T ~ 0.5, where all the data save the SLD A_{LR}, Q_W seem to converge. The second is at T~ −0.5 and S~ −1.5, where all the data save the LEP $\sin^2\theta_W^{\text{eff}}$ average seem to converge. We note that the latter negative-S region is distinctly prohibited by the Standard Model, and a requirement that an extension to the Standard Model produce a negative value of S is considered quite restricting [65]. However, the disagreement is only at the $\approx 2\sigma$ level as of this writing.
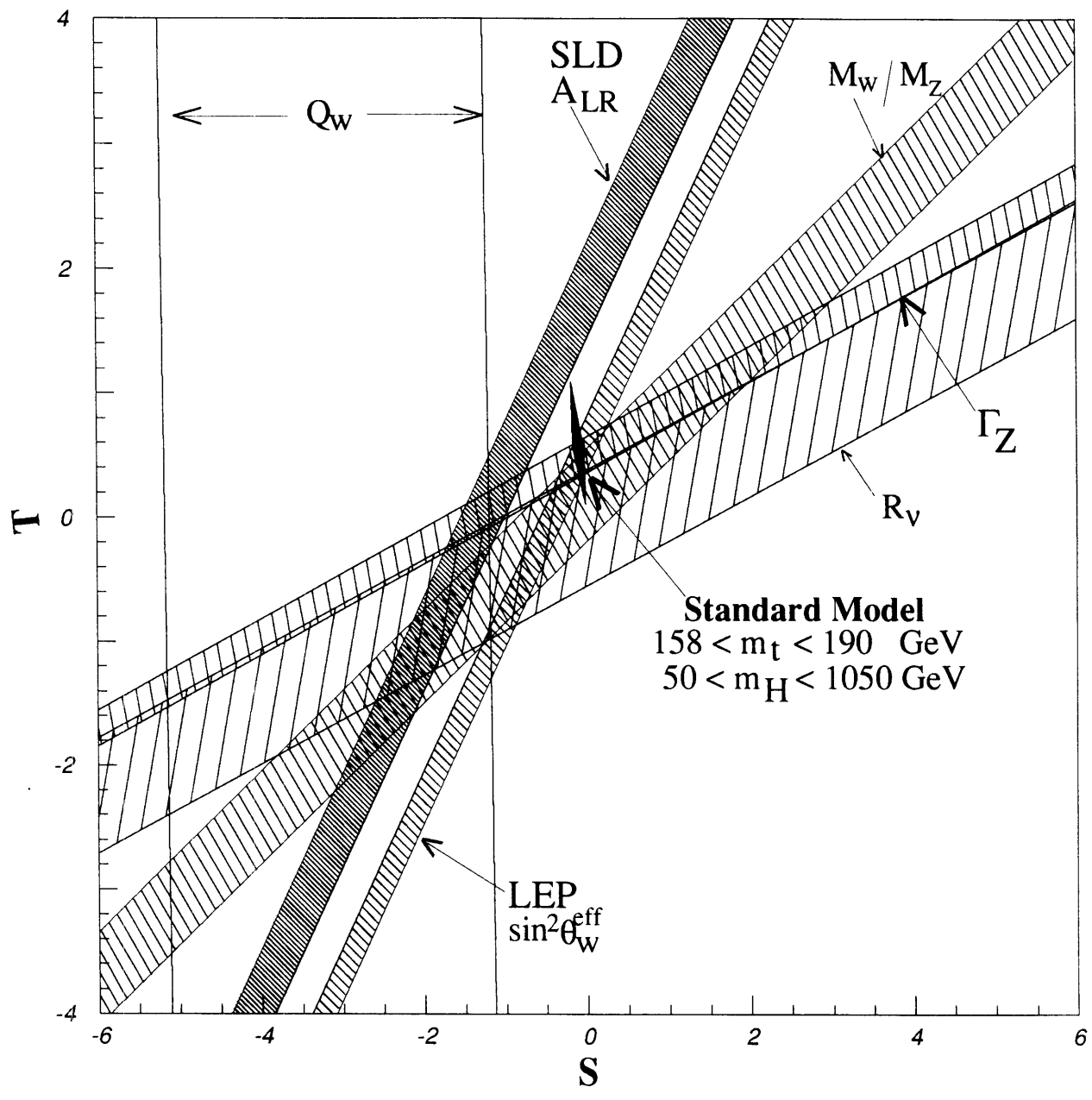
Figure A-2: S and T regions for various electroweak measurements. The black region in at S~ 0, T~ 0 represents the region allowed by the Minimal Standard Model.

Appendix B

Various Cross-checks

In this appendix, we present several cross checks of the beam polarization determination, and the Z event selection. The checks divide into two categories, Compton polarimeter tests, and event-selection checks. We begin with the Compton polarimeter checks.

B.1 Compton Polarimeter Cross-checks

B.1.1 The Linac Møller Polarimeter

There were several cross checks of the Compton Polarimeter. The Linac Møller Polarimeter [66], made an independent determination of the beam polarization before the electron entered the North Arc. Møller polarimetry relies on polarized electrons in an iron-alloy foil to provide the polarized target for the beam electrons, as opposed to the polarized photons provided by the Compton laser. The main difference is that the maximum polarization of the target is ~8%, as opposed to $\geq$99% in Compton scattering, leading to a smaller measured asymmetry. The sign of the target polarization is determined by the sign of the magnetic field produced by Helmholtz coils surrounding the foil. The spread of atomic electron momenta in the target constitutes a large systematic uncertainty for Møller scattering, and must be accounted for. This effect, recently labelled the *Levchuk effect* [67], [68] by workers at SLAC, biases the Møller determination of the polarization by as much as 15%.

Fig. B-1 shows a schematic of the SLC Linac Møller Polarimeter. The Møller polarimeter was situated at the end of the Linac, before the entrance to the Arcs. The Møller polarimeter made an invasive measurement of the beam polarization. The beam was steered to the Møller target which
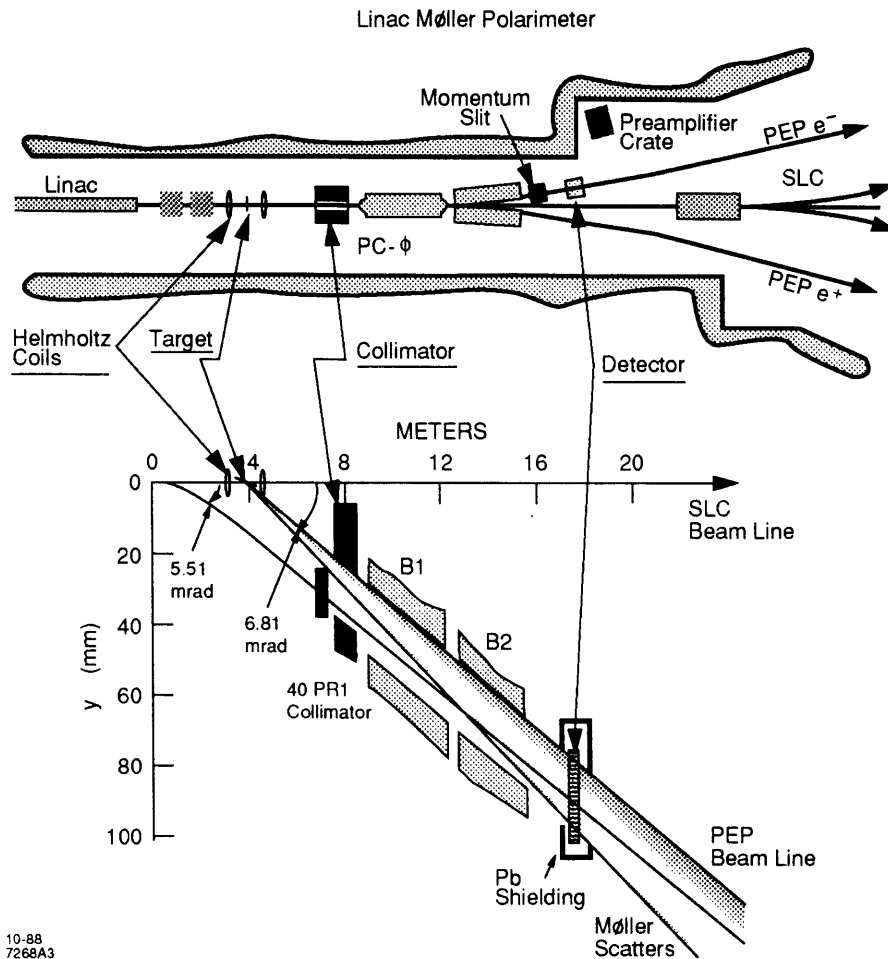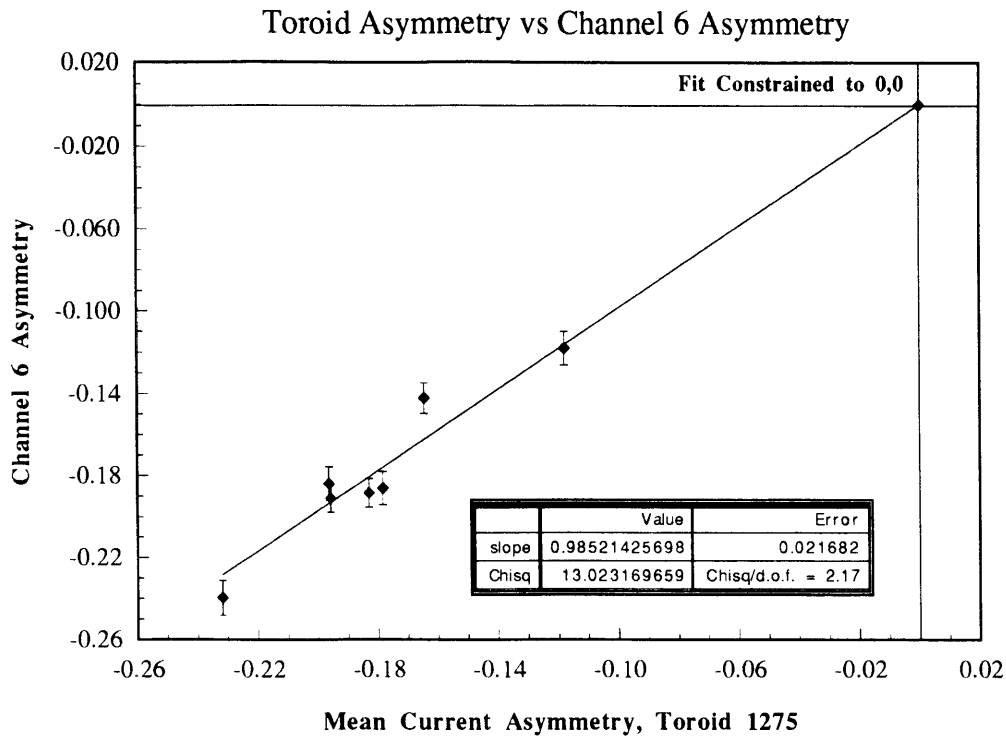
Figure B-1: Schematic of the Linac Møller Polarimeter.

resided in the old PEP extraction line. Collimators then selected the azimuth of the Møller scattered electrons, which were detected in a 64 channel position-sensitive silicon strip detector after showering in a two radiation-length lead-tungsten preradiator.

There were eight separate runs of the Linac Møller polarimeter during the SLC 1993 run. The average of the measurements is $P_{\text{Møller}} = (65.8 \pm 2.7)\%$, which is in agreement with the Compton Polarimeter's determination of the polarization of the beam before it traverses the North Arc, as measured during the narrow-energy beam tests, $P = (65.7 \pm 0.6)\%$.

B.1.2 The Proportional Tube Detector

The Compton scattered electrons, after they had traversed the Compton Čerenkov detector, passed through a proportional tube detector, the PTD. The PTD was essentially an instrumented lead brick. Sixteen 3 mm brass tubes with 20 micron-diameter wire inside constituted the active region

Toroid Asymmetry vs Channel 6 Asymmetry

	Value	Error
slope	0.98521425698	0.021682
Chisq	13.023169659	Chisq/d.o.f. = 2.17

Figure B-2: Results from the induced beam current asymmetry test. The best fit slope of 0.98 ± 0.02 comfirms the ability of the Compton Čerenkov detector to make an asymmetry measurement.

of the detector. The wires were charged to -750 volts, and the surrounding region within the tubes filled with a 89:10:1 mixture of Ar, CO_2, and CH_4. The only common systematic uncertainty shared with Compton Čerenkov detector was the light polarization. Unfortunately, PTD detector suffered from linearity problems and was unable to provide an independent measurement of the Compton asymmetry to the precision required. However, the PTD was able to confirm the measurements made by the Čerenkov detector, to $\approx 3\%$ [69].

B.1.3 Induced Beam Current Asymmetry Test

The ability of the Čerenkov detector channels to detect an asymmetry was tested by inducing an asymmetry in the beam current, that was measured by both the Compton detector and the beam current toroids [70].

The test proceeded as follows: a linear polarizer was added to the optics setup on the source laser bench right after the Pockels cell, so that light incident upon the cathode had no circular polarization, and the extracted electrons had no longitudinal polarization. The Pockels cell-linear polarizer combination now acted as a variable intensity attenuator. Pockels cell voltages were chosen

such that the two helicity-state indices now corresponded to different intensities of light incident on the cathode, leading to different electron currents extracted.

The Compton polarimeter was operated as usual, and the signal asymmetry between the two helicity states was determined. The source of the signal asymmetry was not polarized Compton scattering, since the beams were not polarized for this test, but the artificially induced beam current asymmetry. The beam current asymmetry was also measured by several toroids, including some close to the Compton Polarimeter. The SLC was unable to sustain a stable current asymmetry between successive pulses [71], and the current asymmetry between the two states varied between 10% – 22%. However, the current asymmetry as measured by the Compton Čerenkov detector and the appropriate SLC beam toroid matched quite well, as Fig. B-2 shows. The beam current asymmetry fluctuations during this test made it difficult to correlate beam toroid current measurements with Compton Čerenkov detector measurements, limiting the power of the test as a cross-check. However, the test showed that the Compton Čerenkov detector was able to measure a signal asymmetry to $\approx$ 2%.

B.1.4   Compton Laser Fixed Polarizer Test

The two Pockels Cell setup for the Compton Polarimeter laser transport line was tested using a fixed circular polarizer at the entrance to the SLC [72]. This test measured the effectiveness of the Compton laser transport phase shift measurement, and the ability of the two Pockels cell system to compensate for the phase shifts and deliver circularly polarized light to the Compton IP.

For this test, a linear polarizer and a quarter-wave plate were installed in a metal housing such that the fast axis of the quarter-wave plate was oriented at 45° to the axis of linear polarization transmitted by the linear polarizer, creating a right-handed circular polarizer. This polarizer was tested and found to deliver circularly polarized light of $\mathcal{P}_\gamma = (99.5 \pm 0.5)\%$, then installed in front of the the SLC vacuum beam-pipe entrance window. The Compton Polarimeter was then operated as usual. The fixed polarizer bypassed the many windows and mirror pairs of the Compton Laser transport line, but lacked the ability to randomly select light helicity pulse-to-pulse. The $\mathcal{P}_e\mathcal{P}_\gamma$ product determined from the asymmetry between the two electron helicities scattering from the right-circularly polarized light is shown in Fig. B-3, along with $\mathcal{P}_e\mathcal{P}_\gamma$ determined from a few Compton measurements made immediately before the test was performed. The average of the beam polarization measurements for the normal runs was $\mathcal{P}_e\mathcal{P}_\gamma = 0.607 \pm 0.004$, while the average of the measurements with the fixed polarizer in place was $\mathcal{P}_e\mathcal{P}_\gamma = 0.601 \pm 0.005$. The fixed polarizer test lends confidence that the two Pockels cell method used to measure and compensate for the laser transmission line phase shifts worked well and delivered circularly polarized light to the Compton
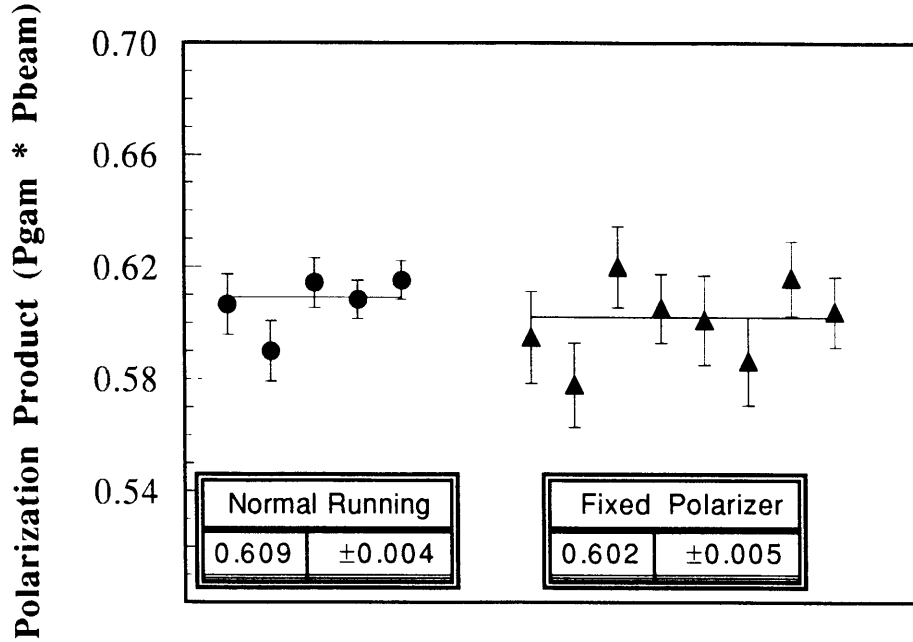
Figure B-3: Result from the Compton Laser fixed polarizer test. This test confirmed the ability of the Pockels cells scans to compensate for phase shifts in the transport system and deliver circularly polarized light to the Compton IP.

IP.

B.2   Event Selection Cross-checks

B.2.1   Selection Criteria Biases

If the Z event sample used for the A_{LR} analysis contained a large class of backgrounds that somehow passed all the selection criteria described in Chapter 8, then very probably the measured asymmetry would be a sensitive function of the event selection criteria. The measured asymmetry, A_m, would vary as the selection criteria were tightened, and more of the background was eliminated. We investigated the possibility of such a background in our Z data calculating the value of A_m for different sets values of the event parameters used in selection. Fig. B-4 shows A_m in different bins of total energy, energy imbalance, cluster multiplicity and time from nearest polarization measurement. The straight line in the histograms indicates a fit to a constant. In all cases the fit is consistent with the constant $A_m = 0.1024$.

The lower measured asymmetry for the first few bins of the cluster multiplicity distributions
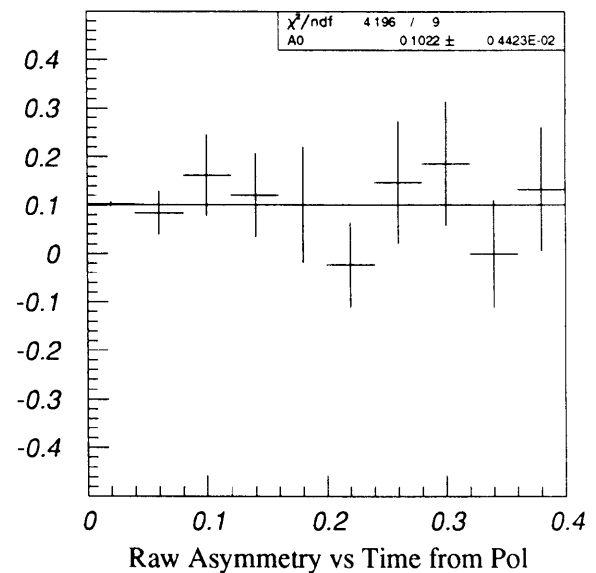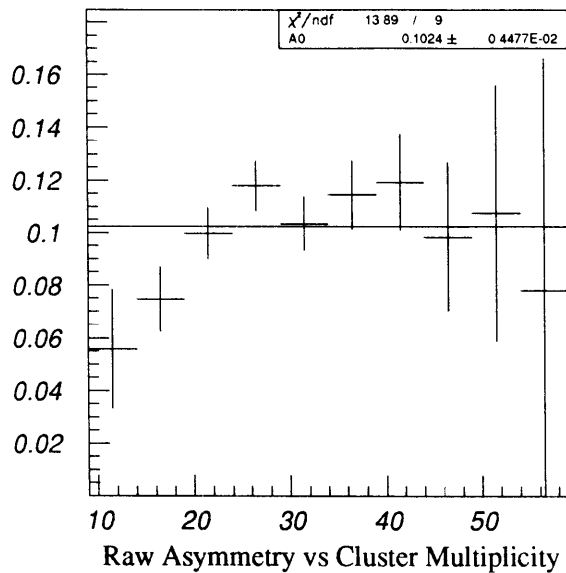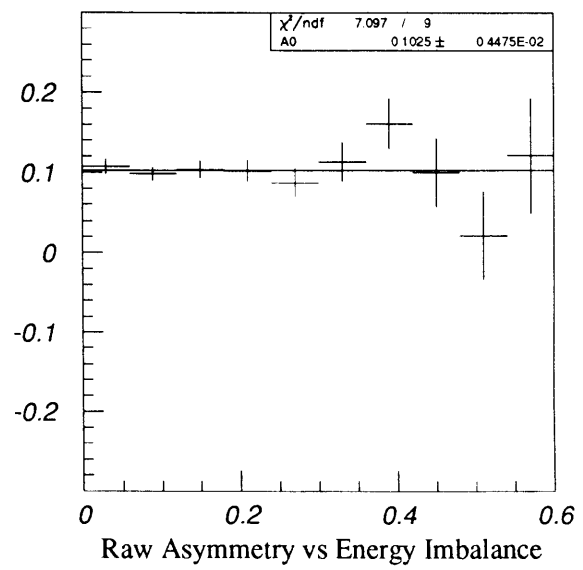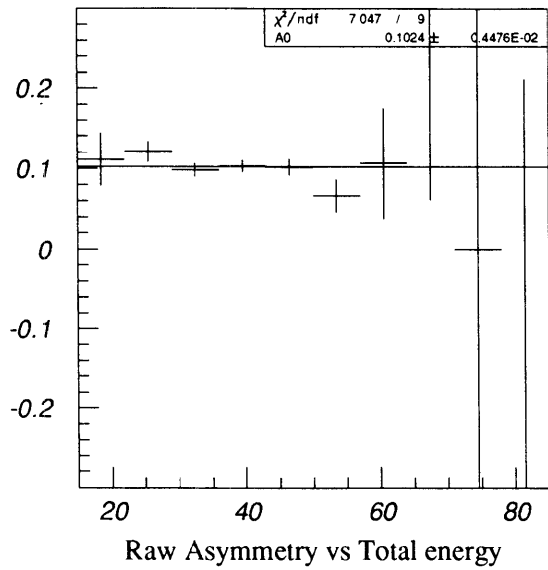
Figure B-4: Raw Asymmetry plotted in bins of total energy, energy imbalance, cluster multiplicity, and time from polarization. The best fit to the data is shown as a horizontal line. The numerical value of the best-fit, A_0, and its χ^2/degreeoffreedom are listed.
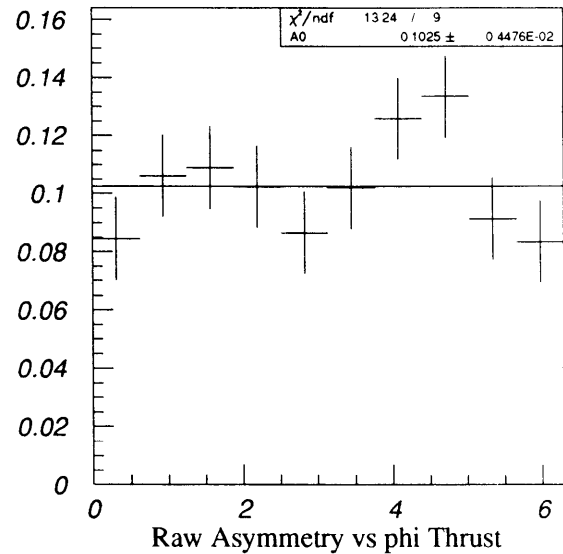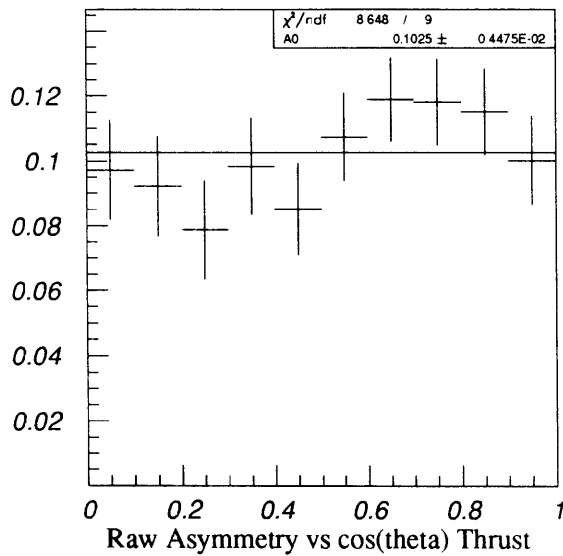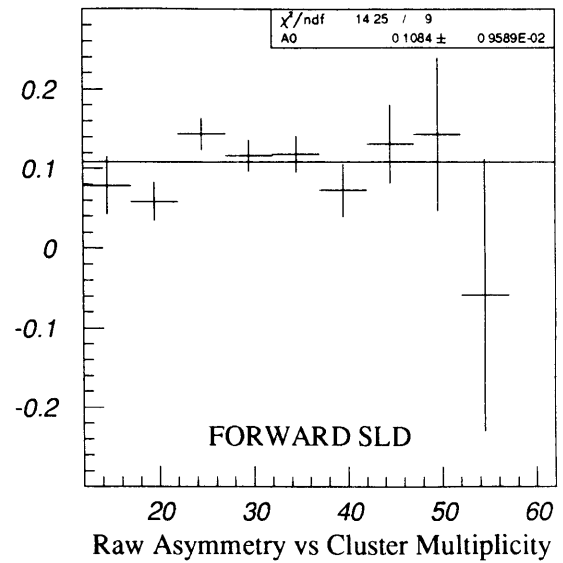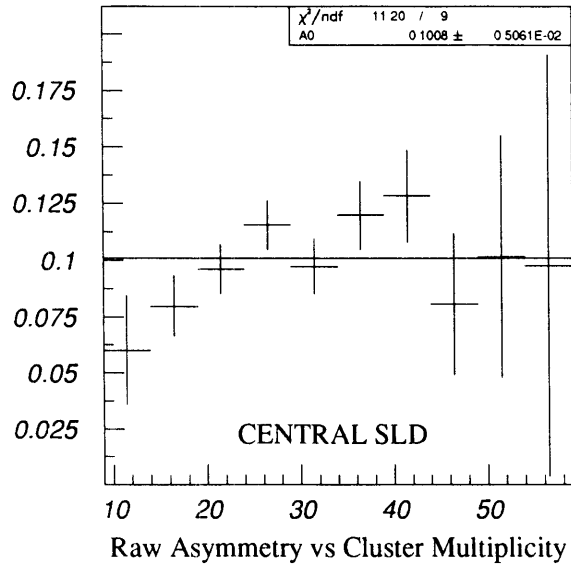
Figure B-5: Raw Asymmetry in bins of cluster multiplicity separately for central and forward parts of SLD, as well as $\cos\theta$ and ϕ. The best fit to the data is shown as a horizontal line. The numerical value of the best-fit, A_0, and its χ^2/degreeoffreedom are listed.

caused us to investigate the events with low cluster multiplicity. As noted in section 8.3, the cluster multiplicity distributions were difficult to simulate, and the concern that some class of backgrounds was populating these low cluster multiplicity bins caused us to examine all the events in those bins closely. The first two histograms in Fig. B-5 shows the asymmetry versus cluster multiplicity distribution separated into the central and forward regions. The low asymmetry for the low cluster multiplicity bins was found to come from events in the central part of the detector (not the forward part where backgrounds would be expected to contribute the most), whose event topologies suggested strongly that they were hadronic decays of Z events. Although the best fit to a constant for the central part distribution is seen to be low, it is still statistically consistent with 0.1024.

The possible correlation of A_m was studied for other event parameters of interest. The last two histograms in Fig. B-5 show A_m calculated in bins of $\cos\theta$ and ϕ,the polar and azimuthal angle of the event's thrust axis. The best fit to a constant value are shown. Several other event parameters, such as the value of the polarization measurement associated with the Z, the statistical error on that measurement, the sphericity, oblateness, and track multiplicity were tested in the same way and found to have no correlation with the measured asymmetry.

B.2.2   Calorimeter-Independent event selection

We used the SLD Central Drift Chamber (CDC) and the Vertex Detector (VTX) to select a sample of hadronic decay events with negligible backgrounds. Since the CDC coverage only extended out to $\approx 53°$ in the polar angle, the size of the data set is much smaller than the A_{LR} data set selected by the Calorimetric data selection. In addition, the data sample is further reduced by inefficiencies in the CDC and VTX tracking and vertex-finding hardware and software. which have been described elsewhere [73]. We used the Pass 1 events which had tracks close to the primary vertex. We demanded at least six tracks with momentum equal to or greater than 250 Mev originate from a cylindrical fiducial region around the interaction point (IP) of 5 cm in the transverse (ρ) axis. and 10 cm in the z axis. We refer to this the CDC-VTX data selection.

Fig. B-6 shows the absolute polarization plotted for negative and positive helicity events that passed the CDC-VTX cuts mentioned above. A total of 20867 negative-helicity events passed the cuts, along with 16974 positive-helicity ones. This yields $A_m^{\text{CDC-VTX}} = 0.1029 \pm 0.0051$, which agrees with $A_m = 0.1024 \pm 0.0045$. The luminosity-weighted beam polarization for the CDC-VTX selected data is 63.3% (after the chromaticity correction) which also agrees well with the $63.0\% \pm 1.1\%$ from the Calorimetric data selection.

CDC-VTX Data Selection
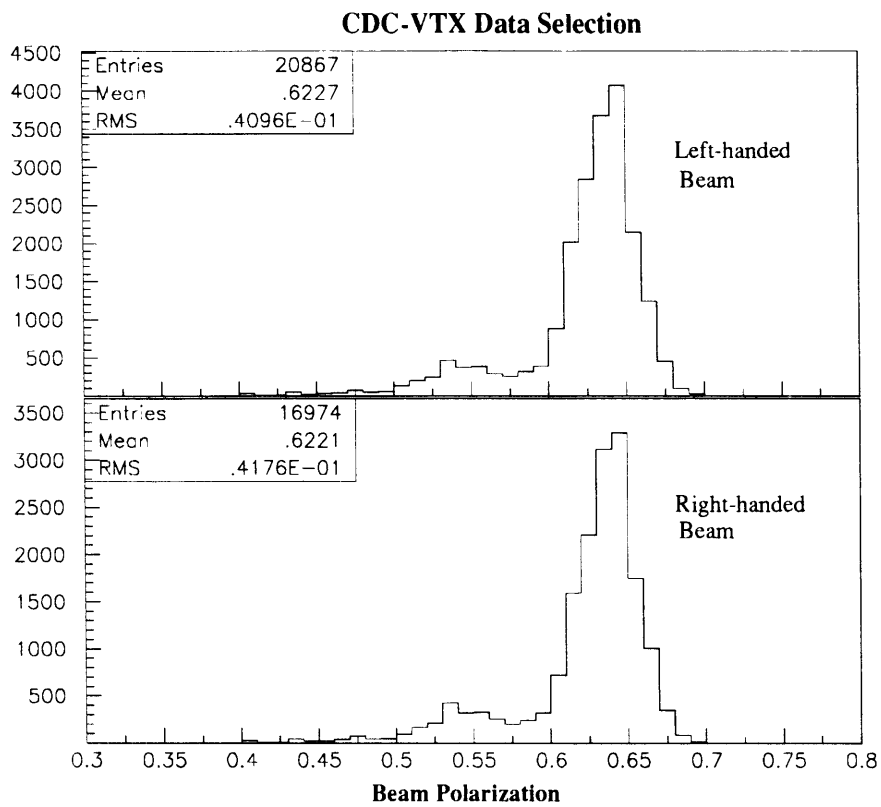
Figure B-6:   Beam polarization for left-handed (top) and right-handed (bottom) events for the CDC-VTX event selection.

References

[1] S.L. Glashow. Partial-Symmetries of Weak Interactions. *Nucl. Phys.*, 22:579, 1961.

[2] S. Weinberg. A Model of Leptons. *Phys. Rev. Lett.*, 19:1264, 1967.

[3] A. Salam and J. C. Ward. Electromagnetic and Weak Interactions. *Phys. Lett.*, 13:168, 1964.

[4] G. Arnison et al. Experimental Observation of Isolated Large Transverse Energy Electrons With Associated Missing Energy at $\sqrt{s} = 540$ GeV. *Physics Letters*, 122B(1):103, 1983.

[5] Particle Data Group. Review of Particle Properties. *Phys. Rev. D*, 50(3), 1994. Part I.

[6] F. Halzen and A.D. Martin. *Quarks and Leptons: An Intorductory Course in Modern Particle Physics.* John Wiley and Sons., 1984.

[7] P.W. Higgs. *Phys. Rev. Lett.*, 12(132), 1966.

[8] See, for instance, G. Alexander *et al, Polarization at LEP* Vol. 1, CERN-88-06 (1988).

[9] M.E. Peskin. Theory of Precision Electroweak Measurements. SLAC-PUB-5210, 1990.

[10] G. Bonneau and F. Martin. *Nucl. Phys.*, B27(381), 1979.

[11] E.A. Kuraev and V.S. Fadin. *Sov. J. Nucl. Phys.*, 41(466), 1985.

[12] Morris Swartz, private communication.

[13] F. Abe et al. Evidence for Top Quark Production in $p\bar{p}$ collisions at $\sqrt{s} = 1.8$ TeV. *Phys. Rev.*, D50, 1994.

[14] D. Bardin et al. A Realistic Approach to the Standard Z Peak. *Z. Phys.*, C44(493), 1989.

[15] D.C. Kennedy and B.W. Lynn. Electroweak Radiative Correction with an Effective Lagrangian. *Nucl. Phys*, B322(1), 1989.

[16] A. Sirlin. Radiative Correction to Neutrino Induced Neutral Current Phenomena in the SU(2) X U(1) Theory. *Phys. Rev.*, D22(971), 1980.

[17] B. Lynn, M. Peskin, and R.G. Stuart. Radiative Corrections in SU(2) X U(1):LEP/SLC. In *Physics at LEP, Proceedings of the Workshop*, volume 1, 1986. CERN 86-02.

[18] M. Consoli and W. Hollik. Electroweak Radiative Corrections for Z physics. In *Z Physics at LEP 1*, page 7, 1989. CERN 89-08.

[19] The process of increasing the quantum-efficiency of the cathode by depsiting cesium came to be known as *cesiation*.

[20] R. Prepost. Polarzed Electron Sources. Unpublished.

[21] The psuedo-random number generator was a 32-bit shift register design of the type described in *The Art of Electronics* by Horowitz and Hill.

[22] T. Junk and T. Johnson. Using the Pseudorandom Number Generator to Check Polarization Bit Integrity. SLD-NOTE-227.

[23] Bruce Schumm, private communication.

[24] J.D. Jackson. *Classical Electrodynamics*. J. Wiley and Sons., second edition, 1975.

[25] T. Limberg. P.Emma, and R. Rossmanith. The North Arc of the SLC as a Spin Rotator. SLAC-PUB-6210, 1993.

[26] F.J. Decker et al. Arc-Spin Transport Studies. SLD-NOTE-238, 1994.

[27] SLD Design Report. SLAC-0273, 1984.

[28] G.D. Agnew et al. Design and Performance of the SLD Vertex Detector, a 120 MPixel Tracking System. SLAC-PUB-5906, 1992.

[29] S.C. Berridge et al. *IEEE Trans. Nucl. Sci.*, NS-39(242), 1992.

[30] L. Rochester et al. Performance of the SLD Central Drift Chamber in the 1992 Physics Run. SLD Note 231, 1993.

[31] Saúl González. First-Pass Determination of the Energy Scale in the SLD Calorimeter. SLD-PHYSICS-NOTE-24, 1993.

[32] G. Blaylock. The WISRD Beam Energy Measurement. SLD Physics Note 22, 1993.

[33] D. Calloway et al. The Compton Polarimeter for SLC. SLAC-PUB-6026, 1992.

[34] P. Horowitz and W. Hill. *The Art of Electronics*. Cambridge University Press, second edition, 1989.

[35] The calculation of polarized Compton scattering has been carried out by various workers. See, for instance. SLAC-PUB-4689 by M. Swartz, *Polarization at SLC*, presented at the Workshop on Polarization at LEP, 1987.

[36] W.R. Nelson, H. Hirayama, and D.W.O. Rogers. The EGS4 Code System. SLAC-Report-265, 1985.

[37] Robert Dean Elia. *Measurement of Left-Right Asymmetry in Z Boson Production by Electron-Positron Collisions*. PhD thesis, Stanford University, 1994.

[38] Max Born and Emil Wolf. *Principles of Optics: Electromagnetic Theory of Propogation, Interference, and Diffraction of Light*. Pergamon Press, 1980.

[39] R.M.A. Azzam and N.M. Bashra. *Ellipsometry and Polarized Light*. North-Holland, 1989.

[40] A. Lath and M. Woods. Compton Laser Analysis: Determination of Polarization and Systematic Errors. SLD-NOTE-236, 1994.

[41] A. Lath and M. Woods. Compton Laser Analysis: Photodiode Noise Pickup, Linearity and ADC Resolution Studies. SLD-NOTE-235, 1994.

[42] B. Schumm et al. Estimate of the Chromaticity Effect on the 1993 Electron Beam Polarization. SLD-NOTE-240, 1994.

[43] K.L. Brown and F.C. Iselin. Decay TURTLE (Trace Unlimited Rays Through Lumped Elements): A Computer Program for Simulating Charged Particle Beam Transport Systems, Including Decay Calculations. CERN-74-2, 1974.

[44] P. Emma and F.J. Decker, private communications.

[45] D. Axen et al. The Lead-Liquid Argon Sampling Calorimeter of the SLD. *NIM*, A328:472, 1993.

[46] J. Yamartino. Hadronic Event Selection using the LAC. SLD Physics Note 14, 1992.

[47] John Michael Yamartino. *A Measurement of the e^+e^- Decay Width of the Z^0*. PhD thesis, Massachusets Institute of Technology, 1994.

[48] V.D. Barger and R.J.N. Phillips. *Collider Physics*. Addison-Wesley, 1987.

[49] K. Pitts, private communication.

[50] Kevin T. Pitts. *Electroweak Coupling Measurements from Polarized Bhabha Scattering at the Z0 Resonance*. PhD thesis, University of Oregon, 1994.

[51] R. Brun et al. GEANT3 User's Guide. CERN-DD/EE/84-1, 1989.

[52] Hyun Hwang, private communication.

[53] H. Aihara et al. *Z. Phys.*, C34(1), 1987.

[54] F. E. Low. *Phys. Rev. Lett.*, 14(238), 1965.

[55] K. Abe et al. First Measurement of the Left-Right Cross Section Asymmetry in Z Boson Production by e^+e^- Colisions. *Phys. Rev. Lett.*, 70(17), 1993.

[56] Beenakker et al. Large Angle Bhabha Scattering. *Nucl. Phys.*, B349, 1991.

[57] A.A. Sokolov and I.M. Turnov. *Dokl. Akad. Nauk. SSSR.*, 153(1052), 1963.

[58] The LEP Collaborations and the LEP Electroweak Working Group. Updated Parameters of the Z^0 Resonance from Combined Preliminary Data of the LEP Experiments. CERN/PPE/93-157, 1993.

[59] The electroweak results from the four LEP collaboratons were presented at the XXIXth Rencontres de Moriond, March 1994, by B. Pietrzyk.

[60] M. Golden and L. Randall. Radiative Correction to Electroweak Parameters in Technicolor Theories. *Nuc. Phys.*, B361, 1991.

[61] M.E. Peskin and T. Takeuchi. Estimation of Electroweak Observables. *Phys. Rev.*, D46(1), 1992.

[62] The Z, W masses are from PDG 1994.

[63] The R_ν value used is an average of the results from the CDHS, CHARM, and CCFR collaborations.

[64] M.C. Noecker et al. Measurement of Parity Nonconservation in Atomic Cesium. *Phys. Rev. Lett.*, 61(310), 1990.

[65] Lisa Randall and Thomas Rizzo, private communications.

[66] The basics of Møller Polarimetery and design and construction of the SLAC Linac Møller Polarimeter are described in detail by M. Swartz in *Physics with Polarized Electron Beams*, SLAC-PUB-4656, (1987).

[67] L.G. Levchuk. The Intra-Atomic Motion of Bound Electrons as a Possible Source of a Systematic Error in Electron Beam Polarization Measurements by Means of a Møller Polarimeter. KFTI-92-32, 1992.

[68] M. Swartz et al. Confirmation of the Levchuk Effect as a Significant Effect in Single-Arm Møller Polarimetry. SLAC-PUB-6467, 1994.

[69] Ross King, private communication.

[70] M. Fero et al. Compton Polarimeter Current Asymmetry Test Results. SLD-NOTE-232, 1993.

[71] Mark Ross, private communication.

[72] M. Fero and D. Calloway. Compton Polarimeter Fixed Polarizer Test. SLD-NOTE-233, 1993.

[73] David C. Williams. *The Left-Right Forward-Backward Asymmetry for b Quarks at the SLD*. PhD thesis, Massachusets Institute of Technology, 1994.